IN SITU VITRIFICATION: NUMERICAL STUDIES OF COUPLED HEAT TRANSFER AND VISCOUS FLOW PROCESSES

Graham F. Carey
Robert J. MacKinnon
Paul E. Murray

Published September, 1990

Idaho National Engineering Laboratory
EG&G Idaho, Inc.
Idaho Falls, Idaho 83415

MASTER

IN SITU VITRIFICATION: NUMERICAL STUDIES OF COUPLED
HEAT TRANSFER AND VISCOUS FLOW PROCESSES
EGG-WM-9050

Approved By: _____ Date: 9/24/90
S. K. Merrill, Manager
In Situ Vitrification

Prepared By: Robert J. MacKinnon for G.F. Carey Date: 9/21/90
G. F. Carey

Reviewed By: _____ Date: 9/21/90
G. L. Hawkes
Technical Reviewer

CONTENTS

FIGURES

TABLES

ABSTRACT

This report describes the formulation, results and conclusions of a series of numerical studies performed to support the Idaho National Engineering Laboratory (INEL) In Situ Vitrification (ISV) treatability study. These studies were designed to explore some of the questions related to the dominant physical phenomena associated with the coupled electric field, heat transfer, and fluid flow processes. The work examines the case of a 3-D axisymmetric problem with a central electrode. Such issues as the form of an electric heating model, choice of boundary conditions, latent heat effects, and conductive and convective transport are considered. Some important conclusions and recommendations are made in relation to the convective effects, determination of property parameters, and the issue of a valid electrical heating model.

1. INTRODUCTION

ISV involves coupled electric field, heat transfer, and fluid flow processes. The work reported here is directed towards the treatment of buoyancy-driven fluid flow in this context. Fluid motion influences heat transfer in the melt zone and may play an important role in determining the melt shape and its extent. Clearly this issue is of special significance in the ISV problem.

The following report is organized mainly as a set of numerical studies designed to guide the ISV modeling work at INEL.[1,2] These numerical studies were performed using the finite element model described in reference 3. The basic format of this report is divided into several distinct pieces covering individual studies and topics. The main issues are listed below by section number:

(2) Coupled viscous flow and heat transfer. The focus here is to obtain a qualitative understanding of flow effects in the process. The finite element type, basic grid, and solution procedure are briefly indicated. Recommendations related to the algorithms are also included. A list of material properties for the calculations is given and, unless otherwise stated in the subsequent sections, the grid, domain, and material types are fixed at these values.

(3) The joule heating model is briefly formulated. This model leads to the important issue of correct heating models in the next section.

(4) The heating models tested include the heating model defined in (2), the heating model applied in the conduction studies[4], and a hybrid model incorporating some effects of both forms. The question of a valid heating model is a central issue, as became clear during the course of the numerical studies. The main difficulties arise from two coupled effects: first the electrical conductivity is a strong function of the material temperature and secondly, the electrical conductivity determines, in turn, the strength and distribution of the heat source for the thermal problem. The difficulties are

1

further complicated by the buoyancy effects in the flow field since these also will be strongest in regions of high thermal gradients and will tend to form cell structures. As indicated above, different models were applied and supporting numerical calculations were made. These calculations served to emphasize the importance of bouyancy driven flow and the strong recommendation that further studies of this coupled effect be made. If the goal of a simplified heating model in a conduction analysis can be realized (and this is not yet known) then the practicality of 3-D simulation and design studies would be greatly enhanced.

(5) Coupled fluid-solid heat transfer is considered next with conduction alone in the solid and both conduction and convection in the melt zone. The nature of the heating model is such that the melt rate is accelerated. This enables us to examine the fluid flow effects in a "contracted time frame", portraying flow cells that will develop in practice only in a longer time frame. This approach permits the calculations to be made more efficiently and yet still lends insight into local effects that may be important early in the process and during startup. Later some long term studies without the accelerated process are examined. The surface boundary condition includes free surface radiation and the far field boundary conditions are of convective heat transfer type.

(6) This section deals with the relative importance of latent heat effects. It is shown that for the material in the ISV problem the Stefan number is of the order of one to ten so latent heat cannot be neglected. Numerical experiments for a 1D problem with a moving melt boundary show that ignoring latent heat will over-predict the boundary location by approximately 20%.

(7-9) The final set of numerical experiments include the effect of an initially heated "frit" zone at the surface. Both conductive solid and fluid-solid situations are tested. Finally, the heating model is such that the time scale now is of the same order as in the ISV process. Multiple flow cells form in the "frit" zone and the melt extends downward. There is strong convective mixing associated with these flow cells and as a result the

2

isotherms are strongly influenced. This effect appears to be important.
Properties and heating model details are summarized in associated tables.

2. COUPLED VISCOUS FLOW AND HEAT TRANSFER

The first phase of calculations was designed to examine coupled fluid flow and heat transfer in a simplified test problem: electrical heating of a fluid domain. The problem corresponds to an axisymmetric domain with a central heating electrode and a remote far field. The finite element discretization for the viscous flow and heat transfer problem is given in Figure 2.1. Since the problem is axisymmetric it can be discretized as a two-dimensional domain with annular elements of quadrilateral section as indicated in the figure. Thus, the problem reduces to a quasi two-dimensional calculation.

The potential field is solved analytically by assuming a simple form for the spatially varying electrical conductivity. The main objective is to investigate the coupled flow and heat transfer aspects of the ISV problem in these numerical studies. In more complete calculations this problem would be solved as a fully coupled problem where the electric field potential and electrical conductivity are updated at each time step. In this study it is assumed that the entire domain is a liquid with constant electrical conductivity. Given the potential solution and the form of the conductivity, the volumetric heat source can be determined from the current.

Note that if one assumes the conductivity is constant, then the potential in the annulus is easily obtained. Let a be the inner radius and b the outer radius with applied potential V. Then the solution is

$$\phi = \frac{V \ln(r/b)}{\ln(a/b)} \tag{2.1}$$

which implies that

$$Q = \sigma_e E \cdot E = \sigma_e \left(V / [\ln(a/b)r] \right)^2 \tag{2.2}$$

As a "worst case" estimate, setting $\sigma = 20$ (ohms-m)$^{-1}$ (at $T = 2273°K$), $V = 1000$ volts, $a = 0.15m$, $b = 1m$ and $r = 0.15m$, we get $Q = 2.48 \times 10^8$ W/m^3. The actual peak value will be less and in the numerical experiment the limit value $Q \leq 10^7$W/m^3 is set.

The problem then reduces to solving for the coupled viscous flow and heat transfer in the axisymmetric domain. This problem is solved by iteratively decoupling the viscous flow equations and heat transfer equations within each time step (for further details see McLay and Carey[3]). Again the principal objective is to obtain a qualitative understanding of the behavior and the dominant effects in the process and to gain insight into appropriate numerical techniques and limitations of the numerical methods with respect to grid size, convective effects, and time step behavior.

The volumetric heat source generates a buoyancy force in the Navier Stokes equations (with the Boussinesq approximations). This force induces motion of the fluid. In the present calculations the fluid flow is solved using an implicit technique, as is the decoupled heat transfer equation in each time step. Neumann boundary conditions apply at the electrode (symmetry) and the far field. The conditions at the surface are modelled using a mixed (convective) boundary condition. Material properties are taken to be those corresponding to Hanford soil. Boundary conditions and material properties are specified in Table 2.1. Beginning with an initially stationary domain with fixed temperature, the solution is integrated in time implicitly. A convective cell forms with the dominant flow in a vertical region adjacent to the electrode and then reducing outward across the top surface as indicated in Figure 2.2.

The velocity vector arrows in the figures are normalized by the maximum velocity at each time step. Little fluid motion occurs away from the electrode. Velocities at time $t = 1000s$ near the electrode are of the order of millimeters per second. The associated heat transfer field is indicated by the plot of isotherms in Figure 2.3. Notice that, although the velocity is not large near the surface, the isotherms extend for some distance radially out across the top surface. There is essentially a thermal layer near the

5

electrode and a partial layer near the surface. Even though the velocity of the flow is not significant, the high thermal capacity for the material scales the convective term in the heat transfer equation. Hence, convection cannot be completely ignored in the heat transfer process. This conclusion appears to be one of the important results that has come out of these studies. The velocity field at a later time t = 2000s is shown in Figure 2.4 and the corresponding isotherms in Figure 2.5.

In interpreting the preceding results, one should keep in mind the important role that the material properties play in the heat transfer process. In particular there is a strong dependence of material properties on temperature. This dependence is shown in the graphs in Figures 2.6 and 2.7, which depict the variation in Prandtl number and Grashof number as function of temperature. The Prandtl number drops precipitously as the temperature increases. If the Rayleigh number is examined as a function temperature (see Figure 2.8), a dramatic increase in the operating range from 1800 to 2200 degrees K occurs. This increase explains the behavior at t = 2000s in the previous figures. As the domain heats up the transport behavior changes. Note that since the Rayleigh number is very large at high temperature the flow does have some convective character, particularly in the time period considered here.

Remarks: The electrical conductivity varies with temperature (and this actually will affect the electric potential). As far as heating is concerned, initially, the greatest heating will be near the electrode. However, as the temperature rises in this region the potential drop across this region falls. The lower the potential drop, the less heating. This effect will tend to reduce the heating near the electrode and promote heating away from the electrode. This feature is important to the success of the process. In some sense the current numerical experiment provides a conservative or perhaps "worst case" situation to guide the further analysis and experiments.

The present numerical experiment suggests that the following points will be important in developing a 3-D simulation:

1. The present calculations employ a fully implicit solution with constant time step of 10 secs. (That is, 200 steps to t = 2000s.) It may be important to use small time steps during the beginning of the heating process and increase the time steps as time increases. Similarly, a combination of implicit and explicit methods may be useful.

2. Some mesh refinement studies with refinement in regions of large gradients may be useful prior to developing a state-of-the-art code with great efficiency. One could refine near the electrode and then adaptively refine as the solution gradients change with the melt.

3. Note that the early time behavior and the late time behavior are quite distinct as indicated in the previous figures and this will be more important for the fluid-solid problem with a large domain.

Table 2.1 Material properties and boundary conditions used in all calculations

---

Properties Used (Hanford Soil)

- Density (kg/m³) $\rho = 2170.0$ kg/m³

- Viscosity (Pa-s)

$$\mu = \begin{cases} 0.5 & T > 2400K \\ 10^{\wedge}\left[0.91\left[\dfrac{10^4}{T} - 4.5\right]\right] & 1000K > T > 2400K, \quad m = 0.91 \\ 10^5 & T < 1000K \end{cases}$$

- Heat Capacity (J/kg K) $c_p = 1046$ J/kgK

- Conductivity (W/m² K) $k = m^*(T - T^*) + k^*$

$$\text{where} \begin{cases} m^* = 2.13 \times 10^{-3}; & T^* = 293K \\ k^* = 0.13 & T < 1173K \\ m^* = 25.5 \times 10^{-3} & T^* = 1173K \\ k^* = 2.0 & T > 1173K \end{cases}$$

- Volumetric Expansion (1/K) $\beta = 10^{-4}$ $T_{ref} = 1428K$

- Melt Temperature (K) $T_{melt} = 1428K$ (1160°C)

- Electrical Conductivity (1/Ωm)

$$\sigma_E = \begin{cases} 10^{\wedge}\left[m\left[\dfrac{10^4}{T} - X_0\right]\right] & T > 1428K \\ 10^{\wedge}\left[a\left[\dfrac{10^4}{T}\right]^2 + b\left[\dfrac{10^4}{T}\right] + c\right] & T < 1428K \end{cases}$$

$m = -1/1.9$ $X_0 = 6.9$
$a = -8.28 \times 10^{-2}$ $b = 0.61$ $c = -0.288$

Table 2.1 (continued)

Boundary Conditions

- Top Surface (W/m^2) $q = h(T - T\infty)$

  where $\begin{cases} h = 42W/m^2K \\ T\infty = 843K \end{cases}$

- Bottom and Side $q = 3200 \ w/m^2$

- Centerline $q = 0$
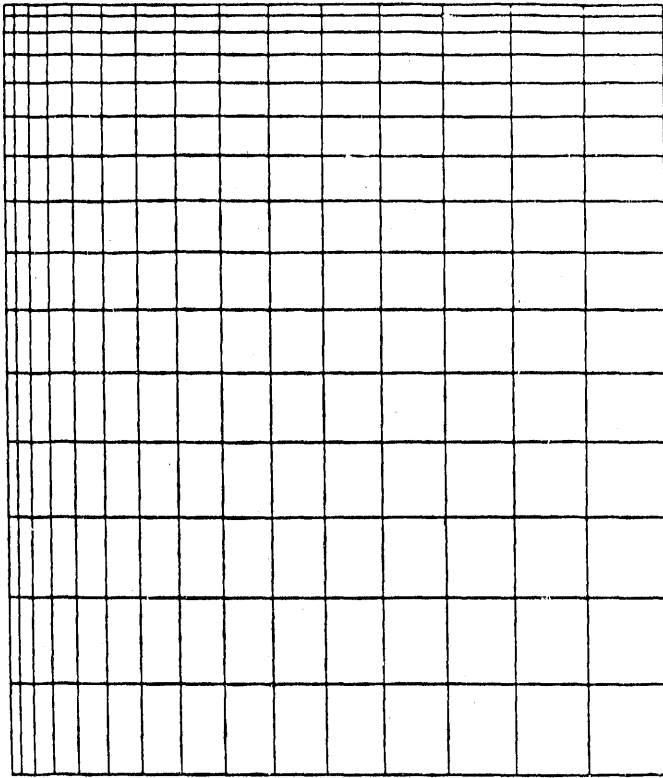
Fig. 2.1 Finite element discretization for ISV calculations. Graded mesh of quadratic elements, surface corner coordinates (.15,0), (1,0).*

Fig. 2.2 Velocity vector field for Problem 1 at t=1000s. (Fluid material only, constant electrical conductivity, volumetric heat source dependent on the current.) Max velocity .0046m/s at (.2,-.57).
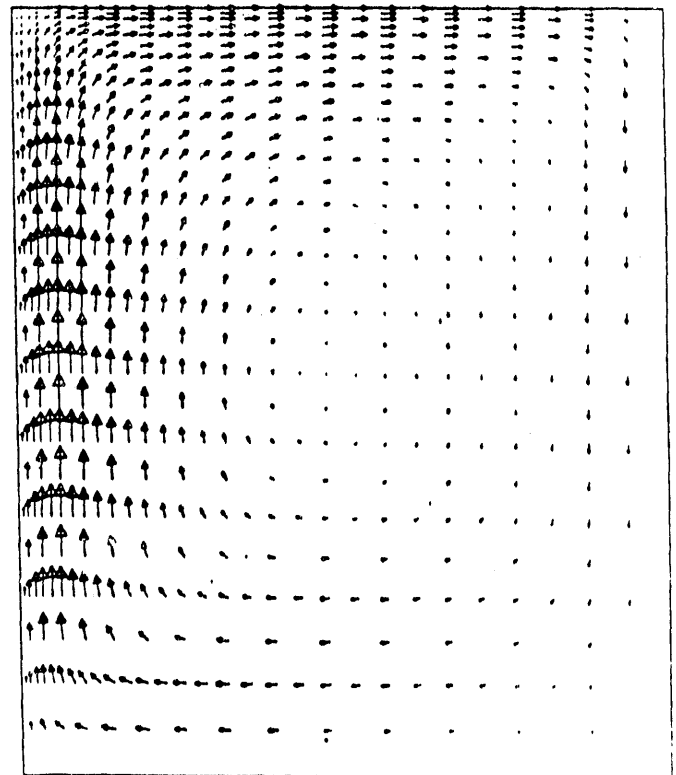
*Here and in all subsequent Figures the domain units are in metrics, time in seconds, velocities in metrics/sec., and temperatures in degrees celcius unless expressly stated otherwise.
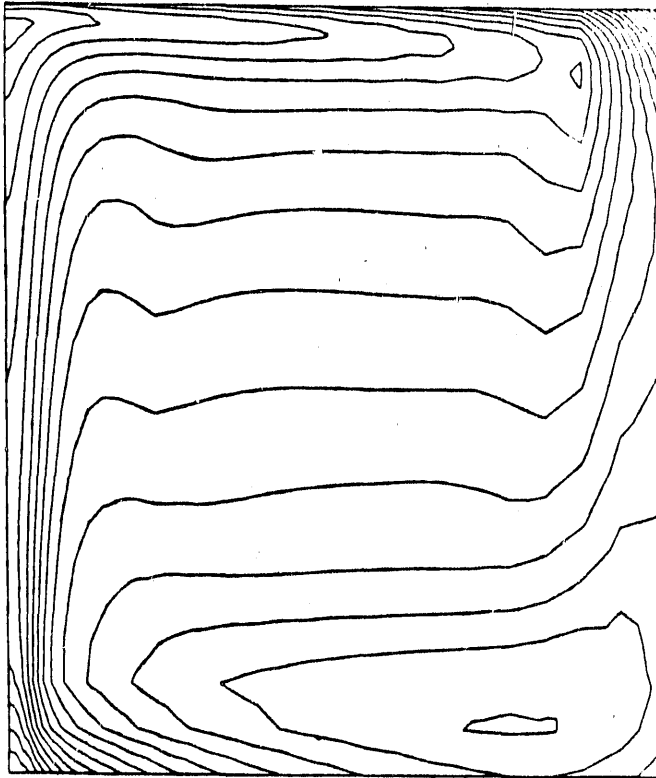
Fig. 2.3 Temperature isotherms for Problem 1 (see velocity field in Fig. 1.2). Max. temperature 1674°, at top left corner (.15,-1). Min. temperature 1402° at top right corner (1,0). Contour spacing approximately 13°. Note the extent of the "horizontal contour loops" near the surface.

Fig. 2.4 Velocity vector field for Problem 1 at t=2000. Max. velocity .0048m/s at surface near right corner at (.8,0). There is a small secondary cell at the bottom left corner and a major cell at the top right corner.
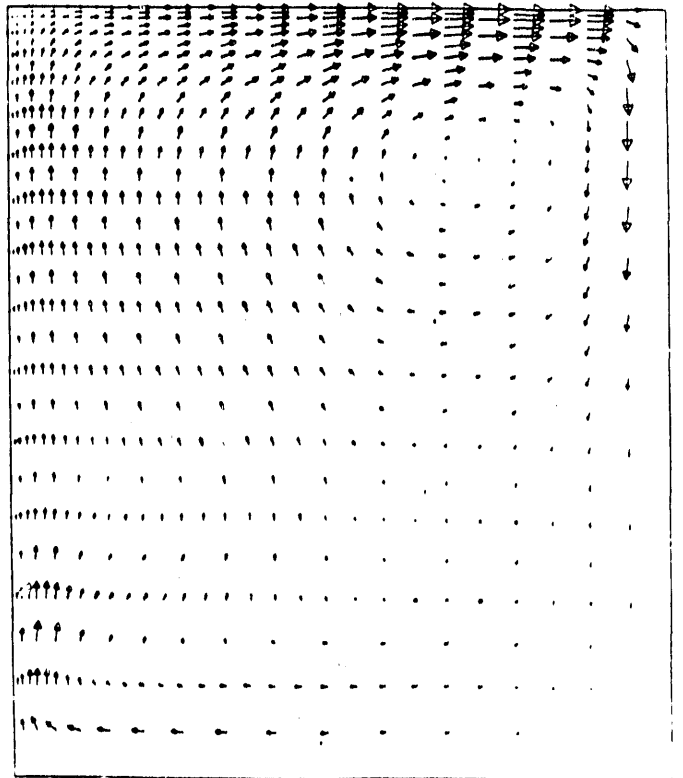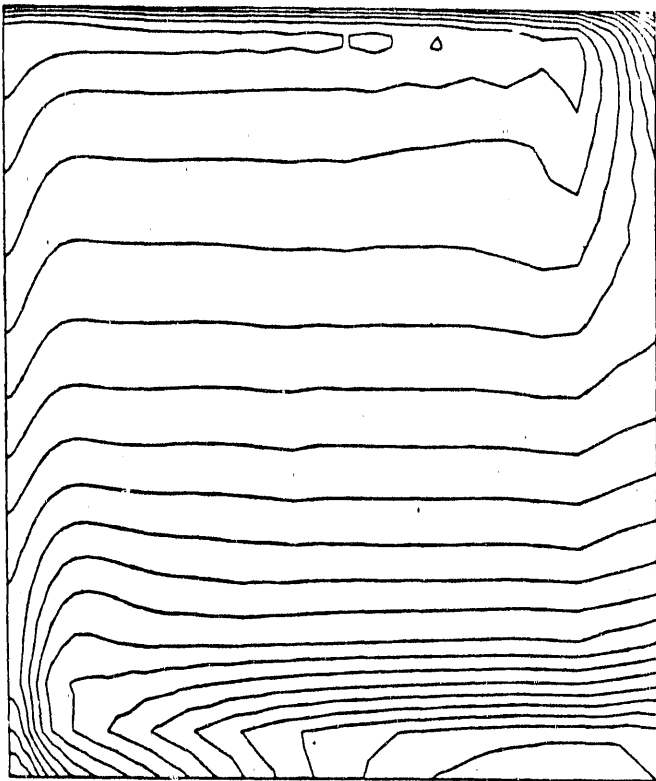
Fig. 2.5   Temperature isotherms at t=200
for Problem 1.   Max. temperature is 1824
at (.15,-.05).   Min. temperature is 1598
at (.8,-1).   Contour spacing is
approximately 10.7°.

Fig. 2.6   Variation of Prandtl
Number with temperature for Hansford
Soil.

PRANDTL NUMBER FOR HANFORD SOIL

GRASHOF NUMBER FOR HANFORD SOIL
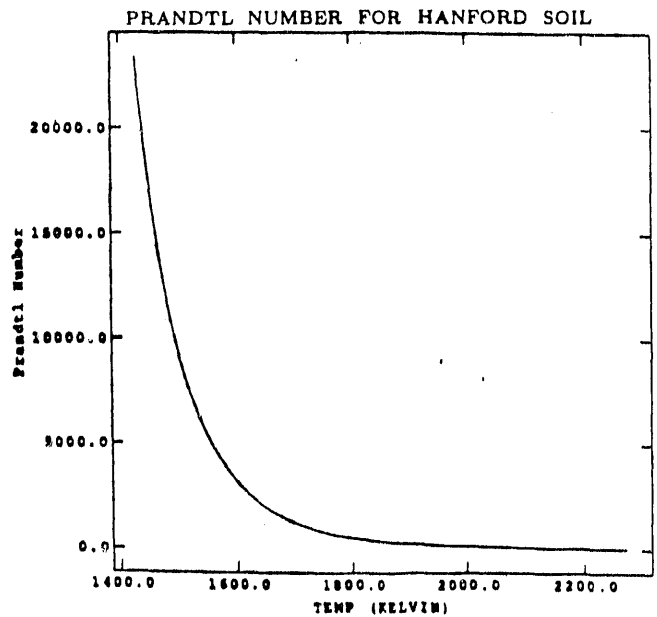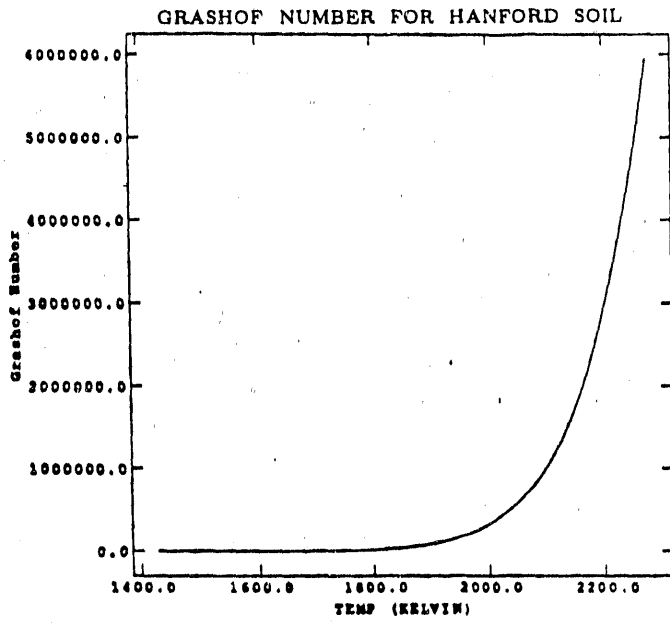
Fig. 2.7   Variation of Grashof Number
with temperature for Hansford Soil.

Fig. 2.8   Variation of Rayleigh
Number with temperature for
Hansford Soil.

RAYLEIGH NUMBER FOR HANFORD SOIL

13
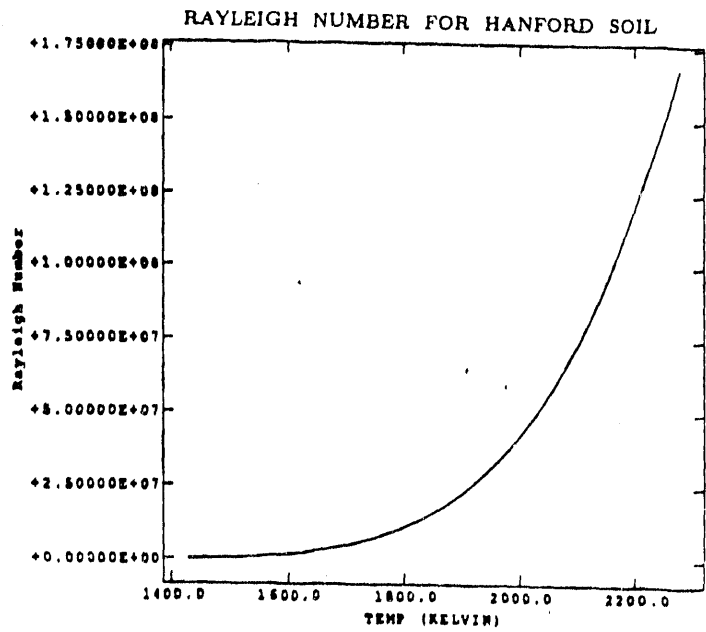
3. JOULE HEATING

The heating from the electrode is joule heating. In a pointwise sense, this is $J \cdot E$ where J is the electric current density vector and the electric field E is the gradient of the electric potential. Now,

$$J = \sigma E + J_v \tag{3.1}$$

where J_v is the electrical current due to motion of the material with free charge.

The conservation of free charge (ρ_f = density of free charge) implies

$$\frac{\partial \rho_f}{\partial t} + \nabla \cdot J = 0 \tag{3.2}$$

Using (3.1), (3.2) can be rewritten

$$\nabla \cdot \sigma E + \nabla \cdot J_v + \frac{\partial \rho_f}{\partial t} = 0 \tag{3.3}$$

Nondimensionalizing, let $\bar{E} = E_0 E$, $\bar{u} = \frac{1}{\tau} u$, $\bar{J_v} = \frac{\varepsilon_0 E_0}{\tau} J_v$, $\bar{\rho_f} = \frac{\varepsilon_0 E_0}{1} \rho_f$, and $\bar{\sigma} = \sigma_0 \sigma$,

where ε_0 is the permittivity, 1 is the reference length and τ is the time scale of interest. Using these variables in the above equation and simplifying

$$\nabla \cdot \bar{\sigma} \bar{E} + \frac{\tau_e}{\tau} \left[\nabla \cdot \bar{J_v} + \frac{\partial \bar{\rho_f}}{\partial t} \right] = 0 \tag{3.4}$$

where $\tau_e = \varepsilon_0/\sigma_o$. If the ground has the permittivity of free space - this is reasonable if there is no significant dielectric material in the ground then

14

$\varepsilon_0 = 8.854 \times 10^{-12}$. When the ground is melted, the electric conductivity σ_0 ranges from 1 to 100/Ωm and letting τ be 1/60 second implies $\tau_e/\tau \sim O(10^{-11})$.

Even for any large dielectric material, the second term in equation (3.4) can be neglected so that

$$\nabla \cdot \overline{\sigma} \, \overline{E} = 0 \tag{3.5}$$

Using the fact that the heating is $J \cdot E$ and the electric current due to motion can be neglected, the joule heating is

$$Q = \sigma E \cdot E \quad \text{or} \quad \sigma \|E\|^2 \tag{3.6}$$

This result implies that the direction of the electric field is not important.

4. HEATING MODELS

In the previous sections flow and temperature solutions for the test problem were presented. One of the primary features of the ISV problem has been demonstrated to be the nature of volumetric heating due to the E field. As noted earlier, the electrical conductivity σ is a strong function of temperature and the temperature varies significantly over the domain and with respect to time. In the present report alternative forms of heat models are considered to provide further insight into the modelling problem and coupled ISV processes.

It is clear that the heat source behavior plays a dominant role and that reliable predictive simulation requires that the joule heating be treated correctly. This fact, in turn, implies that $\sigma(T)$ should be computed as part of the nonlinear coupled E-field, heat transfer and fluid flow problem. Nevertheless, heat source models can be very useful in preliminary analyses and can enhance our understanding of the interactions. Moreover, a full analysis together with laboratory experiments may yield improved simulations. More work is needed in this direction and the present investigation is directed towards this objective.

Recall that the E field satisfies

$$\nabla \cdot \sigma E = 0 \quad \text{in domain } \Omega \tag{4.1}$$

with

$$E = -\nabla \Phi \tag{4.2}$$

for potential ϕ, so that

$$\nabla \cdot (\sigma \nabla \Phi) = 0 \quad \text{in } \Omega \tag{4.3}$$

where $\sigma = \sigma(T)$, temperature T.

In addition, the Joule heating is

$$Q = J \cdot E = \sigma E \cdot E \qquad (4.4)$$

or, equivalently,

$$Q = J \cdot J / \sigma \qquad (4.5)$$

As temperature T rises so does the electrical conductivity σ. Hence, as the temperature changes locally during the ISV process so will the current density. As inferred from the form of (4.5), a low σ (high-electrical resistance) will tend to promote heating. This reciprocal property with respect to temperature is an important feature of the ISV process. Here simple (but incomplete) models are considered to further explore the coupled processes. It should be emphasized also that our principal charter in these studies concerns the issues of convective heat transfer due to fluid motion and some of these questions can be addressed, at least qualitatively, by the present approach.

It is instructive to consider the following two simple models to illustrate several points.

Model I. Assume σ is constant σ_E (which clearly is not the case). For the axisymmetric problem of interest, the solution of (4.1) with σ constant can be obtained analytically for voltage V and radii a, b as

$$\Phi = \frac{V \ln(r/b)}{\ln(a/b)} \qquad (4.6)$$

so that

$$E = \frac{V}{r \ln(a/b)}, \quad J = \frac{\sigma_E V}{r \ln(a/b)} \qquad (4.7)$$

and

17

$$Q = J \cdot E = \sigma_E \left[\frac{V}{r \ln (a/b)} \right]^2 \qquad (4.8)$$

Remarks: Note that as r increases (moving out from the electrode the heat source Q decreases as $1/r^2$ and the current density decreases as $1/r$ so that the correct qualitative spatial dependence (volumetric effect for increasing r) is obtained. However, in reality, as the domain heats up σ increases with E and this model implies the volumetric heat source increases accordingly - which is not correct, since we know that as σ increases, the amount of heat generated should decrease. This contradiction leads us to examine the second "simplified case", Model II.

Model II. Assume current density J is constant. Then

$$Q = |J|^2/\sigma \qquad (4.9)$$

Since $|J|$ is assumed constant, then as σ rises with increasing temperature T, Q decreases correspondingly. This model circumvents the difficulty noted for Model I but other problems arise. In particular, the assumption that current density is constant violates the expected spatial dependence on r for a cylindrically symmetric problem. At r_{large} the current density here is assumed the same as for r_{small} but at r_{large} the volume toroid element $\Delta V = 2 \Pi r_{large} dr dz$ is larger and hence the volumetric heating will be larger. Some other related points concerning the early behavior with this model also warrant comment. First, the actual current J will be less than a reasonable assumption since the conduction path is poor in the early time behavior. Secondly, the conductivity is low at low temperatures and this exacerbates the problem. One can propose alternative heating models to try to circumvent these issues. For example

$$J = J_0/r \quad \text{or} \quad Q = j_0^2/(r^2 \sigma) \qquad (4.10)$$

but again the important features related to the coupling of the temperature, E-field and fluid flow are suspect.

18

In the accompanying numerical studies the standard axisymmetric test problem with the above heating model (4.10)is considered. The results can then be compared with those obtained previously. Here J_o = 1500A/m^2 and Q limited to 10^{-7}. That is,

$$Q \approx \min(J_0^2/\sigma r^2, 10^7)$$

Figure 4.1 shows a thermal boundary layer near the top surface at t = 100s with T_{max} = 1395K and T_{min} = 1162K. The interior temperature is approximately constant. By t= 210s interior heating has increased T_{max} to 1835K, T_{min} is 1231K and the isotherms are spread in the interior with again a surface layer due to the surface boundary condition. The velocity vector field is given in Figure 4.3 with V_{max} = .019m/s. At t = 310s the effect of the high capacitance on convective heat transfer is apparent and T_{max} = 2159K, T_{min} = 1239K. This behavior is repeated at t = 410s, 510s, 610s, in Figures 4.5 to 4.10, with corresponding velocity plots and V_{max} ~.015m/s. By t = 2010s a surface layer structure and large central "core" at near uniform temperature has formed as shown in Figure 4.11, which in some respects conforms to the known behavior.

Future work and recommendations include:

1. Probably the most significant issue is the resolution of questions associated with the heating and electric field. Follow-on work should include solving for the E field including the coupling $\sigma(T)$ to the temperature field. One approach would be to iteratively decouple the field solutions within each time step. Also, with the aid of supporting analysis, periodic E-field updates should be considered; that is, not every step.

2. Results for heat transfer alone (in the absence of fluid flow) can then be analyzed and compared with the earlier "simplified" heat models. Various possible new models may arise from this analysis.

3. Next the fully coupled problem can be analyzed including fluid flow.

4. The influence of the coupled electric-field and heat transfer behavior on the numerical algorithms can be examined. That is, nonlinear stability, accuracy, grid size and time step issues.

5. Analyze the problem with buried metal inclusions, etc.

Remark: Although the axisymmetric test case does differ from the field problem, it does embody the important features of the problem and hence these studies will be quite useful. Moreover, these benchmark calculations can be used as comparison studies for the 3-D code validation at INEL.
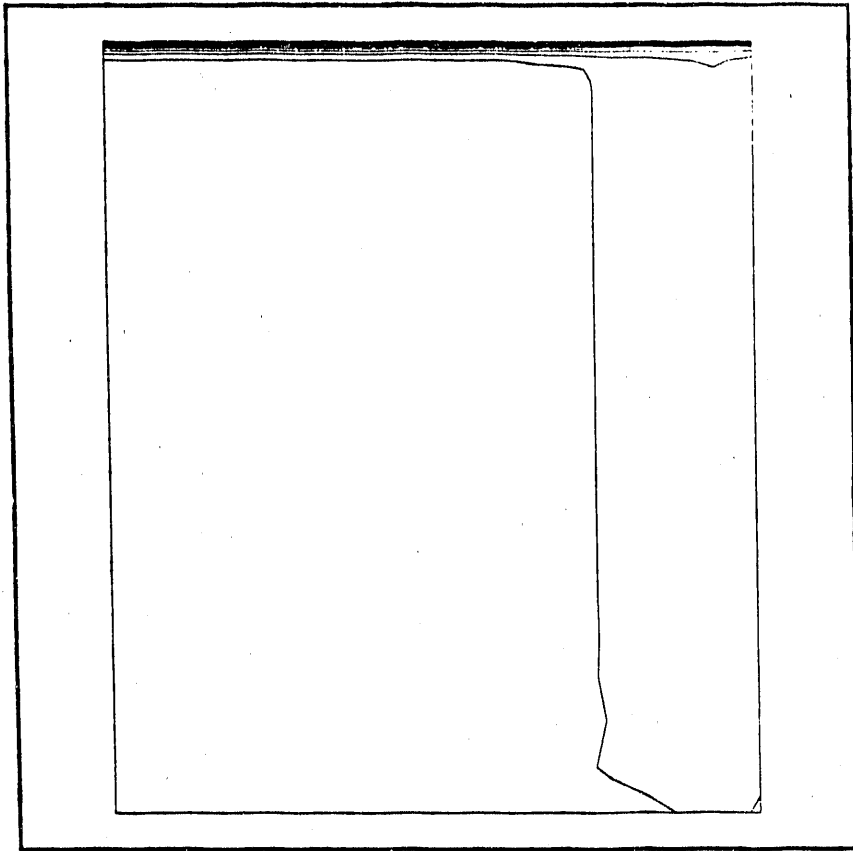
Fig. 4.1 Isotherms

TIME= 110.00
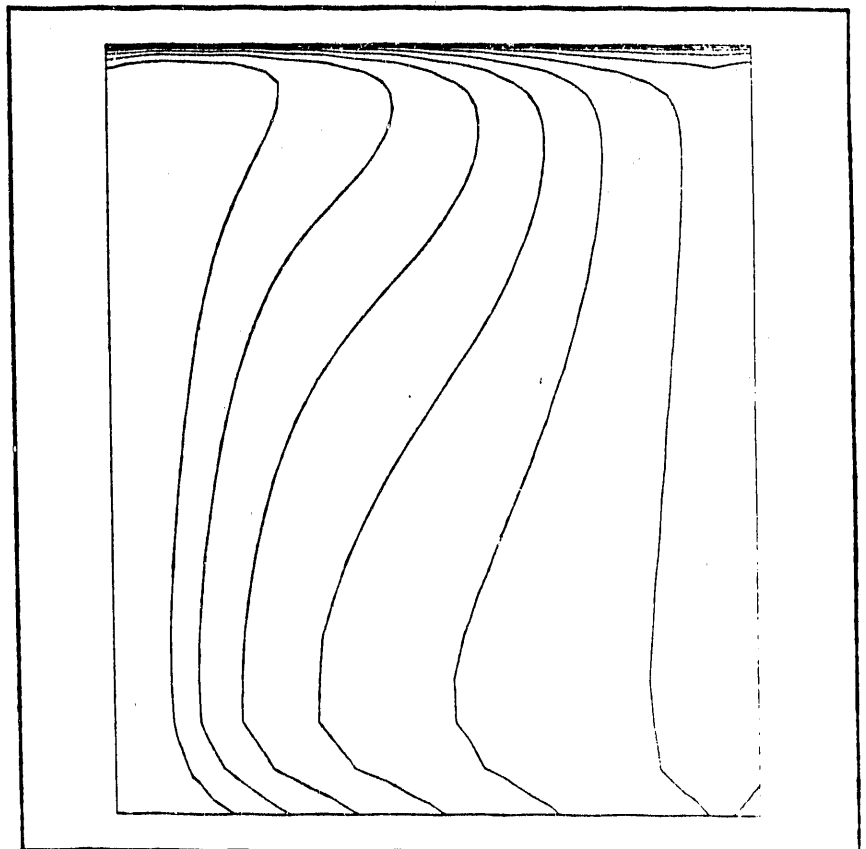
Fig. 4.2 Isotherms 210s

TIME= 210.00

21
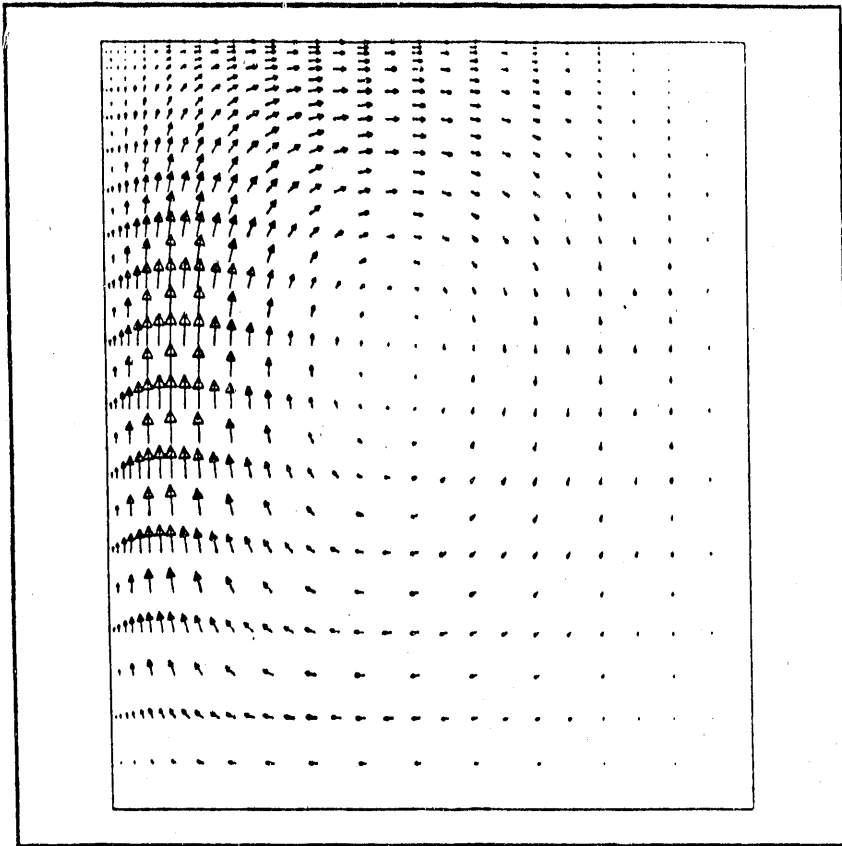
Fig. 4.3
Velocity Vector Plot 310s

TIME= 210.00

Fig. 4.4   Isotherms 310s

TIME= 310.00

22
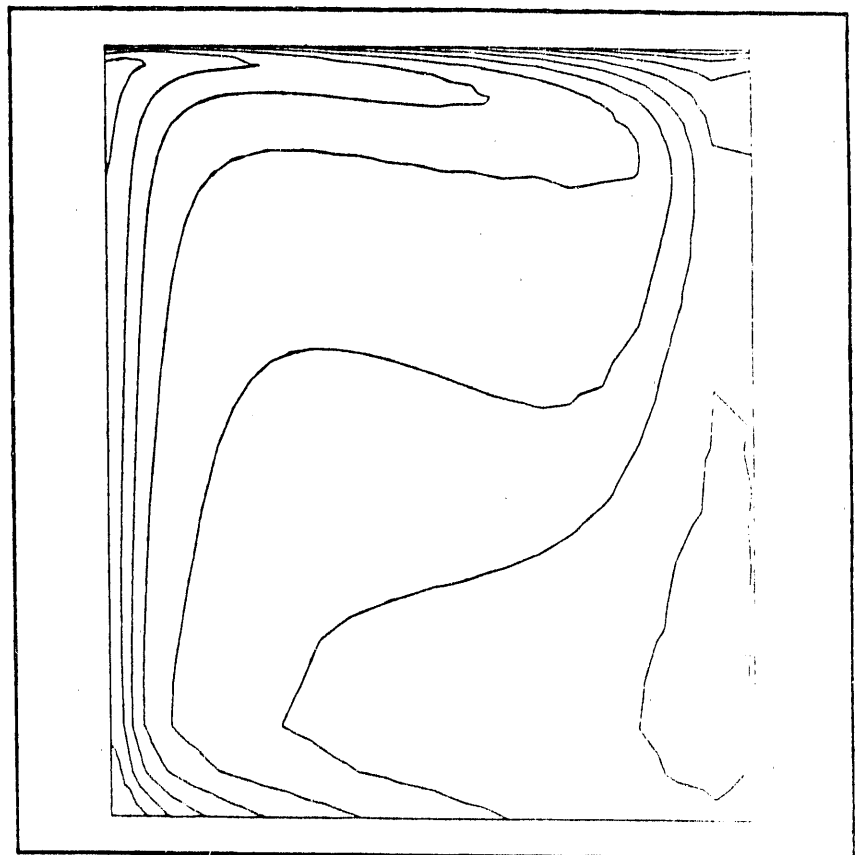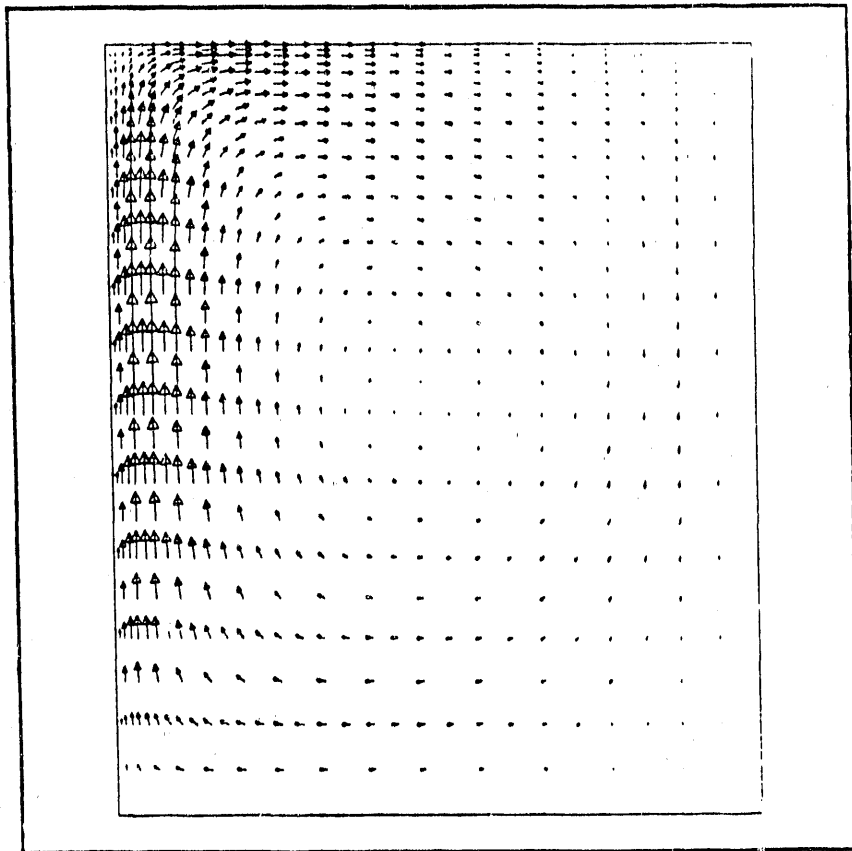
Fig. 4.5

TIME= 310.00

Fig. 4.6
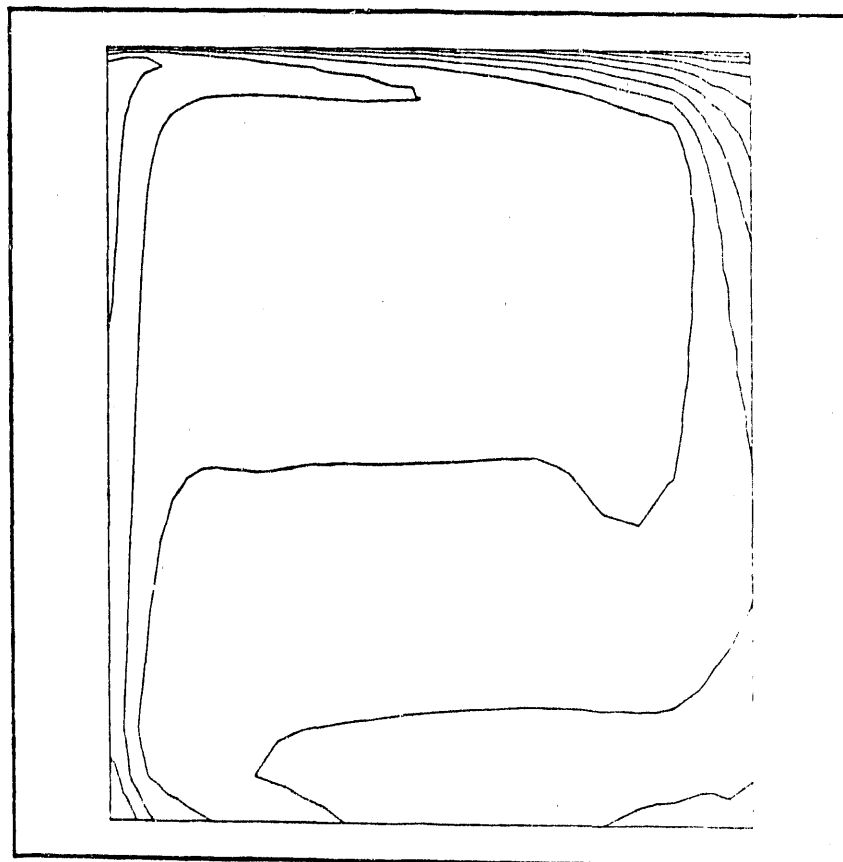
TIME= 810.00
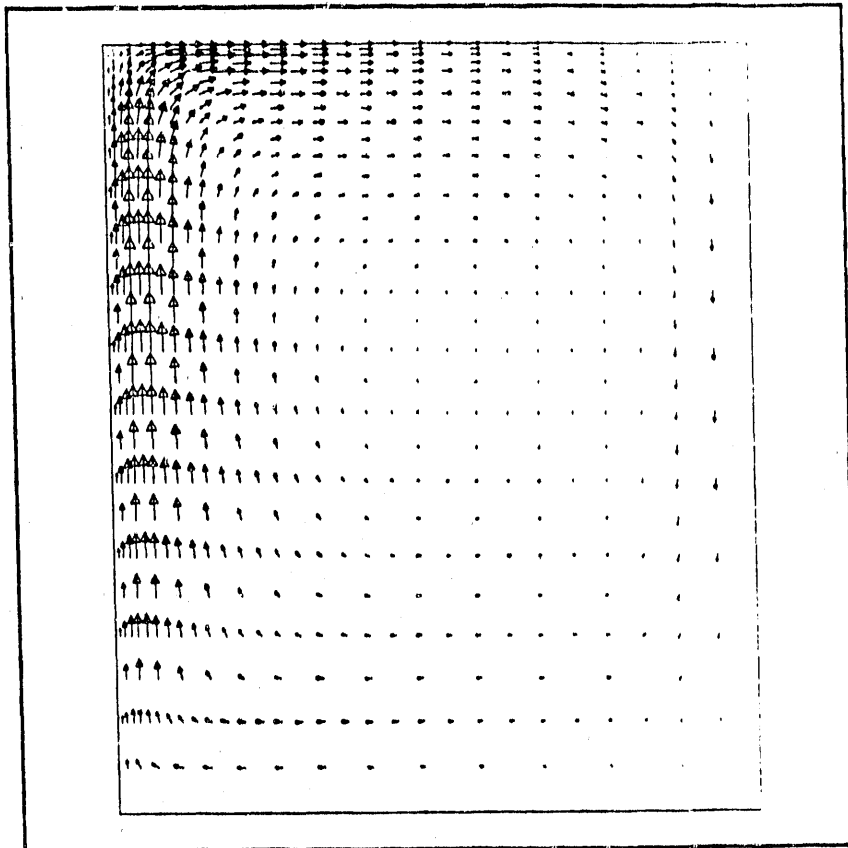
Fig. 4.7

TIME= 810.00

Fig. 4.8

TIME= 1210.0

24
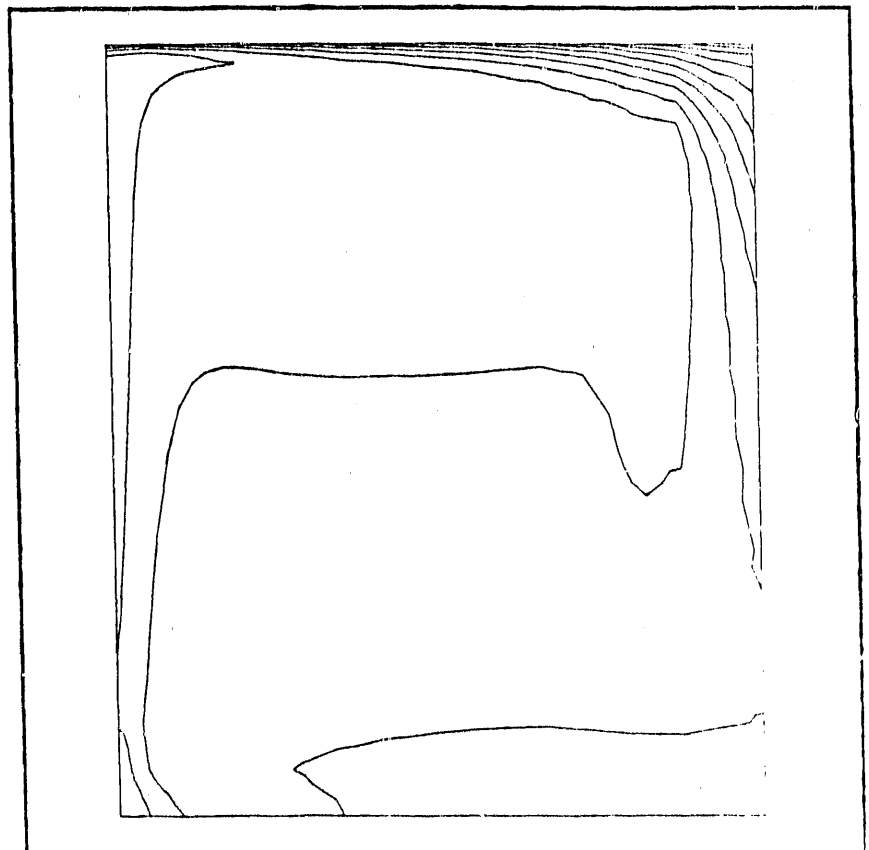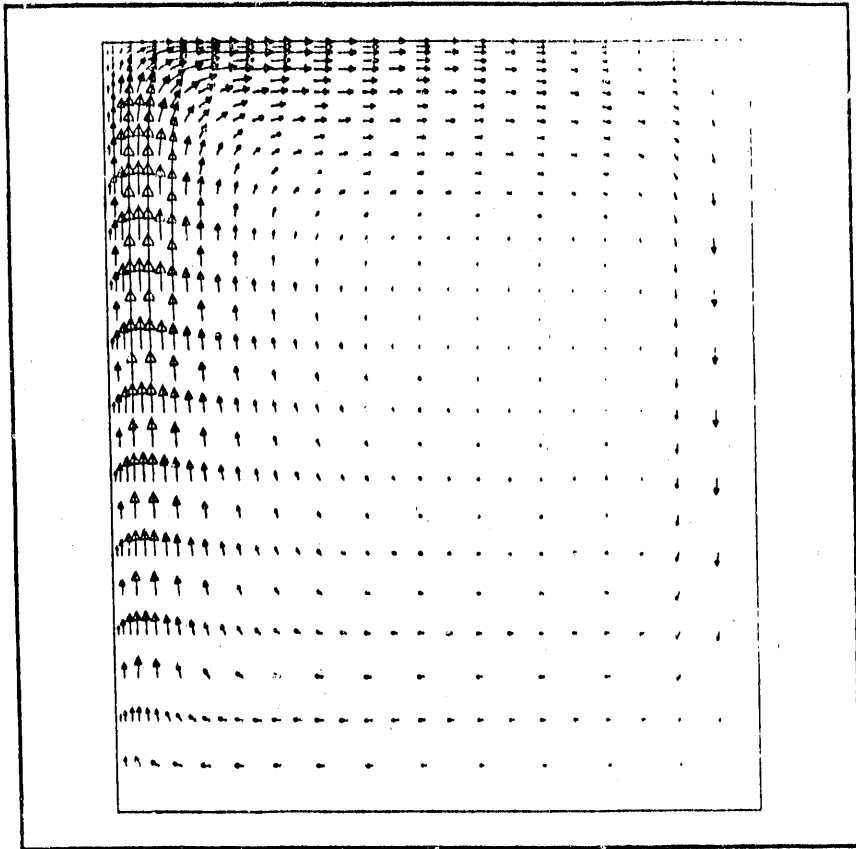
Fig. 4.9

TIME= 1210.0

Fig. 4.10

TIME= 2010.0

25
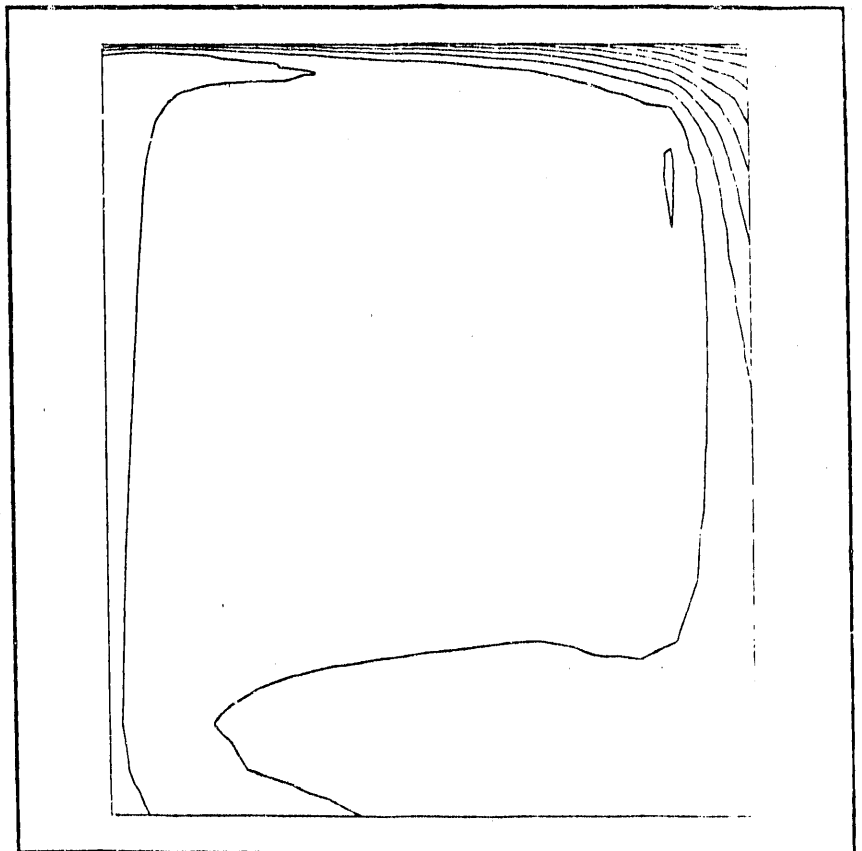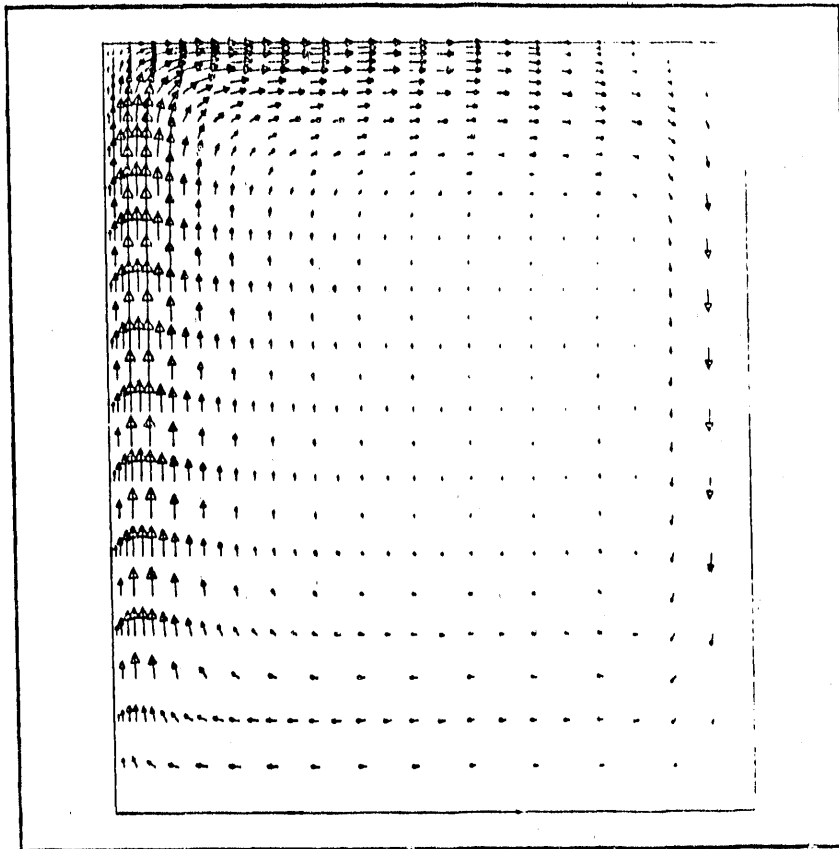
TIME= 2010.0

Fig. 4.11

5. FLUID-SOLID HEATING

In this numerical study the previous annular domain and discretization in previous problems is considered. Initially there is heat conduction in the solid domain and, as melting proceeds, fluid motion in the melt zone occurs with heat transfer by conduction and convection. The buoyancy coefficient is assumed to vary as a function of temperature as follows: It is 0 below the melt temperature T = 1428K and increases linearly until T = 1528K; beyond T = 1528K it is constant at 10^{-4} K^{-1}. At the surface a convective boundary condition applies (heat transfer coefficient is defined as in the previous study).

As heating occurs, the thermal layer near the electrode advances into the interior of the domain with heat transfer initially by conduction alone (and the electrical heat source as before). At a later time the domain begins to melt and heat transfer occurs by convection and conduction in the molten zone, with conduction in the solid. In the attached figures we show the evolution of the temperature isotherms during this process at 100 second intervals. The maximum and minimum temperatures and their location are indicated on the figures. The contours indicate the thermal boundary layer adjacent to the left (electrode) boundary and the upper surface boundary where the convective heat transfer boundary condition applies. There are also some effects at the far field boundary due to the domain approximation.

Conduction occurs through the solid domain to time 810 seconds at which stage melting has been initiated. At t = 910 seconds we see a slight convective roll in the bottom left corner with maximum velocity .04 meters per second. The corresponding isotherms show the effect of the convective velocity on heat transfer in the bottom left corner. By t = 1010s the convective velocity is present along the electrode but the maximum velocity is now at the top left corner. The isotherm plot reflects the influence of the convective heat transfer in both these regions. A similar behavior is evident at t = 1110s with the maximum velocity now .004m/s. (It is important to note that the velocity vectors in each figure are scaled and normalized by the maximum velocity so direct comparison of the figures for velocities can be

misleading as to their magnitude.) At t = 1210s the maximum velocity again occurs in the lower left cell and the magnitude of the maximum velocity is .007m/s.

Subsequent plots show that the velocity peak appears to oscillate between the lower left and top right corners in an interesting quasi periodic behavior. The melt zones in the associated corners grow, as indicated in the isotherm plots until at t = 1810s a second cell has formed in the top left corner due to the effect of the heat source and the associated buoyancy. At this stage the isotherms indicate numerous oscillations and irregularities due to the inability of the grid to accommodate the convective effect.
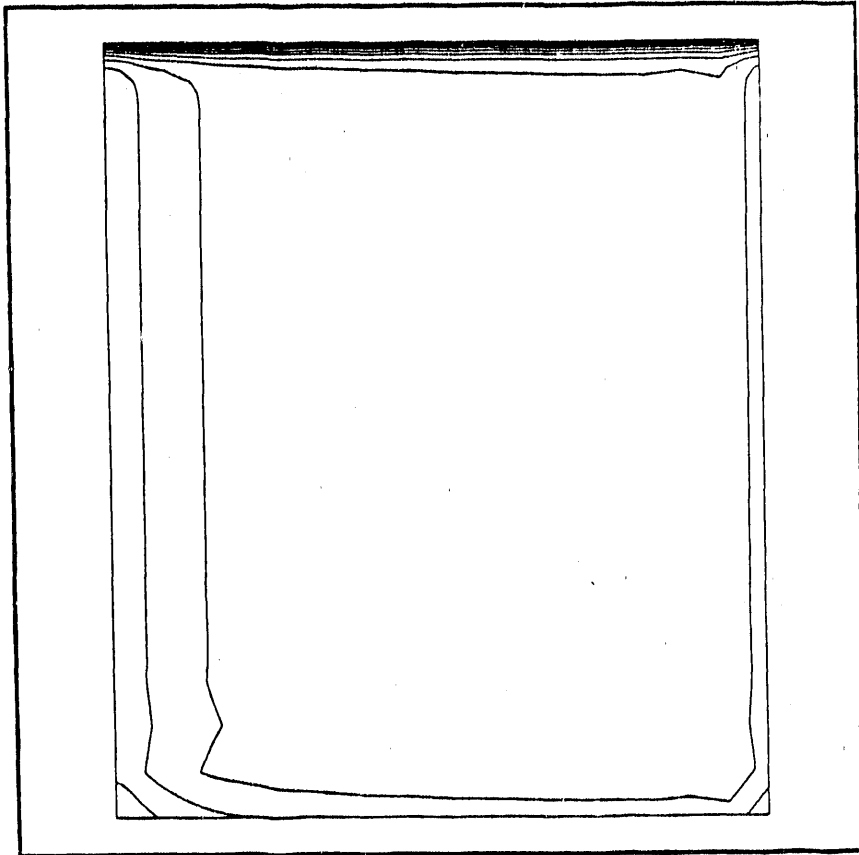
Fig. 5.1
T_{max} 1249 at (.15,−1)

T_{min} 1110 at (.85,0)

TIME= 210.00

Fig. 5.2

T_{max} = 1273 at (.15,−1)

T_{min} = 1094 at (.85,0)

TIME= 310.00

29
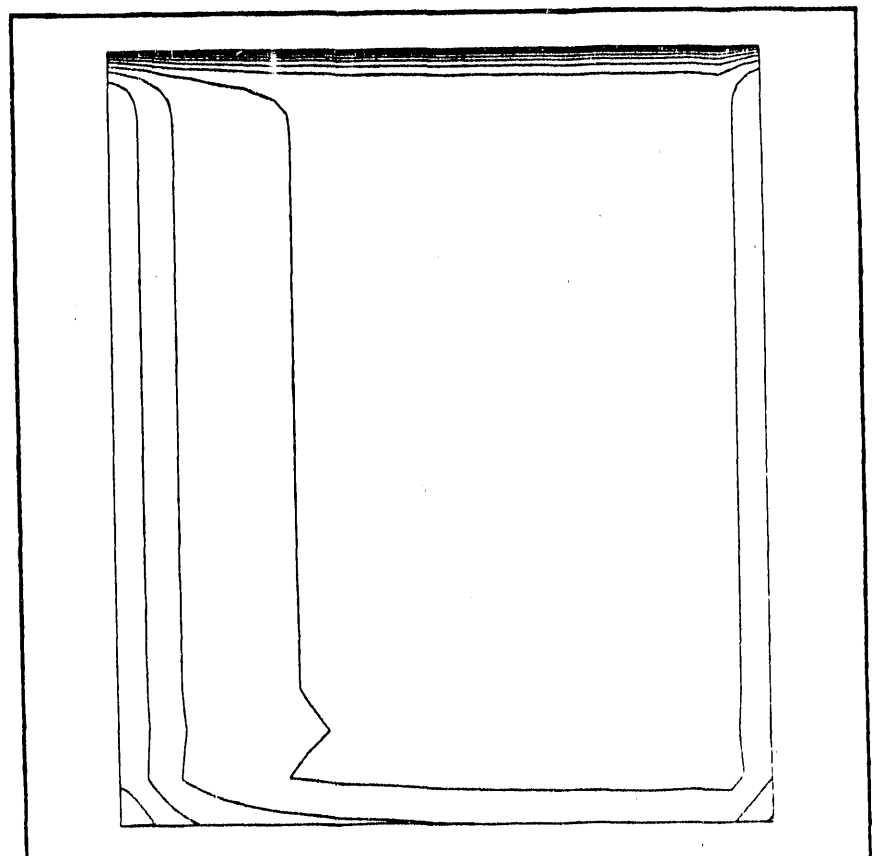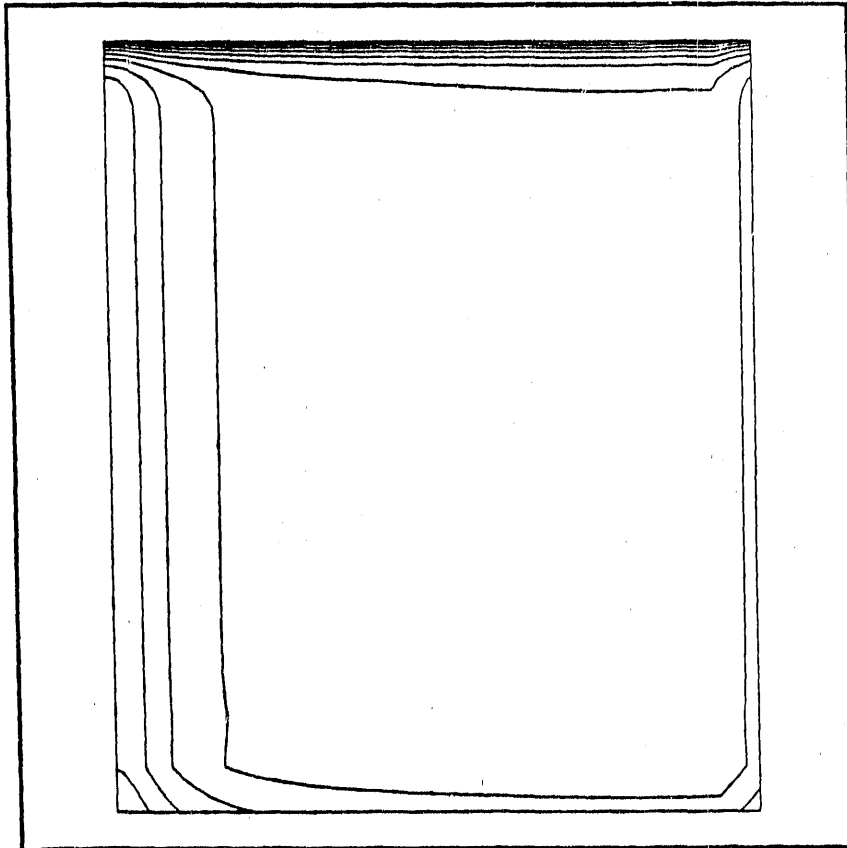
Fig. 5.3
T_{max} = 1299 at (.15,-1)
T_{min} = 1083 at (.85,0)

TIME= 410.00

Fig. 5.4
T_{max} = 1329 at (.15,-1)
T_{min} = 1073 at (.85,0)
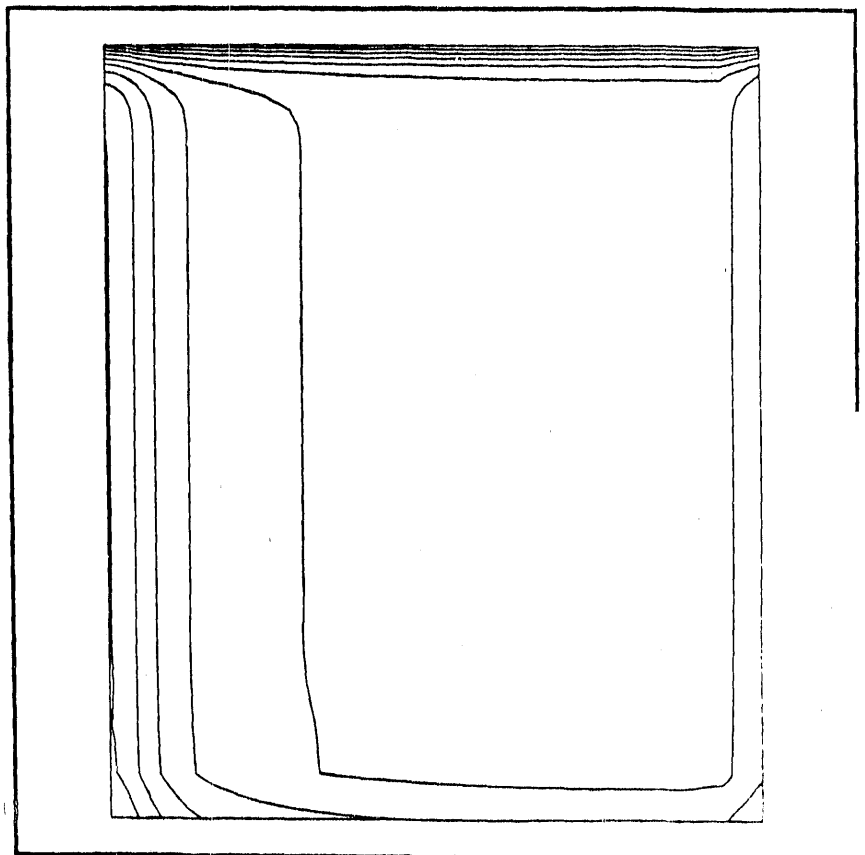
TIME= 510.00
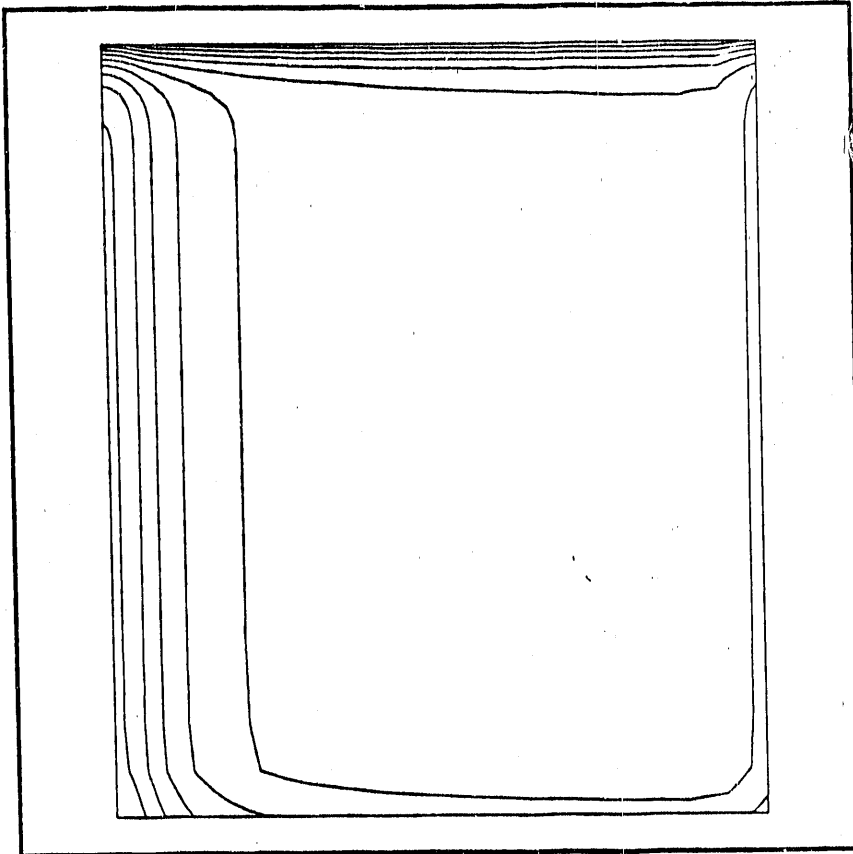
Fig. 5.5

$T_{max} = 1360$ at $(.15, -1)$

$T_{min} = 1065$ at $(.85, 0)$

TIME= 610.00

Fig. 5.6

$T_{max} = 1392$ at $(.15, -1)$

$T_{min} = 1058$ at $(.85, 0)$

TIME= 710.00

31
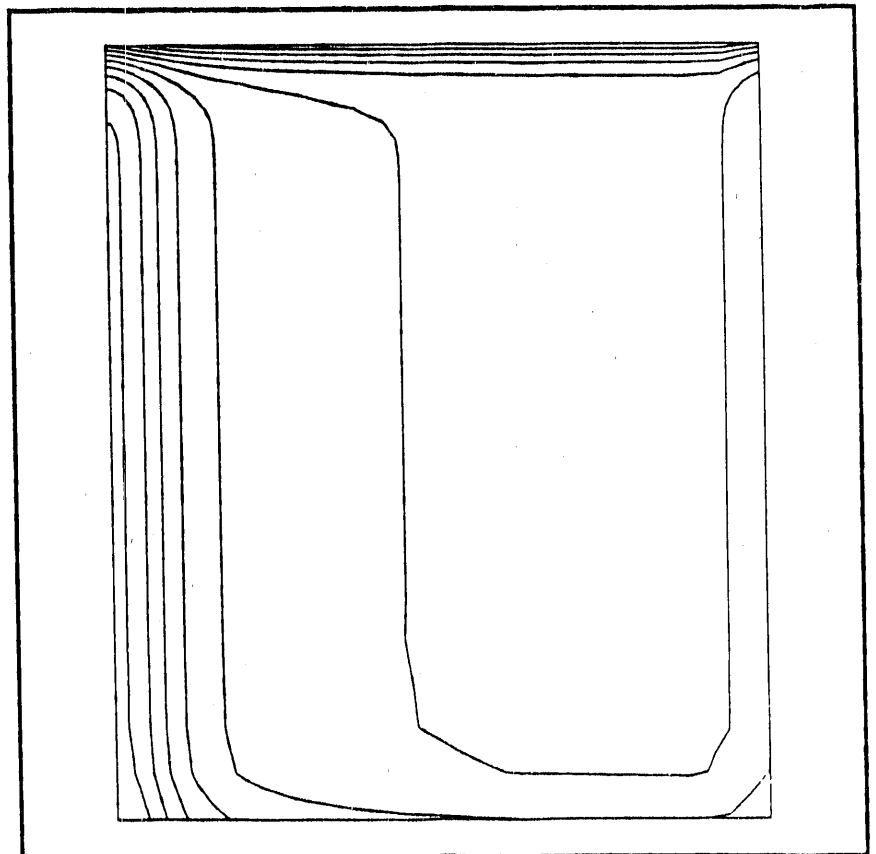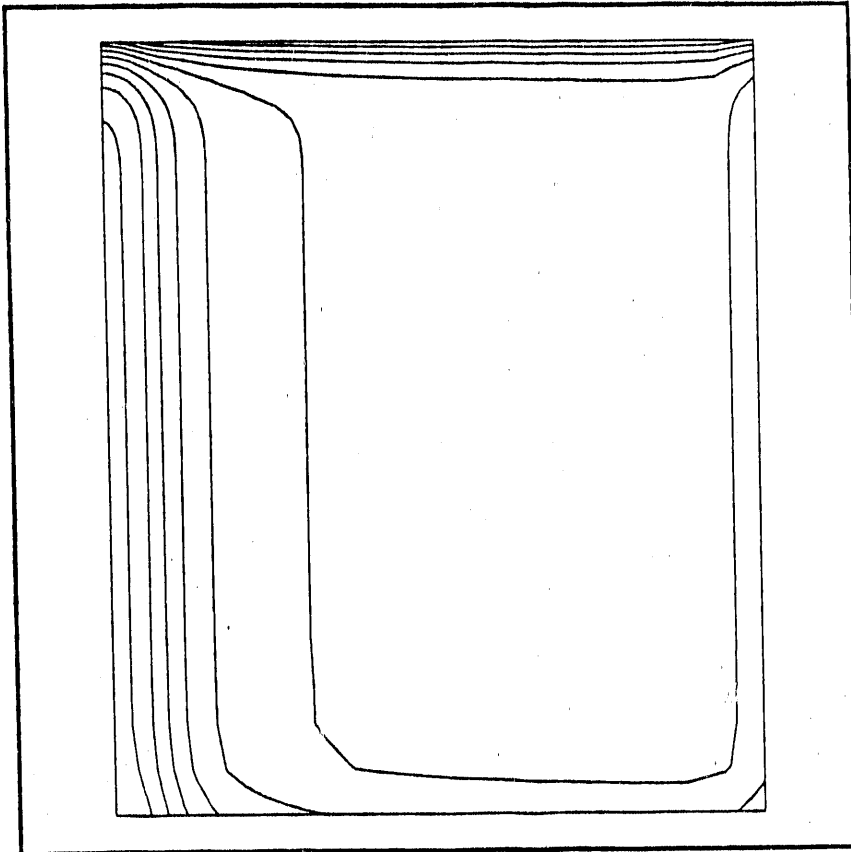
Fig. 5.7
$T_{max} = 1423$
$T_{min} = 1051$

TIME= 810.00

Fig. 5.8
$T_{max} = 1441$ at $(.17, -.76)$
$T_{min} = 1045$
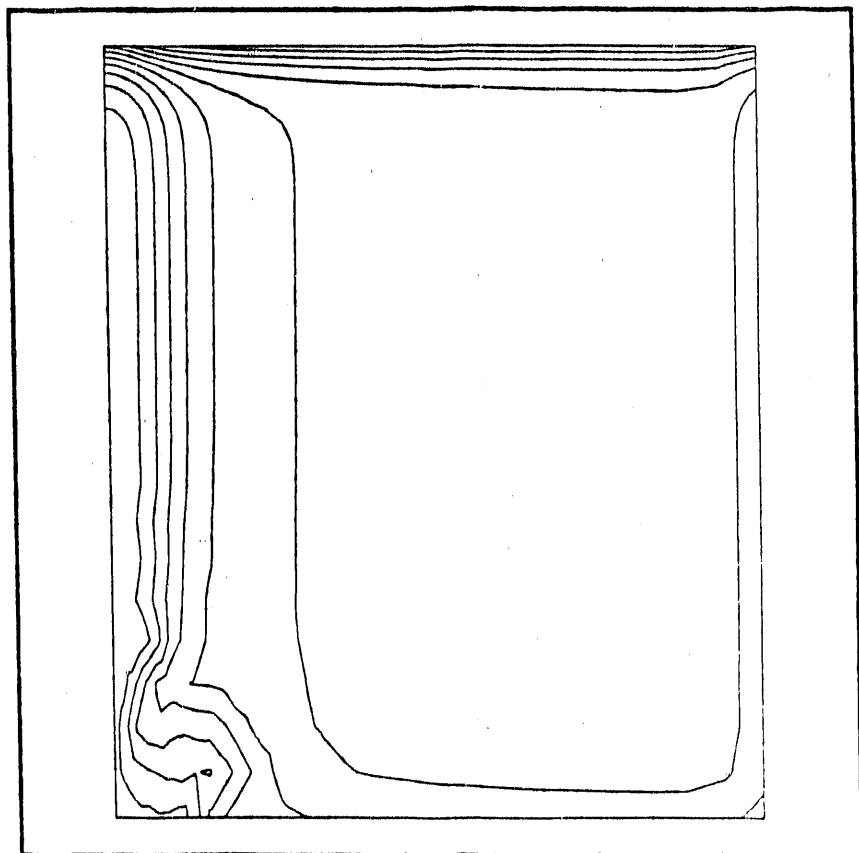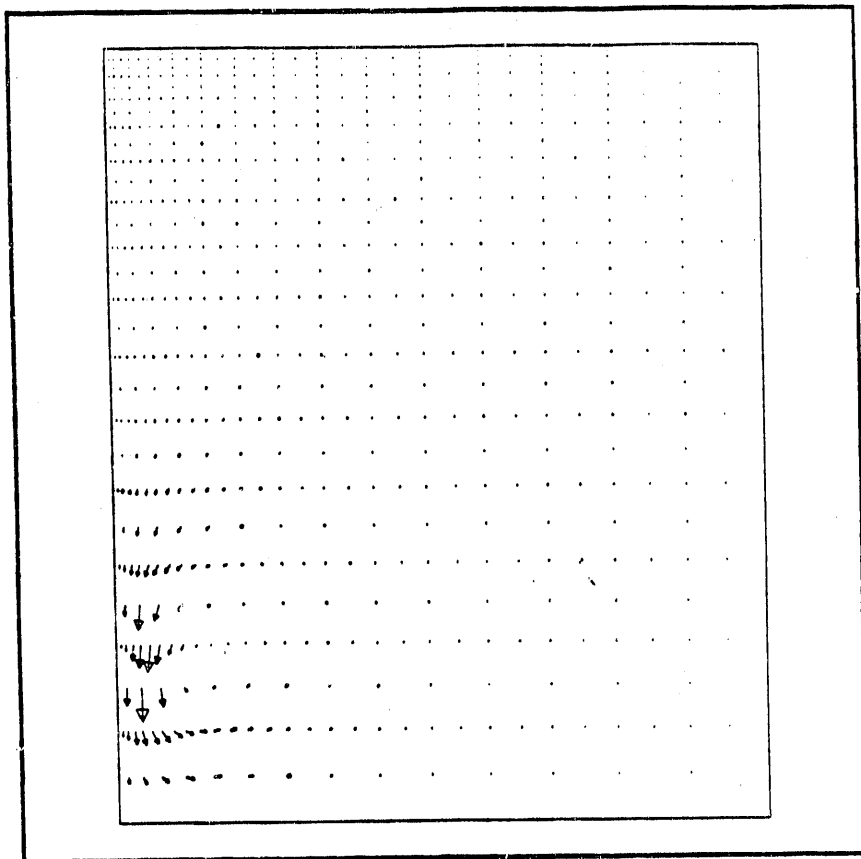
TIME= 910.00

Fig. 5.9
$V_{max} = 3.6 \times 10^{-2}$ at $(.15, -.82)$

TIME= 910.00

Fig. 5.10
$T_{max} = 1443$ at $(.15, -1)$
$T_{min} = 1040$
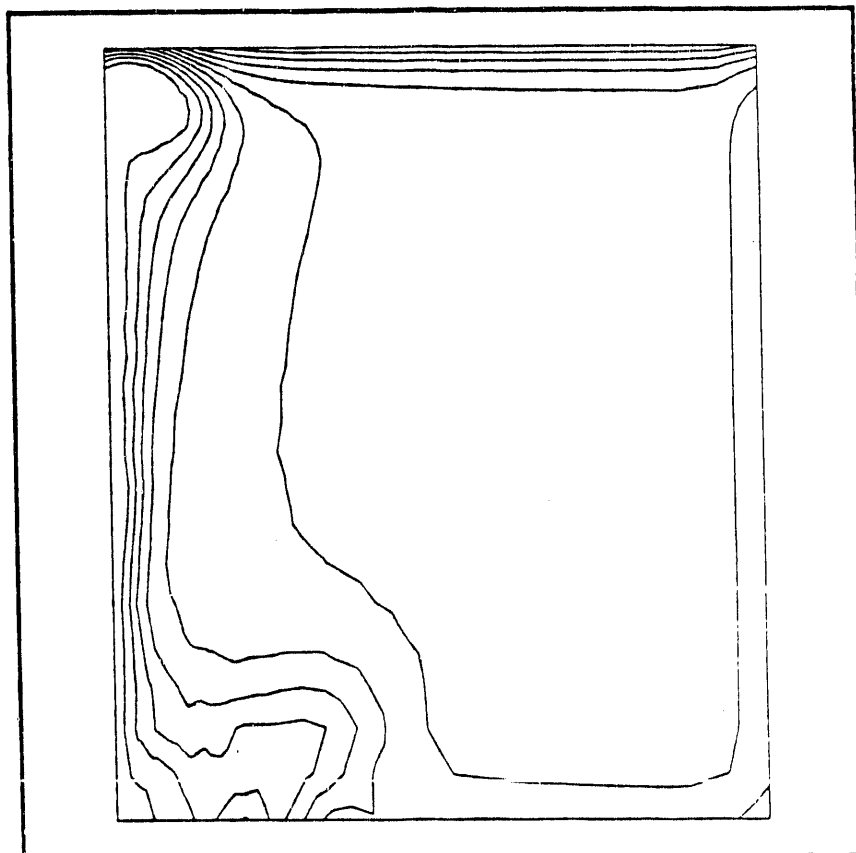
TIME= 1010.0
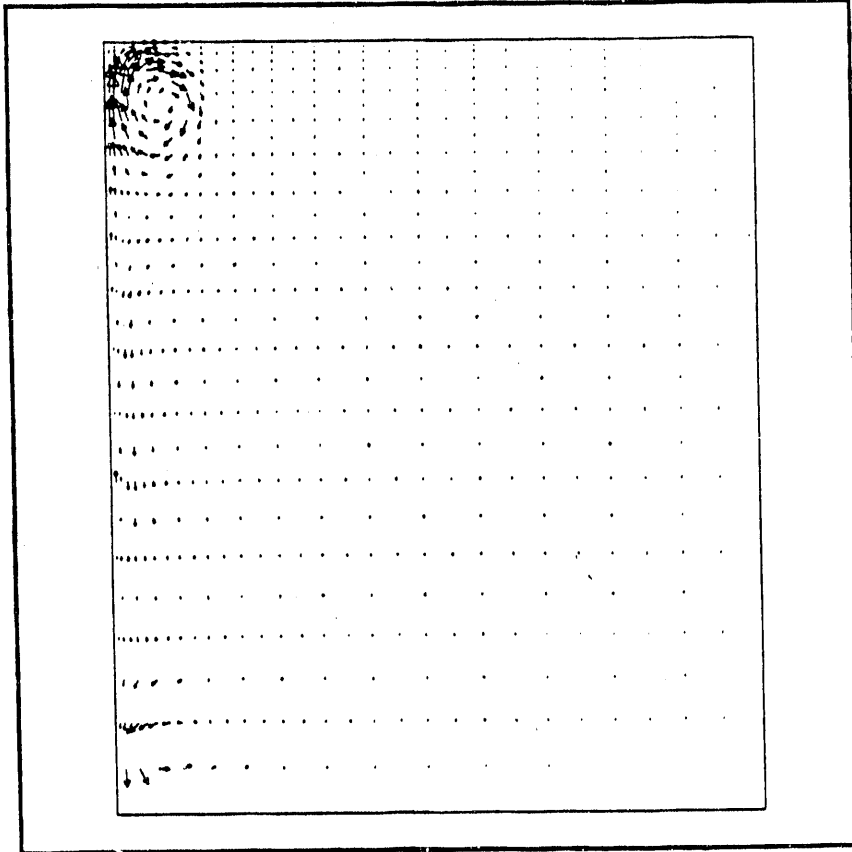
Fig. 5.11

$V_{max} = 8 \times 10^{-3}$ at $(.16, -.08)$

Fig. 5.12

$T_{max} = 1440$ at $(.15, -.02)$

$T_{min} = 1035$ at $(.85, 0)$
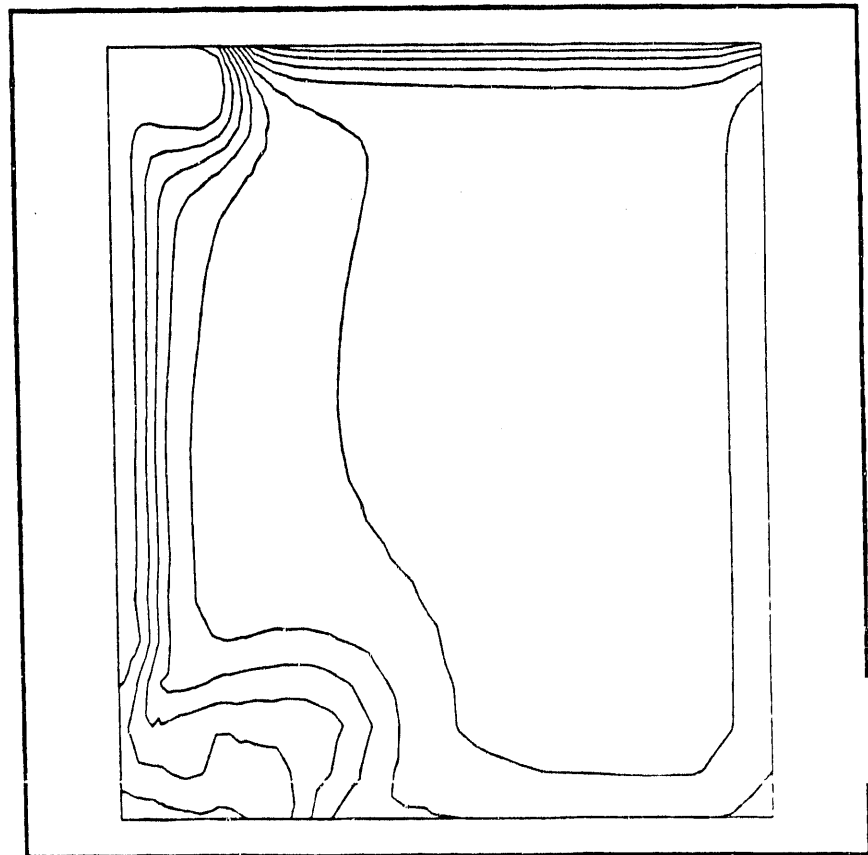
TIME= 1110.0
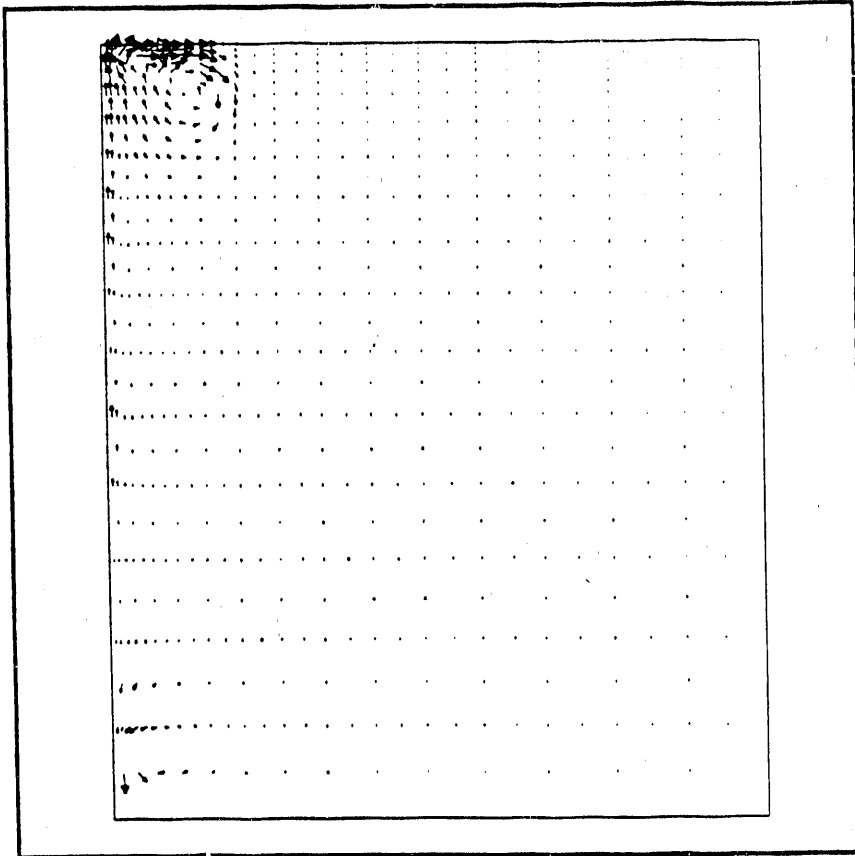
Fig. 5.13

$V_{max} = 4 \times 10^{-3}$ at $(.19, 0)$
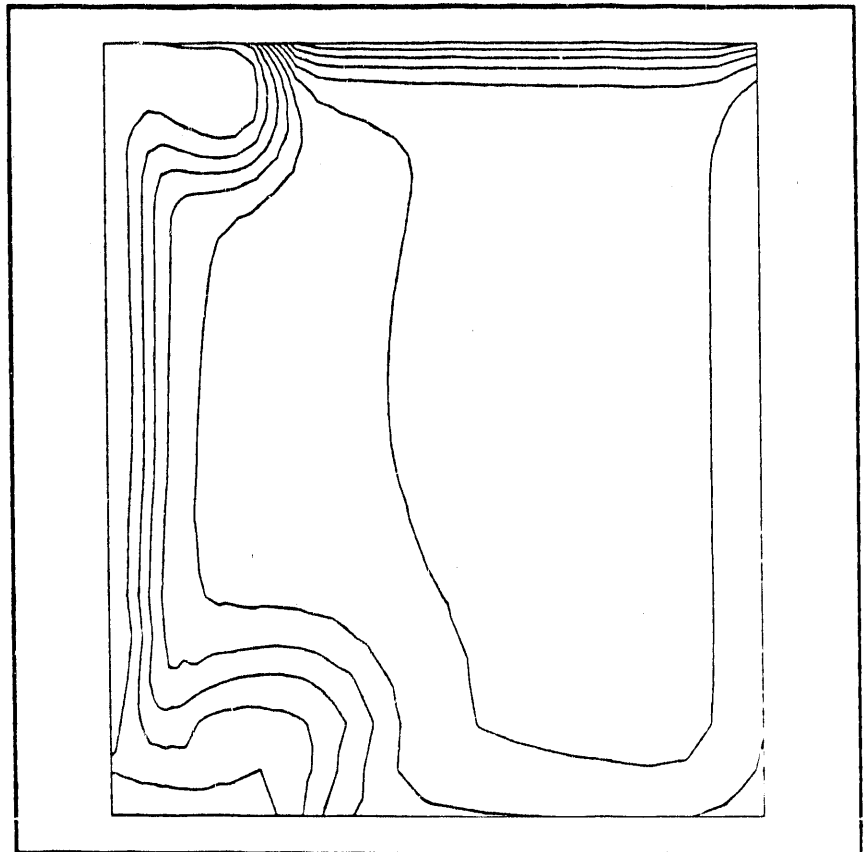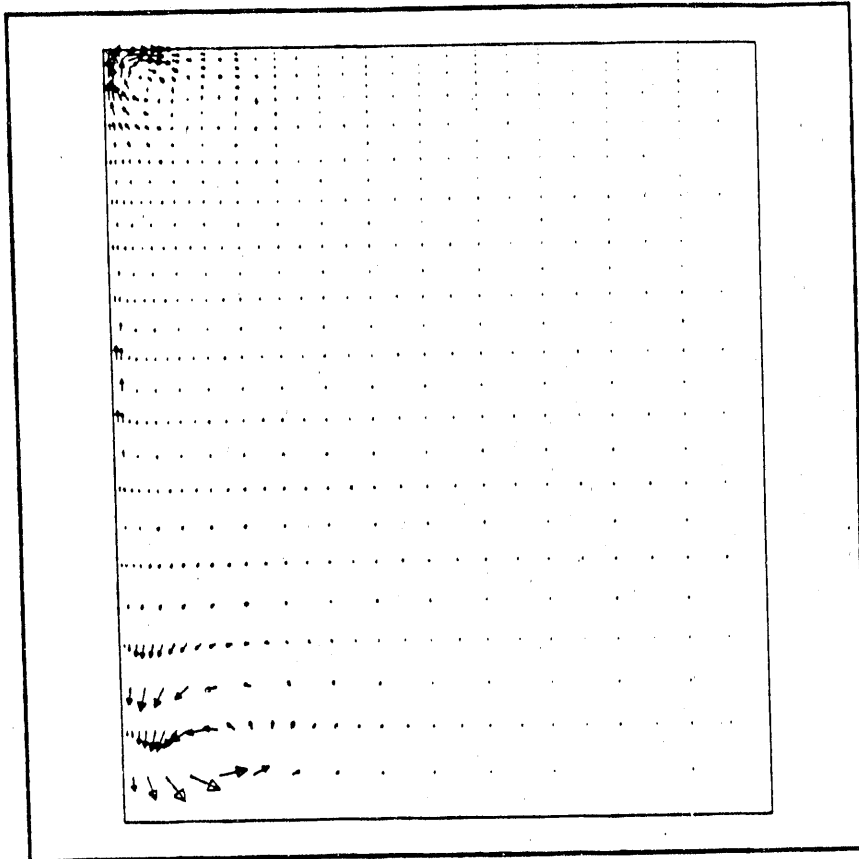
Fig. 5.14

$T_{max} = 1439$ at $(.15, -.43)$

$T_{min} = 1030$

TIME= 1210.0

Fig.5.15

$V_{max} = 7 \times 10^{-3}$ at $(.23, -0.9$

TIME= 1210.0

Fig. 5.16

$T_{max} = 1445$ at $(.17, -.77)$

$T_{min} = 1025$

TIME= 1310.0

36
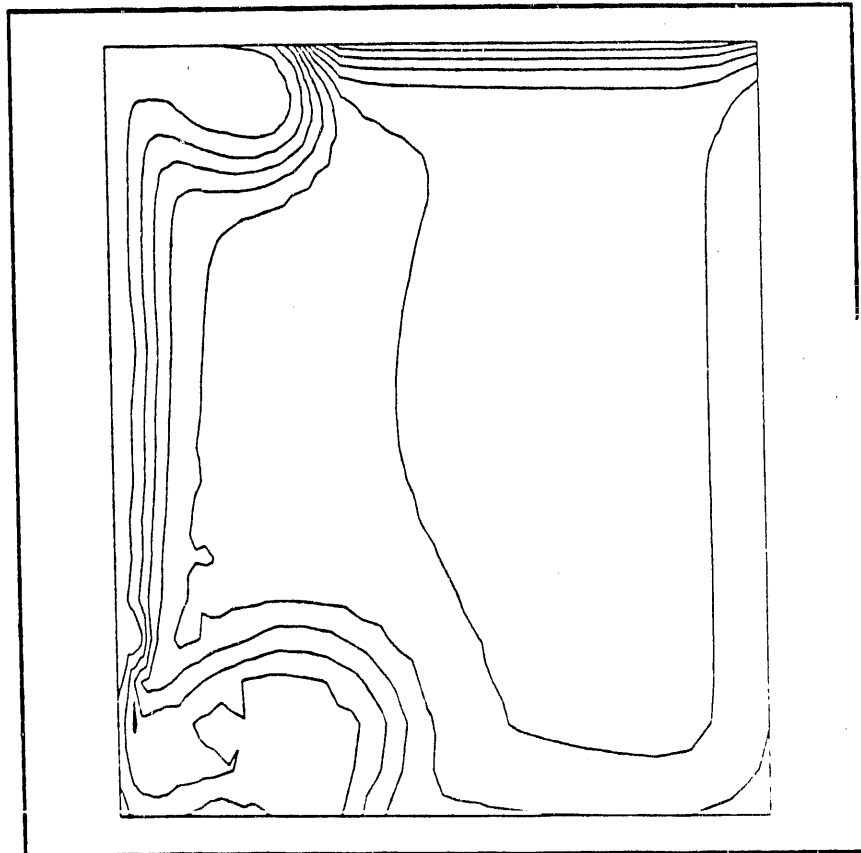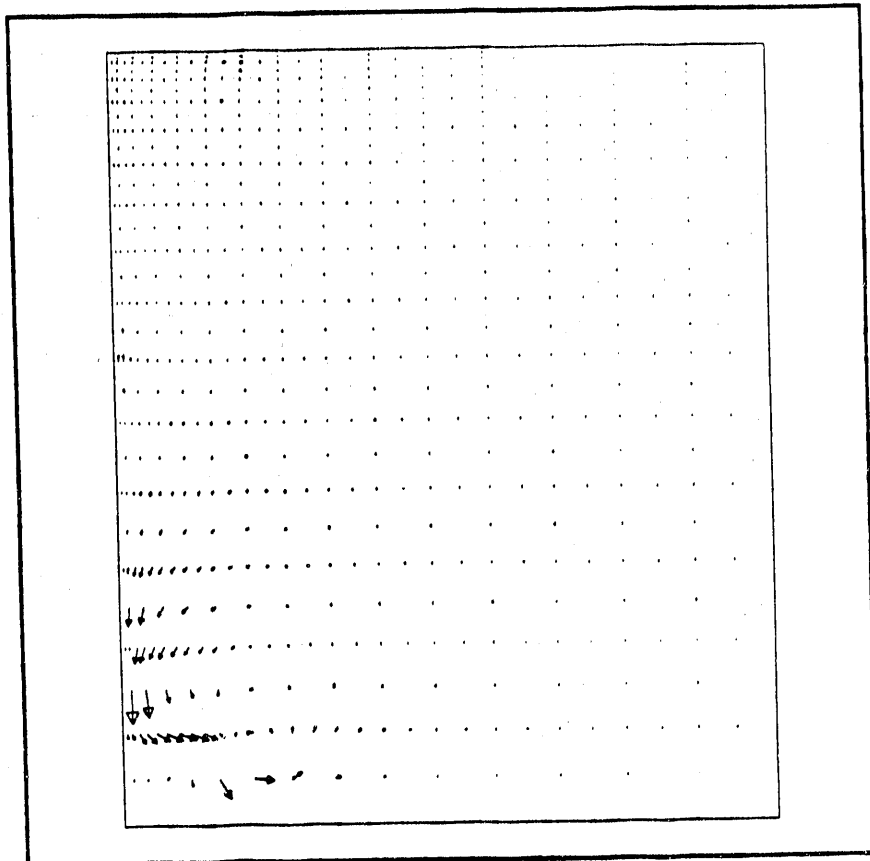
Fig. 5.17
$V_{max} = .03$ at $(.16, -.82)$

TIME= 1310.0

Fig. 5.18
$T_{max} = 1441$ at $(.15, -.01)$
$T_{min} = 1021$
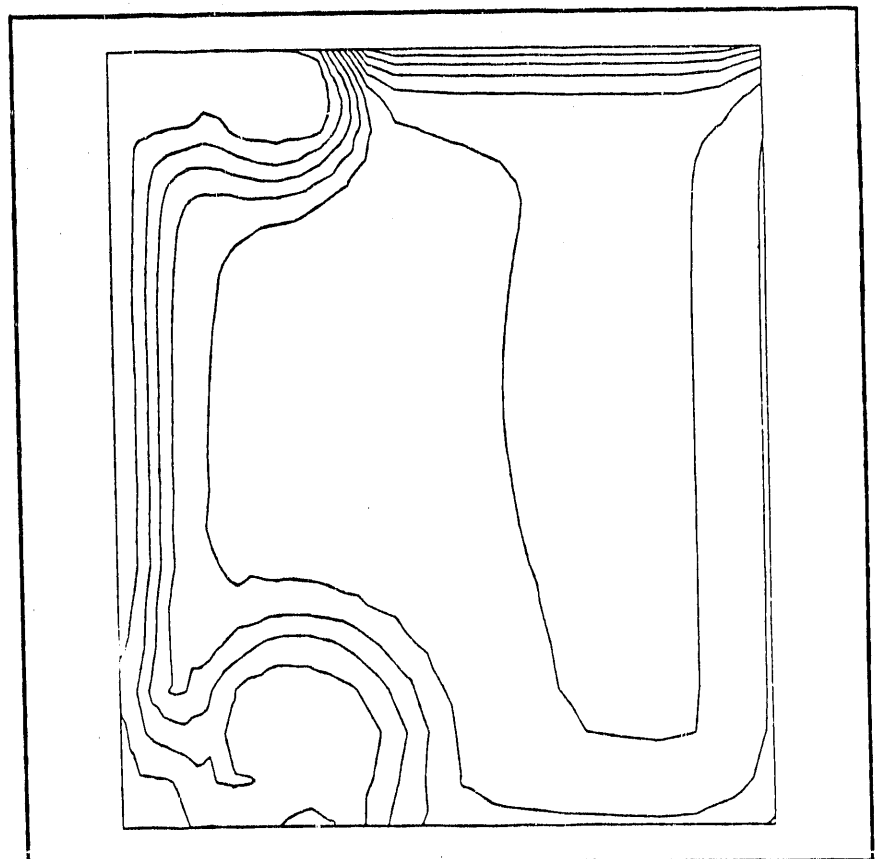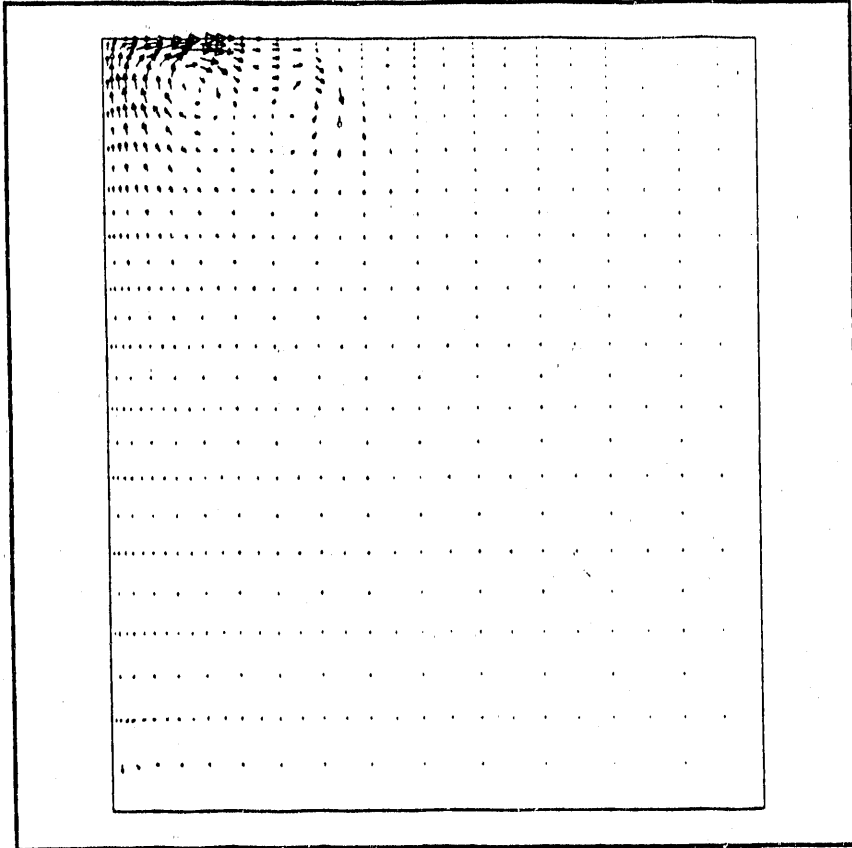
TIME= 1410.0

Fig. 5.19

$V_{max} = .014$ at $(.25,0)$

TIME= 1410.0

Fig. 5.20

$T_{max} = 1448$ at $(.17,-.77)$

$T_{min} = 978$ at $(.55,0)$
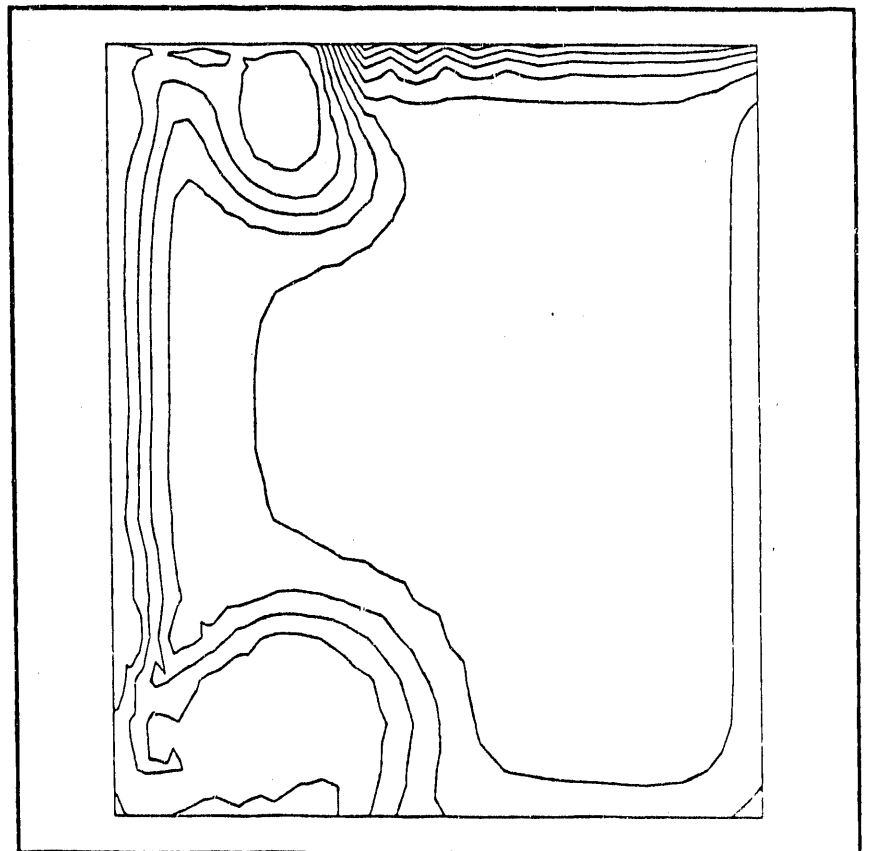
TIME= 1510.0
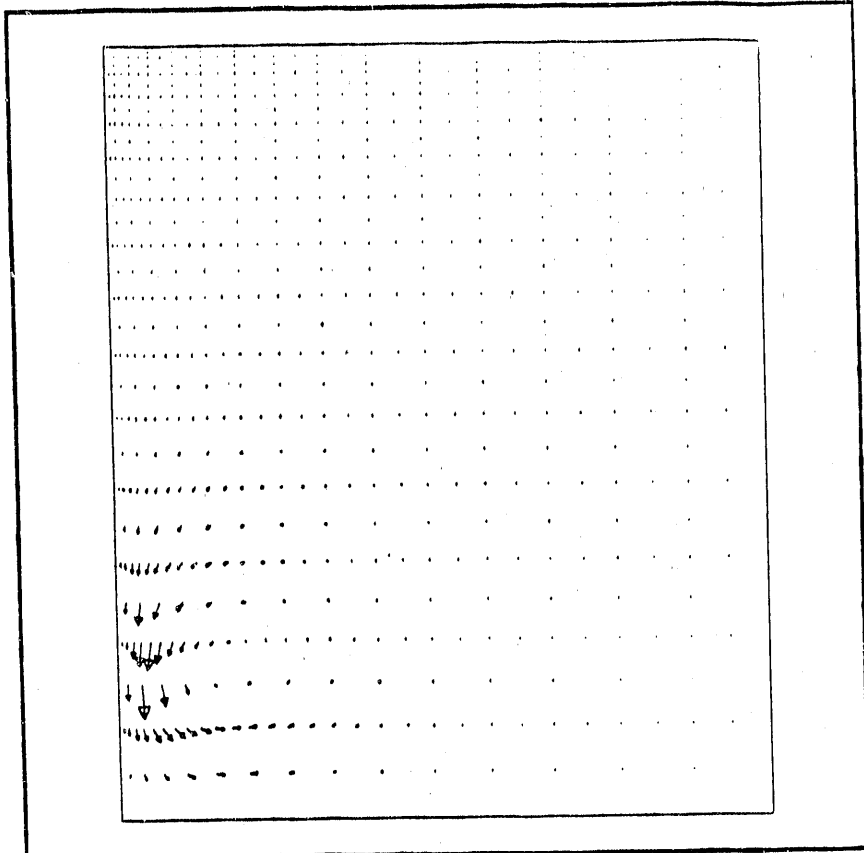
TIME= 1510.0

Fig. 5.21

$V_{max} = .09$ at $(.18, -.8)$
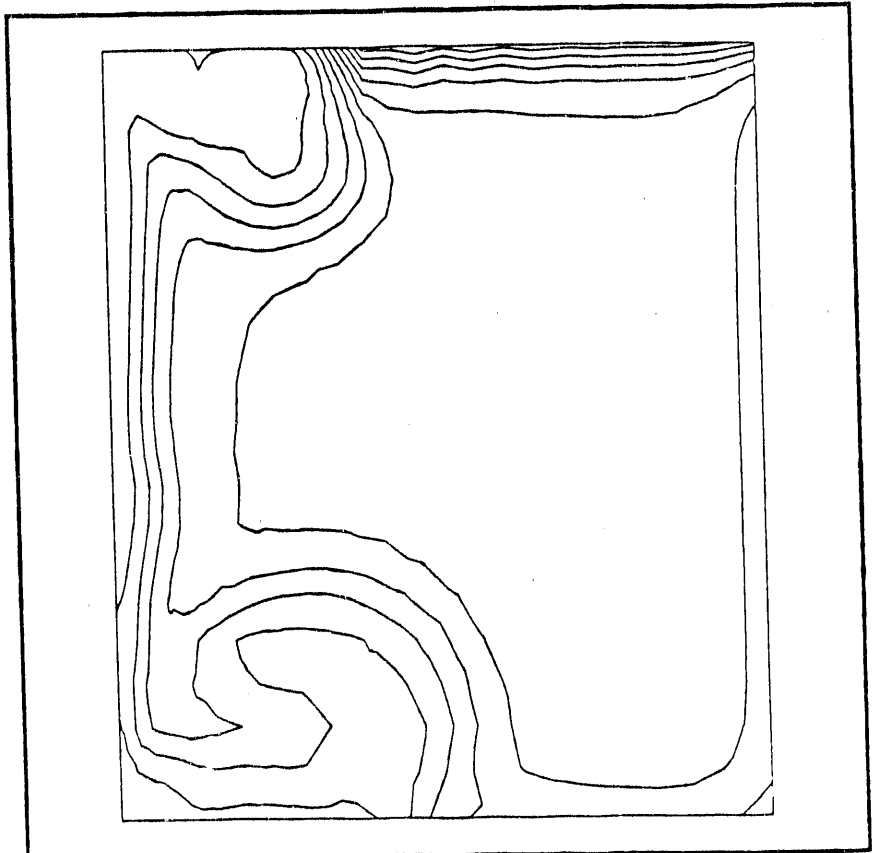
Fig. 5.22

$T_{max} = 1440$ at $(.15, -1)$

$T_{min} = 999$ at $(.55, 0)$
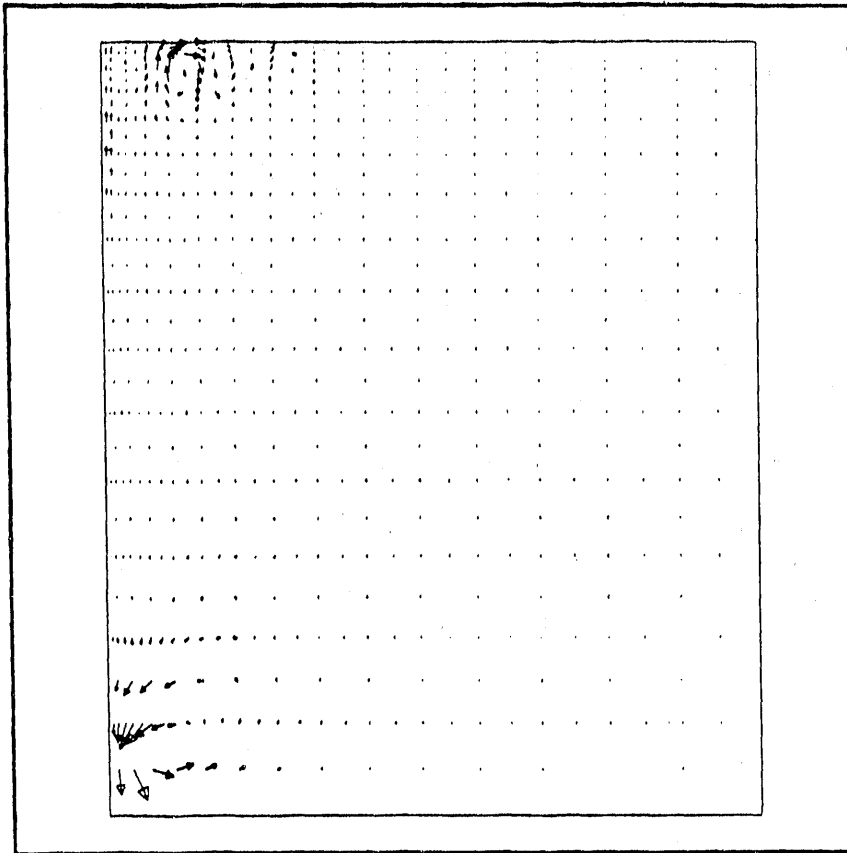
TIME= 1610.0

Fig. 5.23

$V_{max} = .008$ at $(.18,-.94)$

TIME= 1610.0

Fig. 5.24

$T_{max} = 1441$ at $(.15,-.014)$

$T_{min} = 1007$ at $(.55,0)$

TIME= 1710.0

40
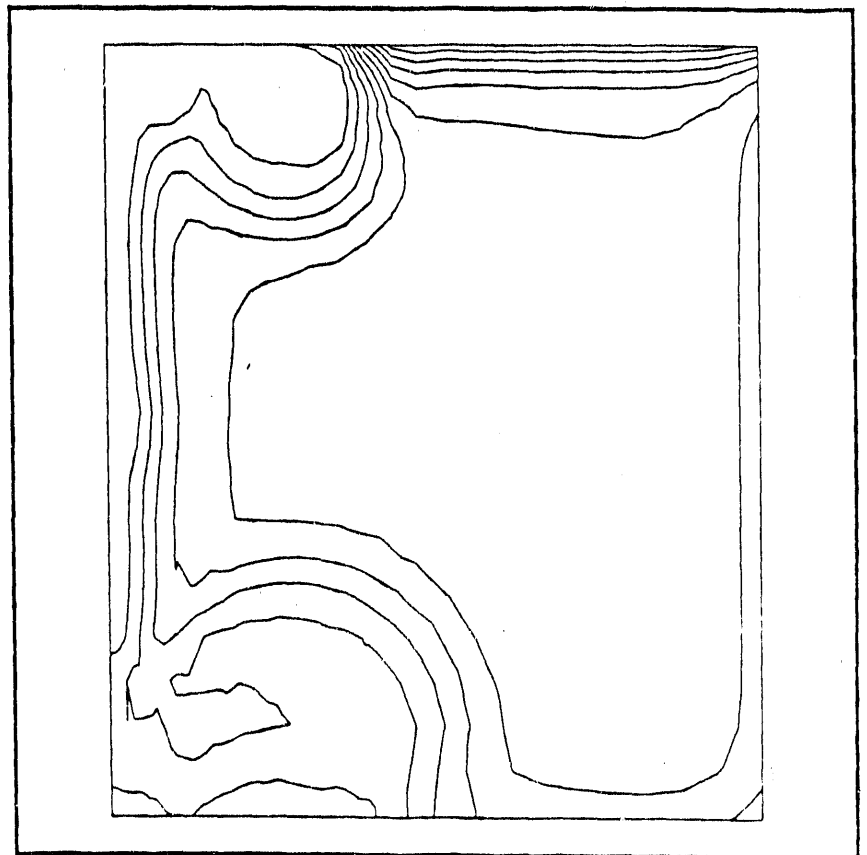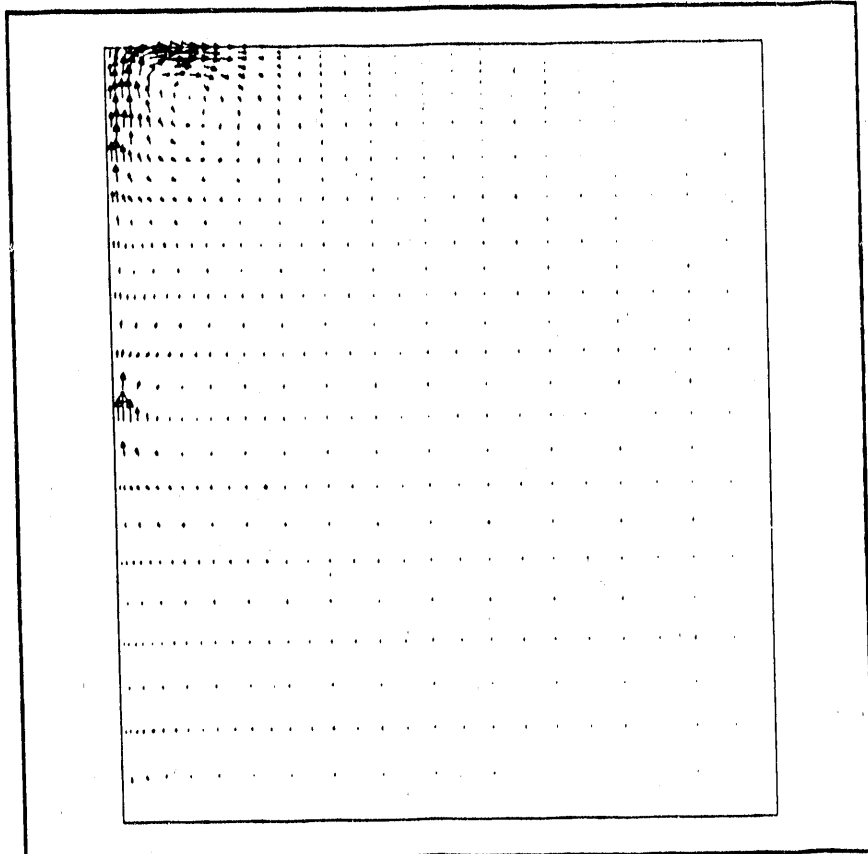
Fig. 5.25

$V_{max} = .012$ at $(.2, 0)$

Fig. 5.26

$T_{max} = 1441$ at $(.15, -.014)$
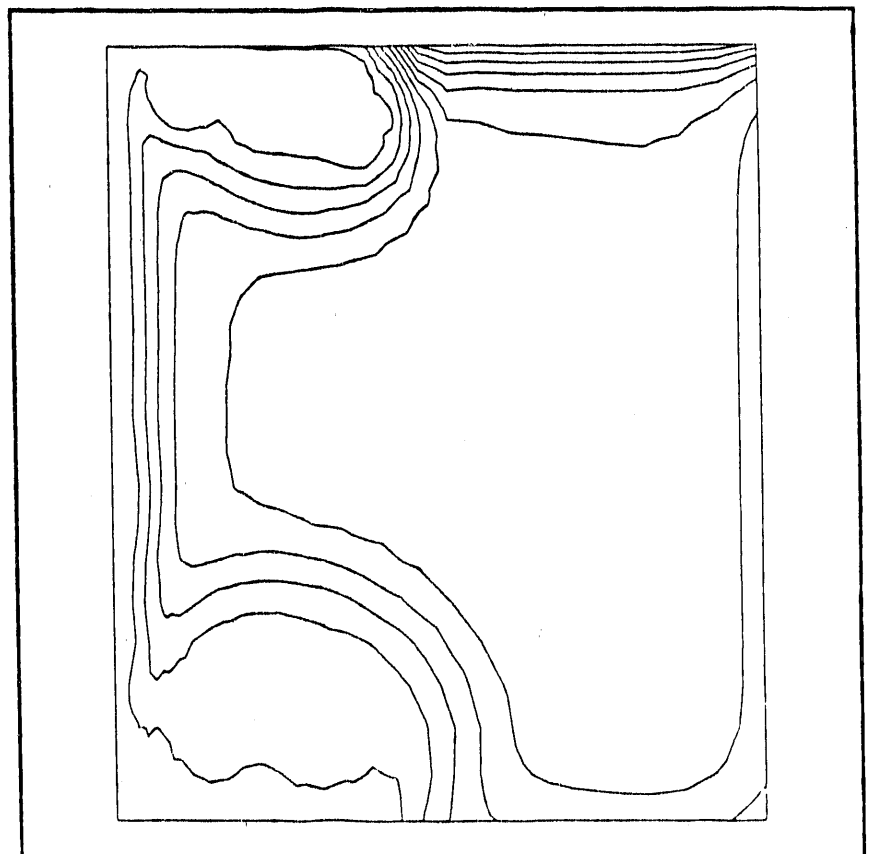
$T_{min} = 1010$
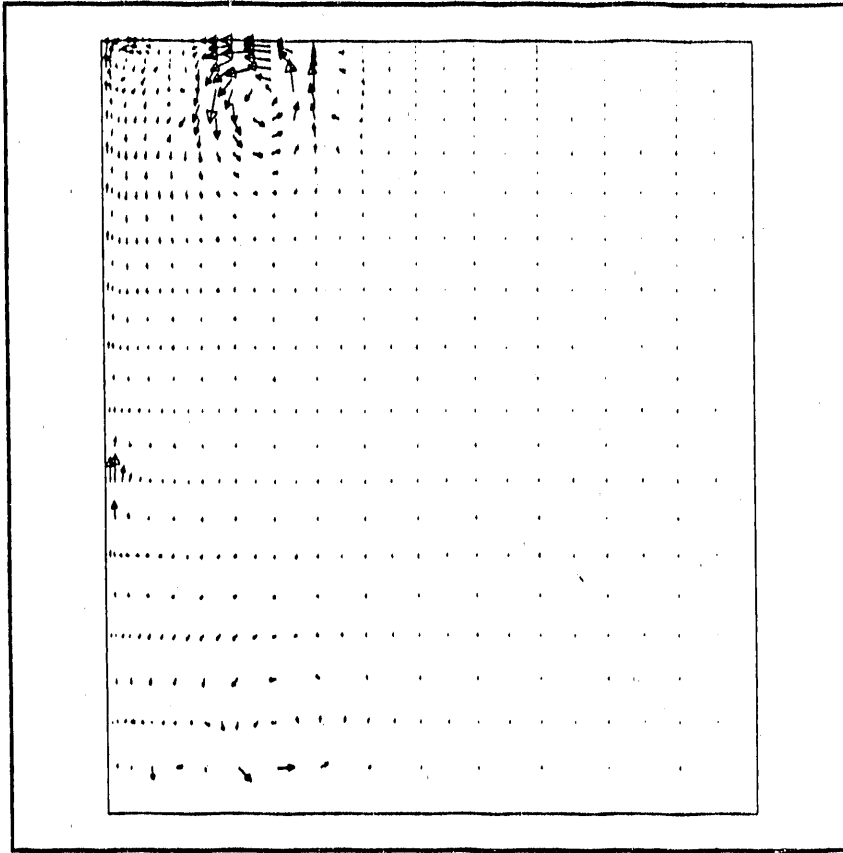
TIME= 1810.0

Fig. 5.27
V_{max} = .007 at (.29,-.06)

Fig. 5.28
T_{max} = 1649 at (.15,-1)
T_{min} = 1007 at (.75,0)
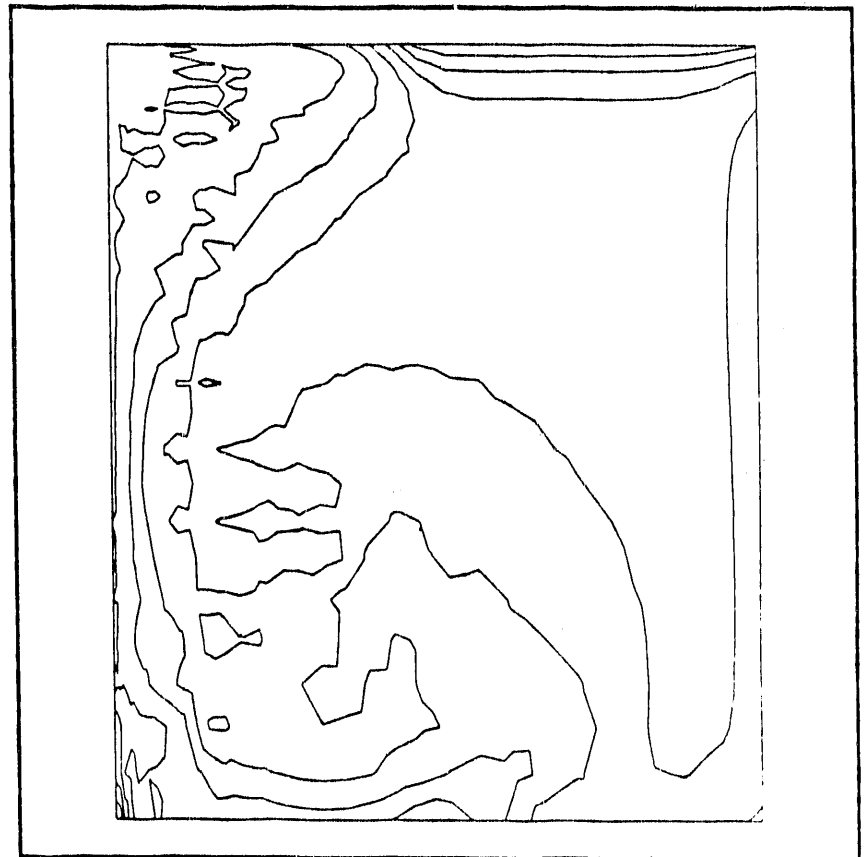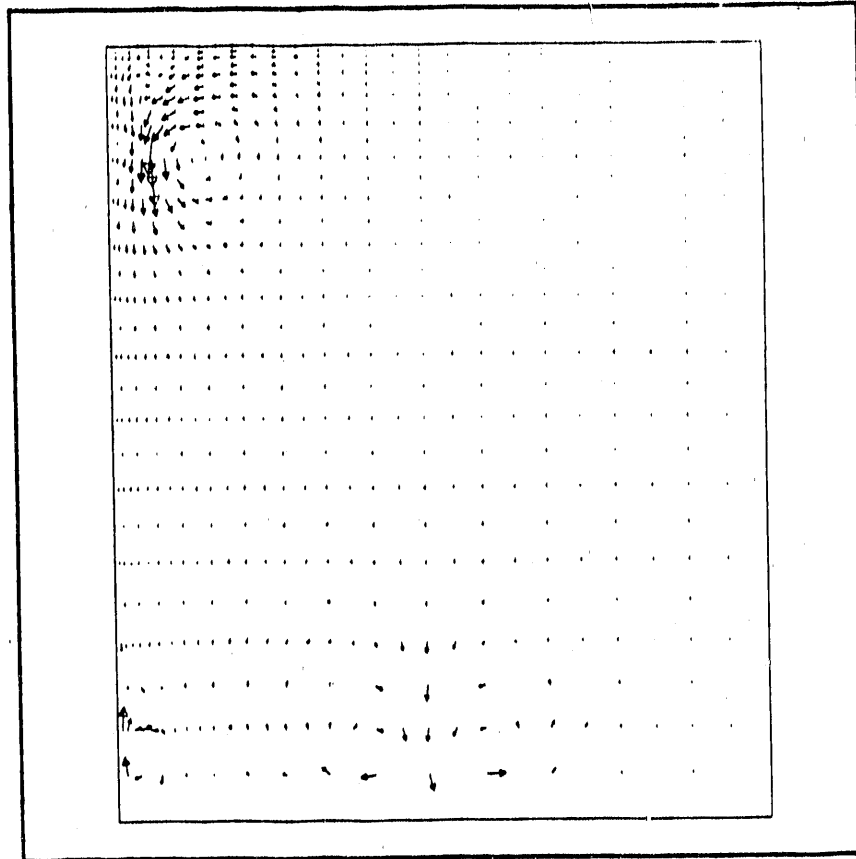
TIME= 1910.0

Fig. 5.29 $V_{max} = .15$ at $(.2, -.12)$

6. LATENT HEAT

The Stefan condition describes the motion of the boundary as $\bar{s}$

$$L\bar{s} = \left[k \frac{\partial T}{\partial n} \right] \tag{6.1}$$

where L is volumetric heat of fusion. To non-dimensionalize our problem, let $\alpha = k\rho c_\rho$; $t_o = \ell^2/\alpha$; $t = t/t_o$; $= T/(T_m - T_i)$; $x = \chi/\ell$; $= \bar{s}/\ell$ so that the Stefan condition (6.1) becomes

$$\left[\frac{\partial \theta}{\partial \bar{x}} \right] = \frac{1}{St}\bar{s}; \quad St = \frac{\rho c_p (T_m - T_i)}{L} \tag{6.2}$$

Here, T_m is the melt temp, T_i is the initial temperature and St is the Stefan number. In particular let us take soil with the following properties:

$$
\begin{aligned}
\rho &= 2170\text{kg/m}^3 \\
c_p &= 1046\text{J/kg}^\circ\text{K} \\
T_m &= 1428^\circ\text{K} \\
T_i &= 300^\circ\text{K} \\
\lambda &= 2.37 \times 10^5 \text{ J/kg} \\
L &= \rho\lambda = 5.14 \times 10^8 \text{ j/m}^3
\end{aligned}
$$

Then

$$St = (2170\text{kg/m}^2)\,(1046\text{J/kg}^\circ\text{K})\,(1428 - 300^\circ\text{K}) \left[\frac{1\text{m}^3}{5.14 \times 10^8 \text{ J}} \right]$$

so $St \sim 5$.

When St is small, as in an ice-water system ($St \approx 10^{-2}$), most of the thermal energy travelling across the melt interface goes into converting

44

material from solid to liquid. However, in the present case where St is in the range of 1 to 10, the thermal energy is balanced between latent heat and heat capacity effects.

An estimate of how important the latent heat is to the position of the melt surface can be estimated as follows. Consider a one-dimensional problem on (0,1). Linearly interpolate the temperature between 1522°K at χ = 0 and T = 300°K at χ = 1.0 as initial data. These temperatures are chosen so that the melt temperature of 1400°K is initially at χ = 0.1. At time t = 0, the left boundary is raised to 2200°K. The temperature is then computed and the melt boundary position is followed as a function of time using a moving boundary finite element technique.

To estimate the relative importance of latent heat, the position of the melt boundary is tracked with and without latent heat (see Figure 6.1). Results show that if latent heat is ignored the boundary position is overestimated by about 20%.
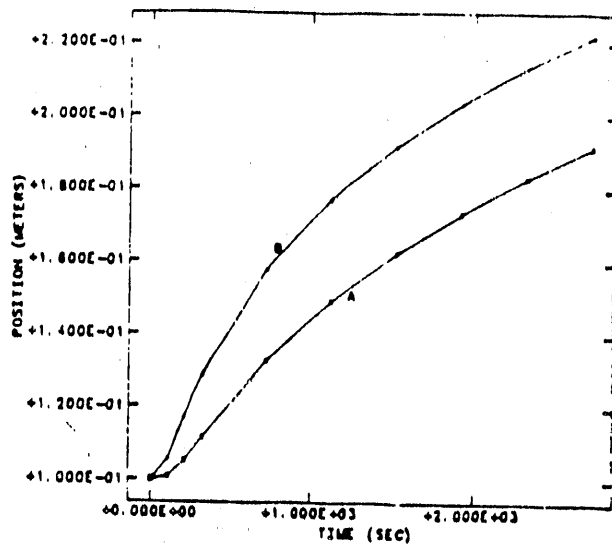
FIGURE 6.1

Figure 6.1. Melt interface position vs. time for material with (A) and without (B) latent heat for St = 4.

46

7. CONDUCTION IN A LARGER DOMAIN

In this section the problem of conduction (only) is considered in a larger domain (5m radius and 5m deep) with a .3m x .25m subregion Ω_2 at the top left corner initially heated at T = 1428°K. The remainder of the region is initially assumed to be at T = 300°K . Part of the purpose of the present study is to provide a qualitative check on these calculations and to verify numerical accuracy and algorithm reliability.

A radiative boundary condition applies at the top surface for .15 < r < 0.5m with ϵ = 0.9, T_∞ = 843°K, and a convective boundary condition for 0.5 < r < 1m, with heat transfer coefficient h = 0.1 and T_∞ = 300°K (simulating the exterior to a cover). At the inner radius, r = 0.15, symmetry implies flux q = 0. At the remote sides and bottom a convective boundary condition with h = 0.1 and T_∞ = 300°K is applied as before. The material properties for ρ, μ, C_p, k, β are given previously. The electrical conductivity $(1/\Omega_m)$ is given by

$$\sigma_E = \begin{cases} 1.0 & T < T_m \\ m(T - T_m) + 1 & T > T_m \end{cases}$$

with m = 19/850 and T_m = 1428°K. The heating model is taken to be

$$Q = \begin{cases} J^2/\sigma_E, & T > T_m \\ 0, & T < T_m \end{cases}$$

where J = 774.6A/m. Note that in this model Q = 0 in the solid region, where T < T_m. In particular, initially Ω_1 is solid with Q = 0. This model then differs from previous models that tend to provide a large bulk source of heat in the solid region which accelerates global heating and melting. Therefore, the results may be quite different, with local heat generation in the molten regions and heat transfer by conduction in the solid due to the presence of the molten pool.

47

The grid for this extended domain is graded towards the electrode on the left (at r = 0.15m) and towards the top surface as shown in Figure 7.1. Temperature contours are labeled in the plots with a minimum temperature contour being A and the maximum contour J. The contours at t = 1000 seconds are shown in Figure 7.2 along with a strong gradient from the melt isotherm into the solid region. By t = 29000 seconds the heat zone has grown slightly and the effects of the radiative surface condition are evident in the crowding of contours at the top innermost region as well as the "lobe" to the right at the surface in Figure 7.3. By time 1.16×10^{-5} seconds the zone has grown further but has the same qualitative form. The effects of the far field boundary conditions clearly are negligible.
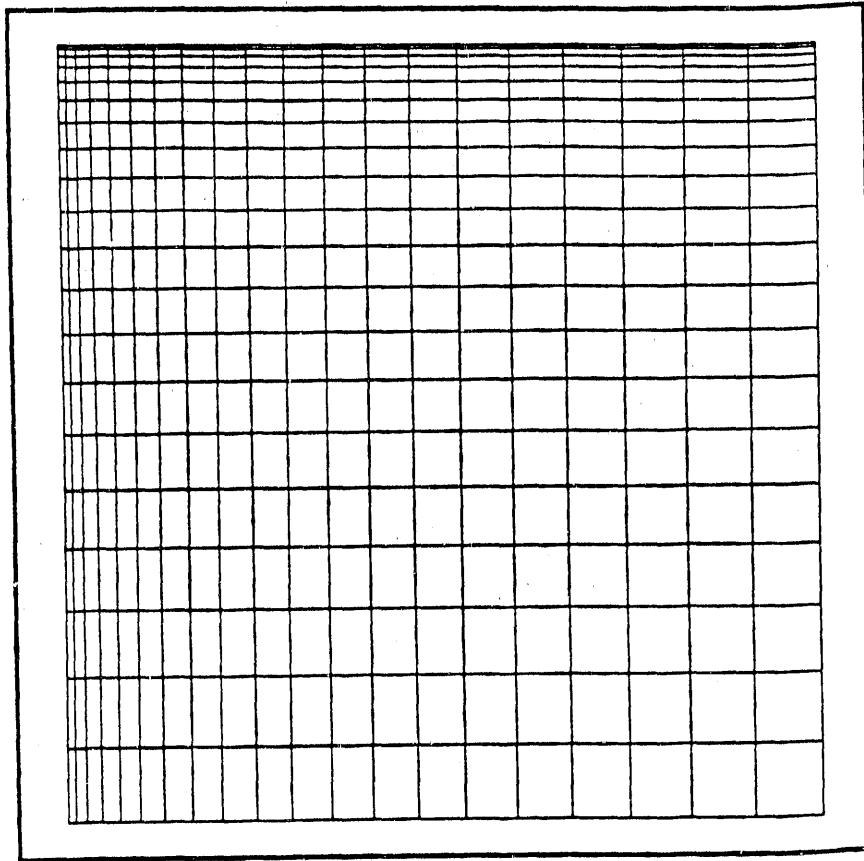
Fig. 7.1

Fig. 7.2
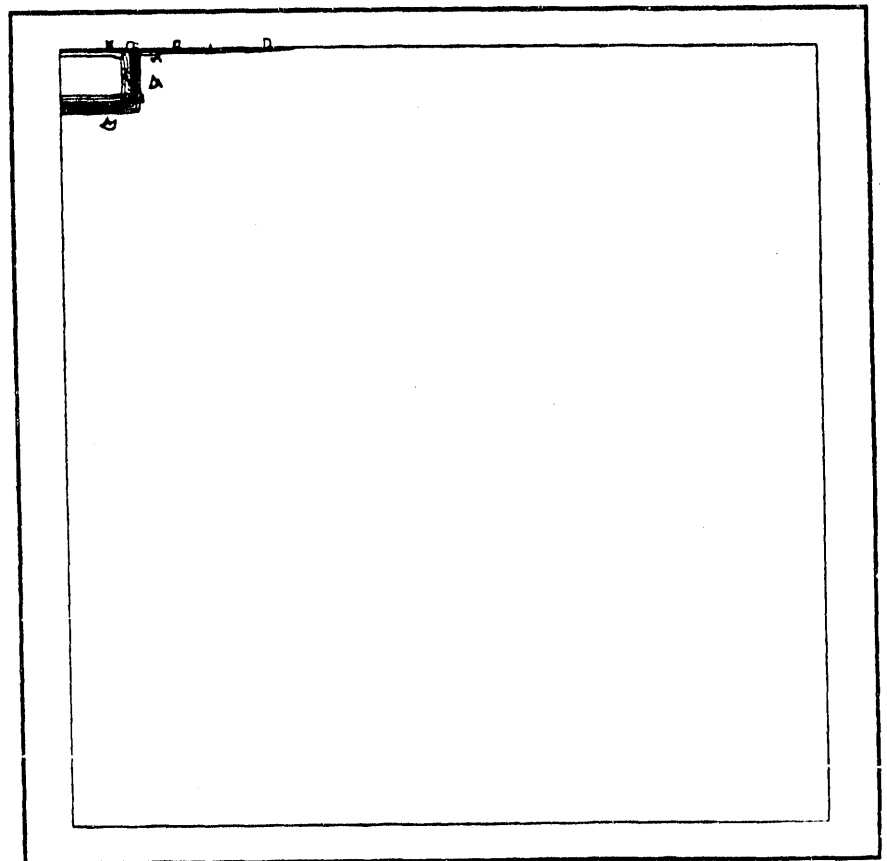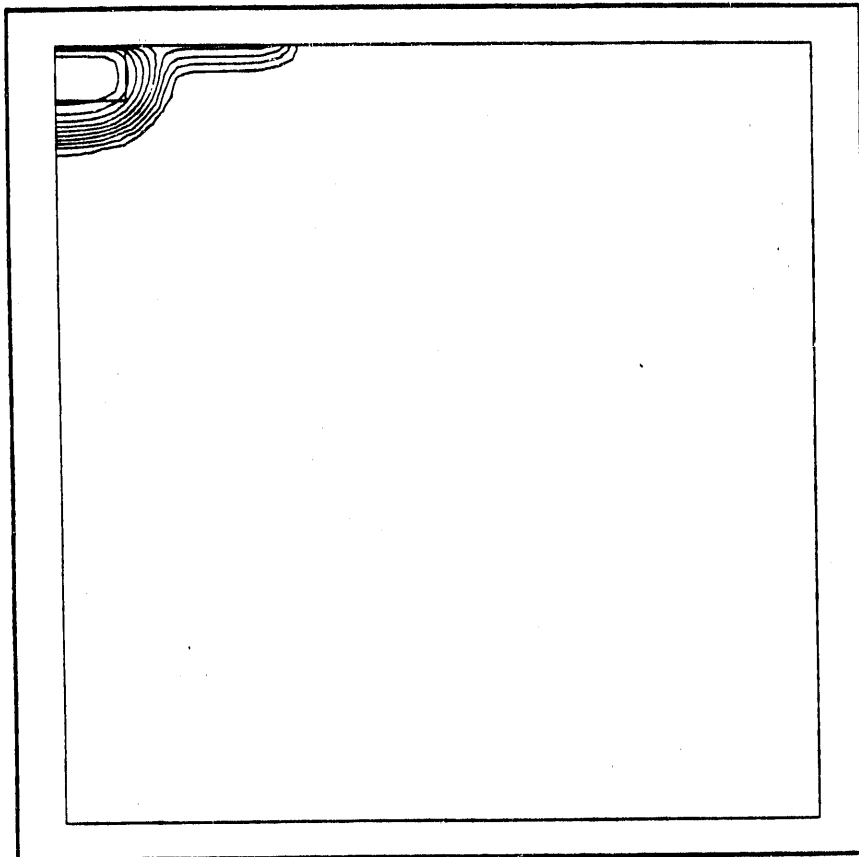
Fig. 7.3

TIME= 29000.
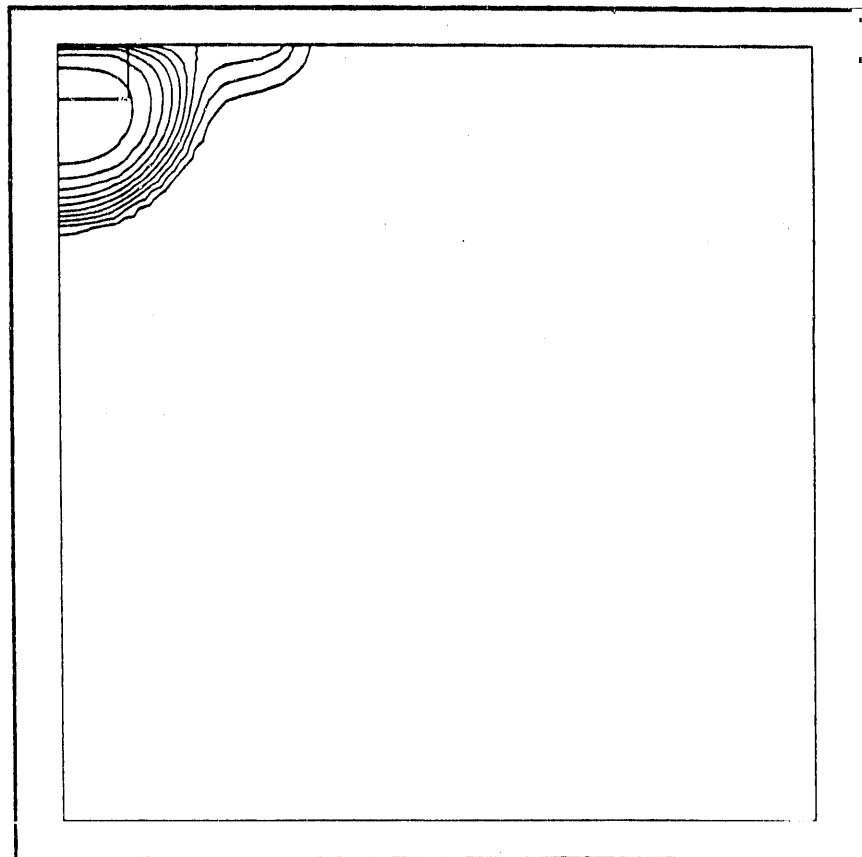
Fig. 7.4

TIME= 0.11600E+06

8. CONDUCTION AND CONVECTION

In the next case both conduction and convection were included and the initial melt zone Ω_2 was taken to be a melted "frit" type region extending across the top of a 1m X 1m domain. This zone extends down to 0.13m and is at 1428°K initially. The radiative boundary condition applies across the top surface and the previous heat flux condition is applied at the other boundaries. The time step for the calculations is Δt = 1500 seconds. Since the hot region extends to the far right boundary there will be an interaction with a convective outer wall boundary condition.

The grid is given in Figure 8.1 and the isotherms in Figure 8.2, at t = 9000 seconds, indicate that conduction is dominant in the early time period. Note the clustering of contours near the surface and in the solid region due to the radiative boundary condition and high capacitance of the solid, respectively. At t = 54000 seconds the convective effects in the melt zone are becoming apparent as seen in the isotherm contours of Figure 8.3. The associated convective rolls in Figure 8.4 contain a primary roll and two secondary counter rotating rolls. The trend continues in Figures 8.5 and 8.6 at t = 61500 seconds and by t = 99000 seconds a large melt zone with strong convective effects occurs due to a single convective cell having maximum velocity of .015m/s, at (.5,-.37). The effect of convection is to produce a well mixed approximately uniform temperature zone. Some minor effects associated with the boundary conditions at the right boundary are apparent.
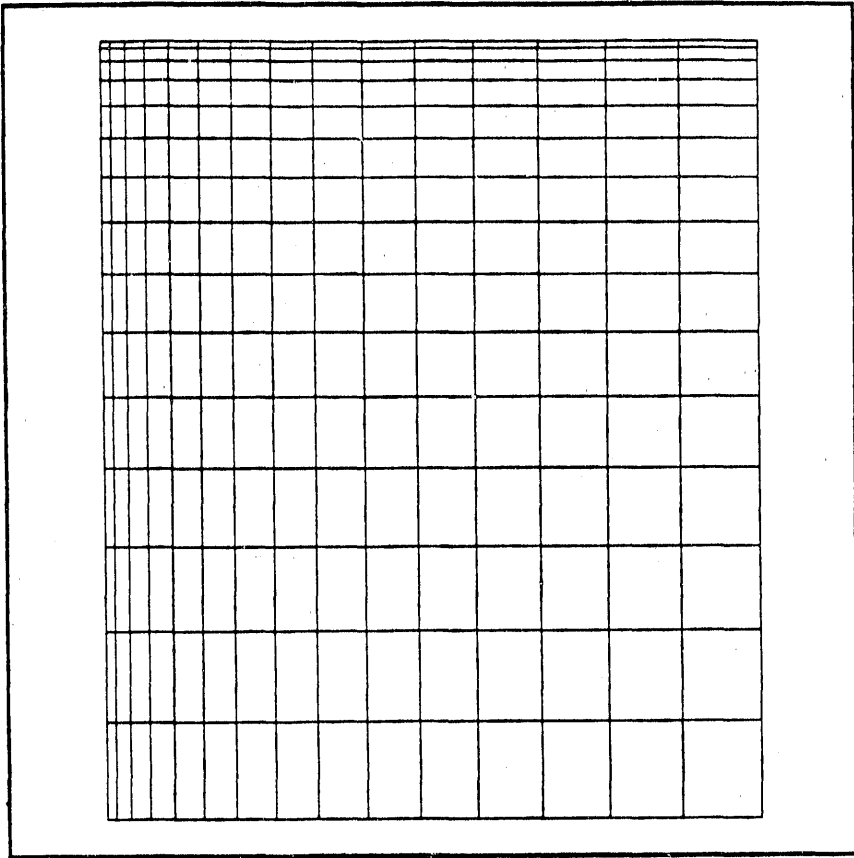
Fig. 8.1

Fig. 8.2

TIME= 9000.0

52
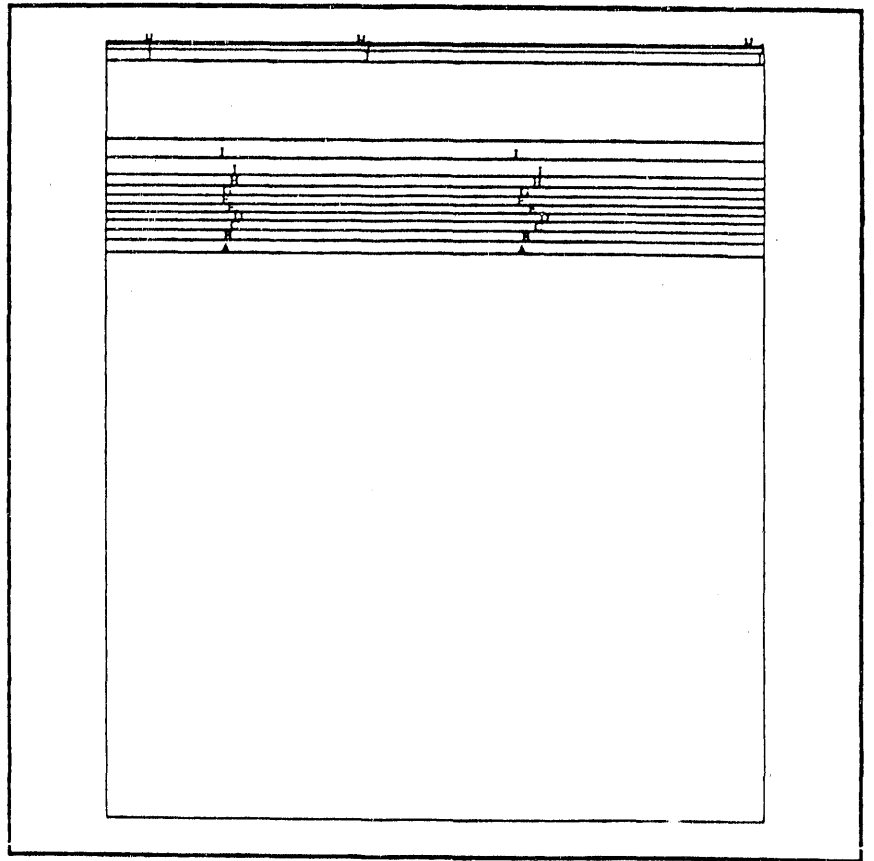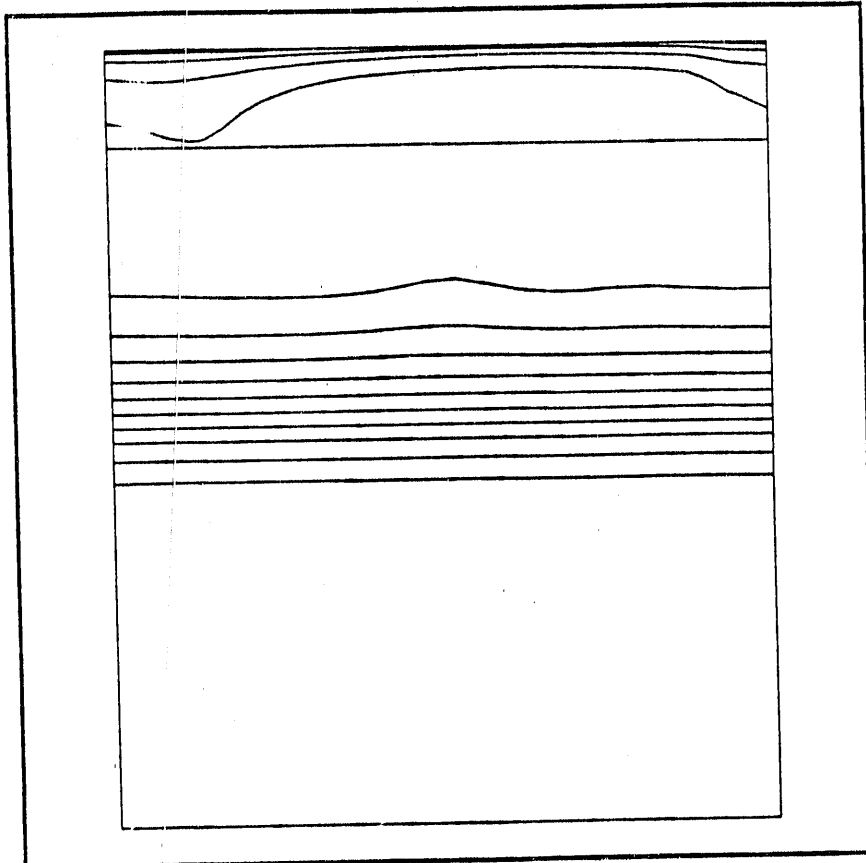
Fig. 8.3

TIME= 54000.

Fig. 8.4
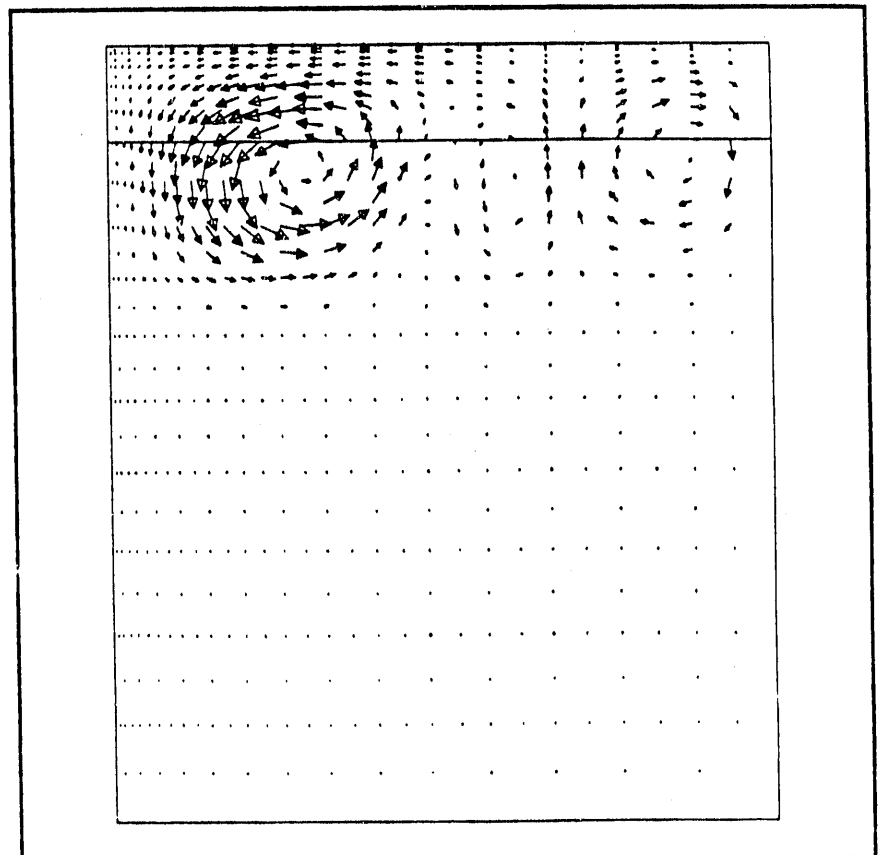
TIME= 54000.
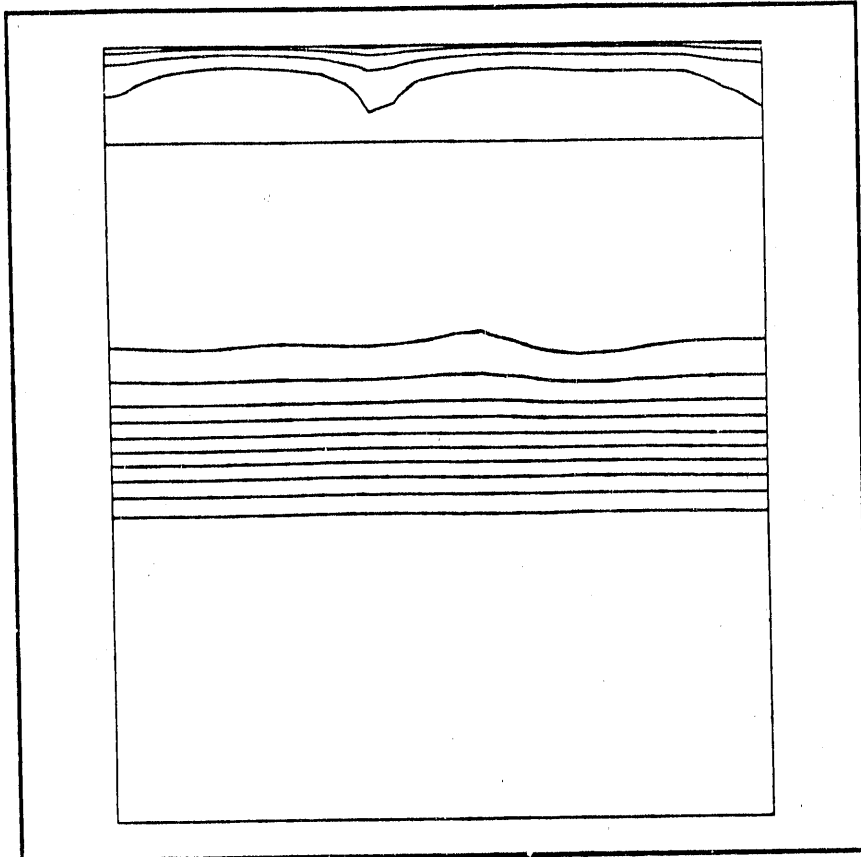
Fig. 8.5

TIME= 61500.

Fig. 8.6

TIME= 61500.

54
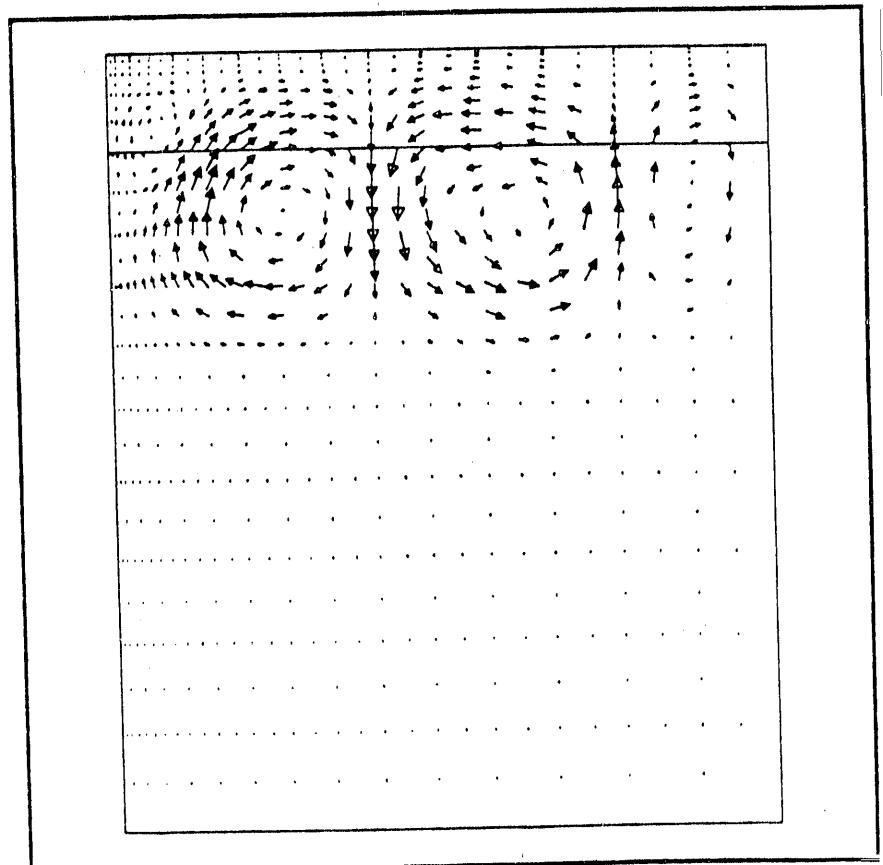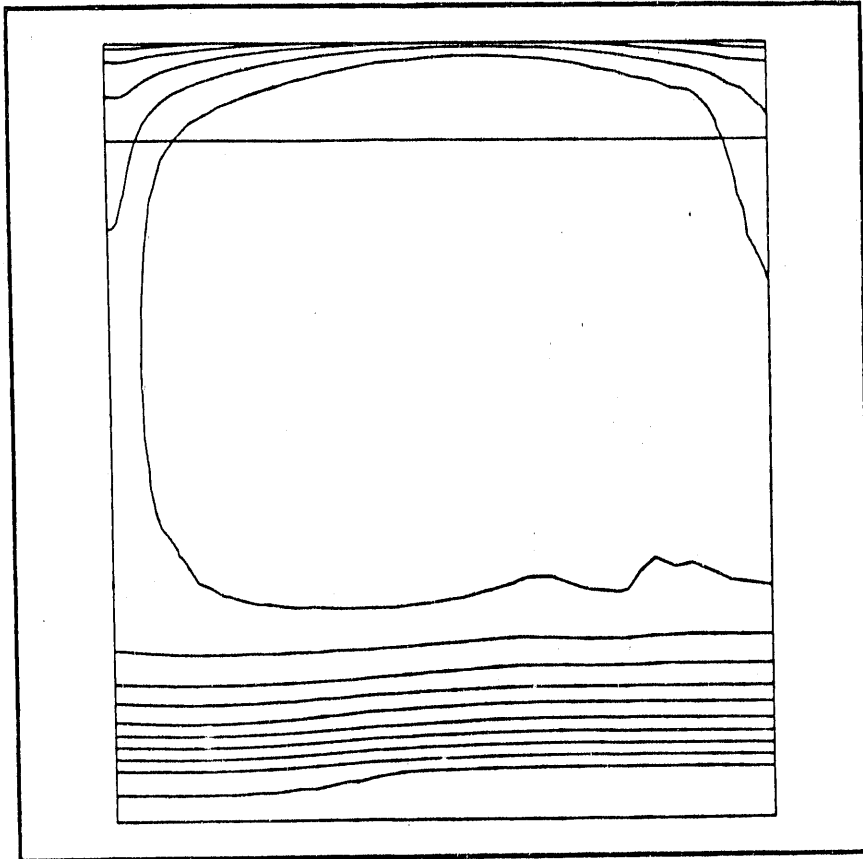
Fig. 8.7

TIME= 99000.

Fig. 8.8
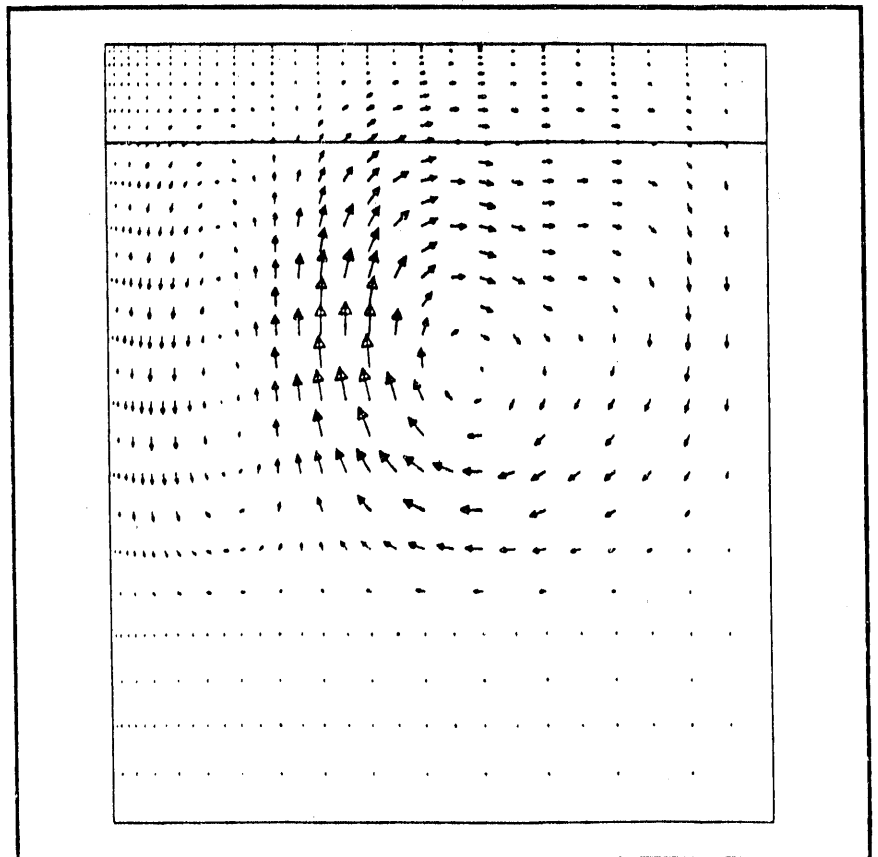
TIME= 99000.

9. CORNER INITIAL MELT

Since the boundaries in Section 7 were remote and seen to be of negligible importance, a similar initial configuration, but for the smaller 1m x 1m domain, is considered. The initial melt zone is .27m x .13m at the top left corner with radiative condition for .15m < r < .3m. We take ε = 0.09 rather than 0.9 in the radiative boundary condition. This lower value will allow the region to heat up more rapidly. The convective heat transfer conditions on the other boundaries at r = 1 and at z = 1 are as before. The time step is Δt = 3000 seconds. Effectively we have brought the far field boundary conditions of Section 7 into 1m and now will include convection.

The grid is given in Figure 9.1 and by t = 33000 seconds a strong convective cell has formed in the melt zone (Figure 9.2). The isotherms are presented in Figure 9.3 and range from 426°K to 1566°K. At t = 108000 seconds we have the pair of counter rotating cells in Figure 9.4 and the isotherms in Figure 9.5. The number of flow cells and shape of the isotherms at later times vary as indicated in the figures. Note the uniform temperature zone associated with the well-mixed flow.

After about two days of the ISV process we see the cells begin to intersect with the imposed outer radius, so boundary condition effects perturb the results. From this study we also see that convective effects are important in producing a well mixed thermal region in the melt zone. The flow velocities nonetheless are quite small, being of the order of 1 to 10 millimeters per second or equivalently a Reynolds number O(1), so Stokes flow is appropriate.

Remarks: Even with a higher heat transfer rate at the top surface, the effects will be similar. Here we have also used $\beta = 10^{-4}$. If $\beta = O(10^{-5})$ the strength of the cells is weaker but qualitatively similar behavior is seen in the final set of Figures (9.20 - 9.39).
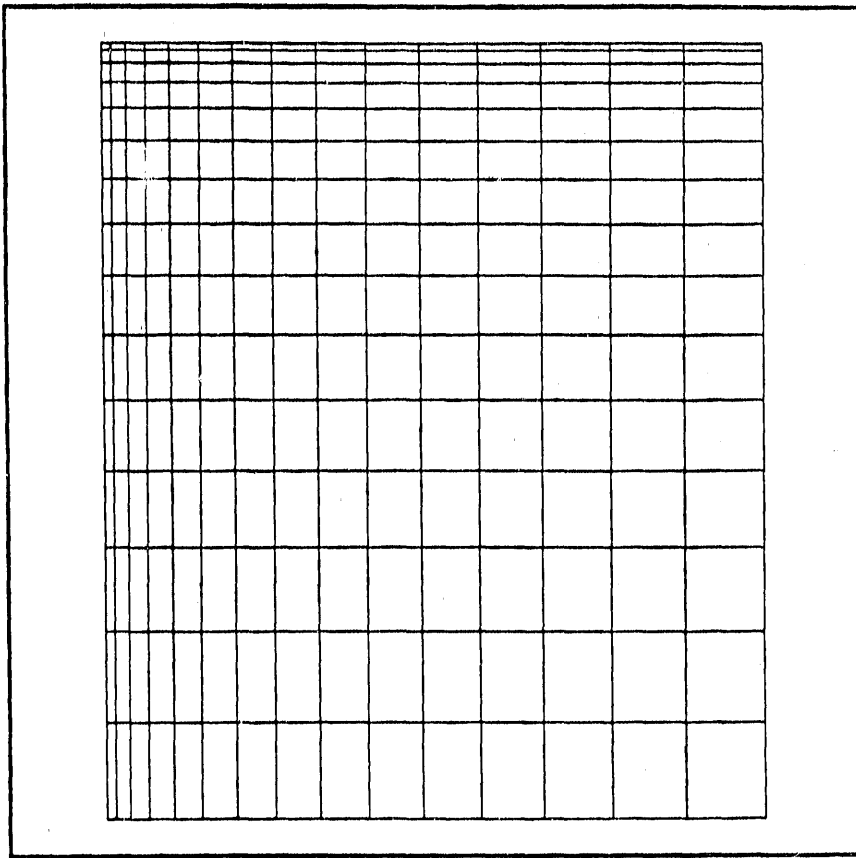
Fig. 9.1

Fig. 9.2
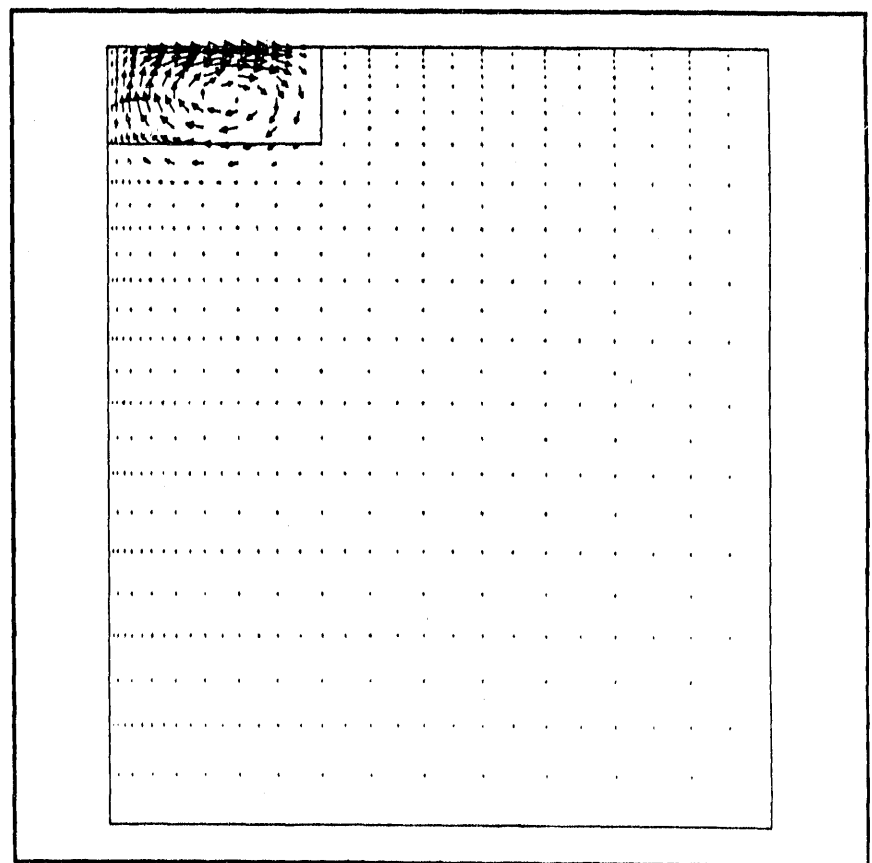
TIME= 33000.
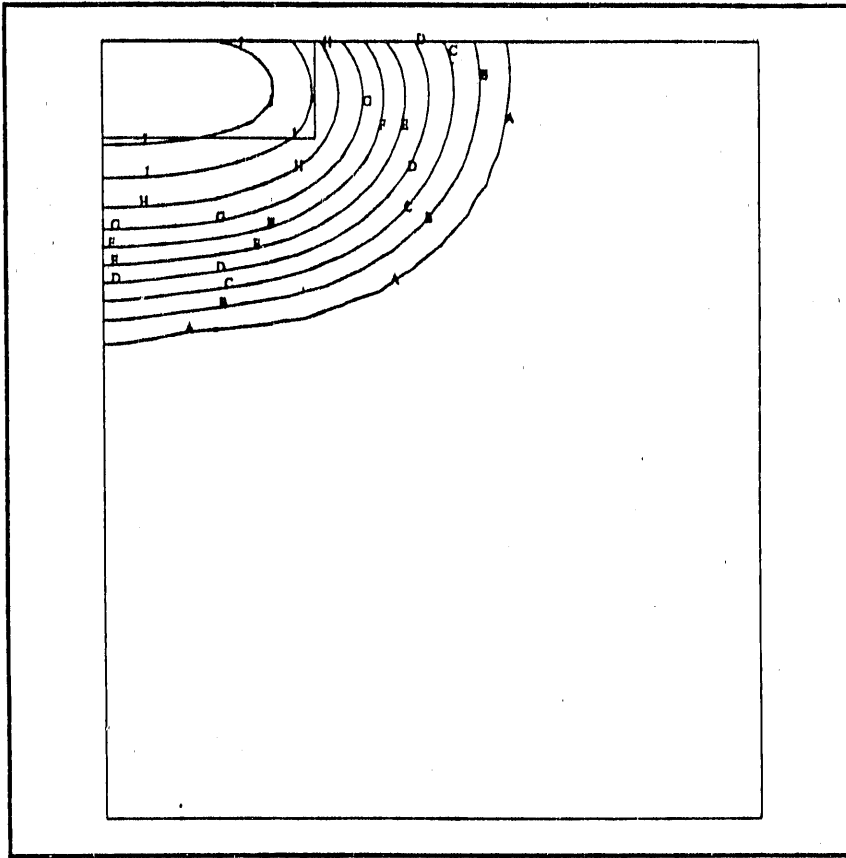
Fig. 9.3

TIME= 33000.

Fig. 9.4

TIME= 0.10800E+06

58
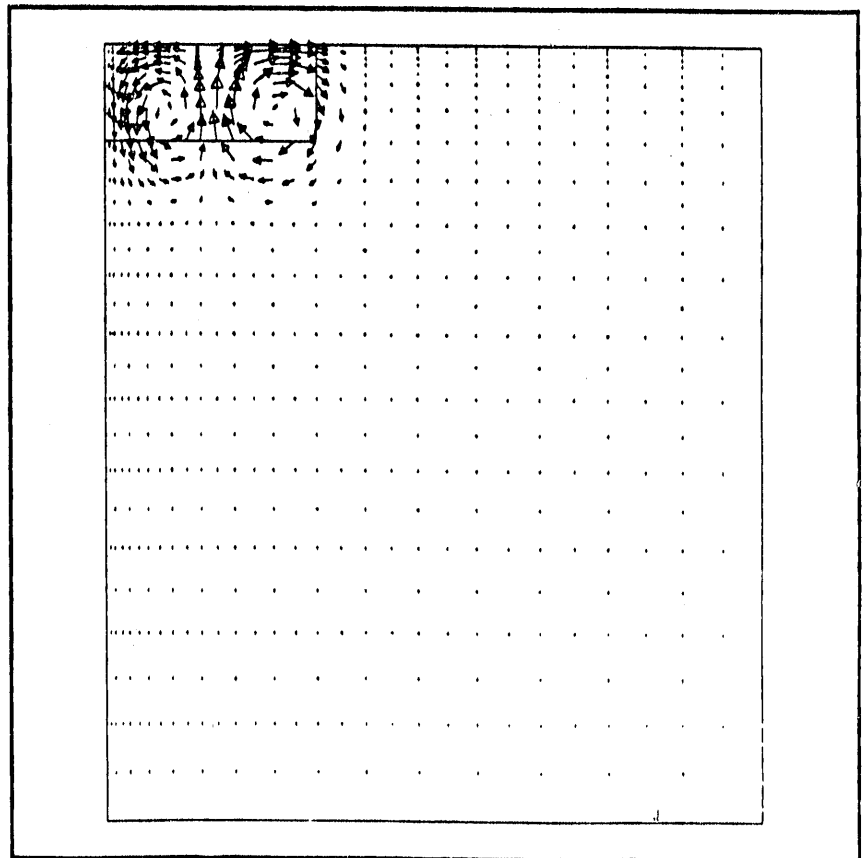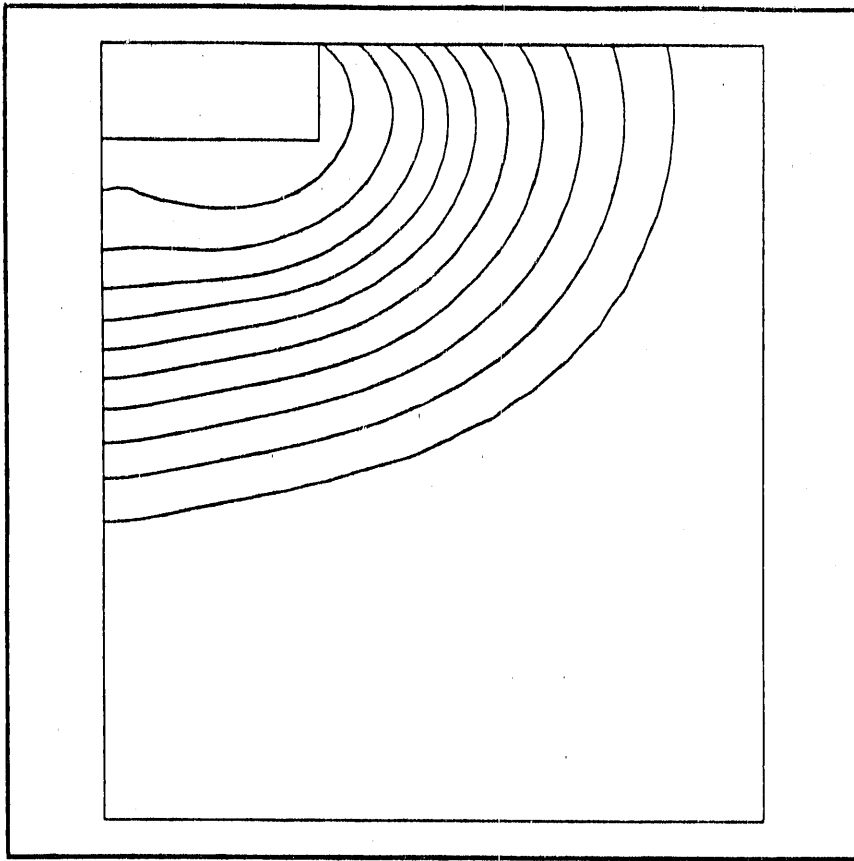
Fig. 9.5

TIME= 0.10800E+06
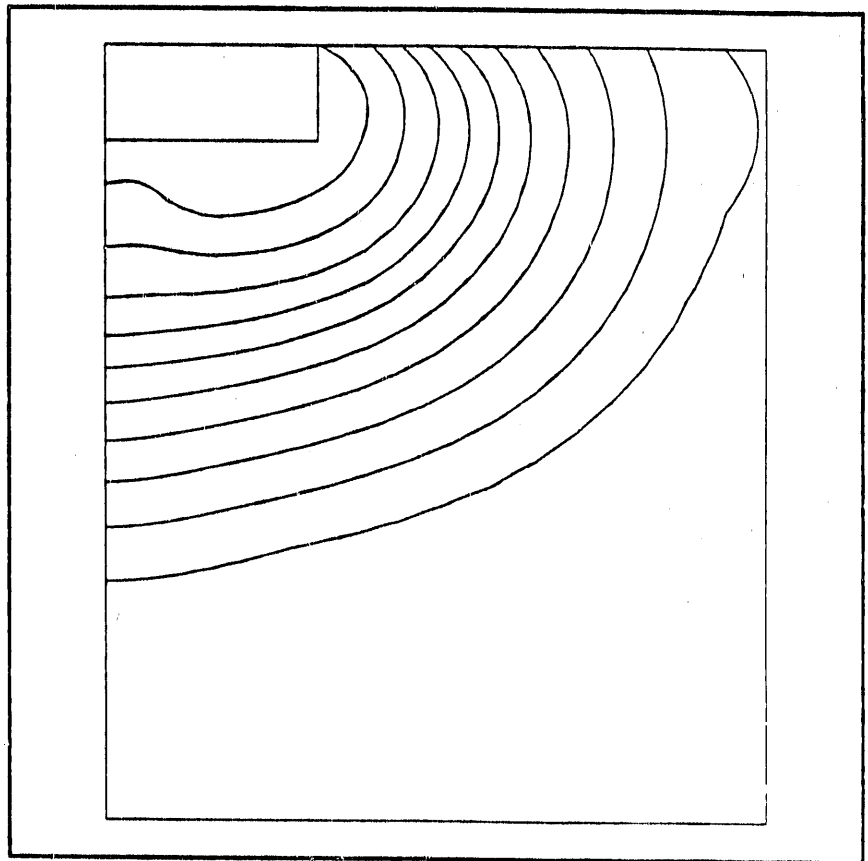
Fig. 9.6

TIME= 0.15300E+06
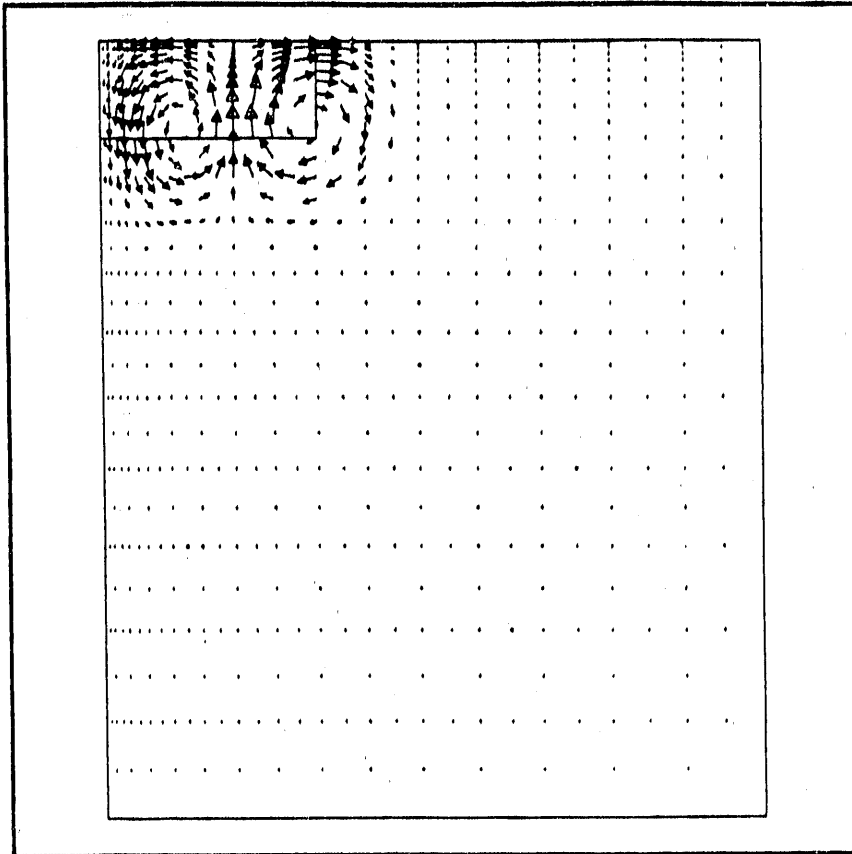
Fig. 9.7

TIME= 0.15300E+06

Fig. 9.8

TIME= 0.16800E+06

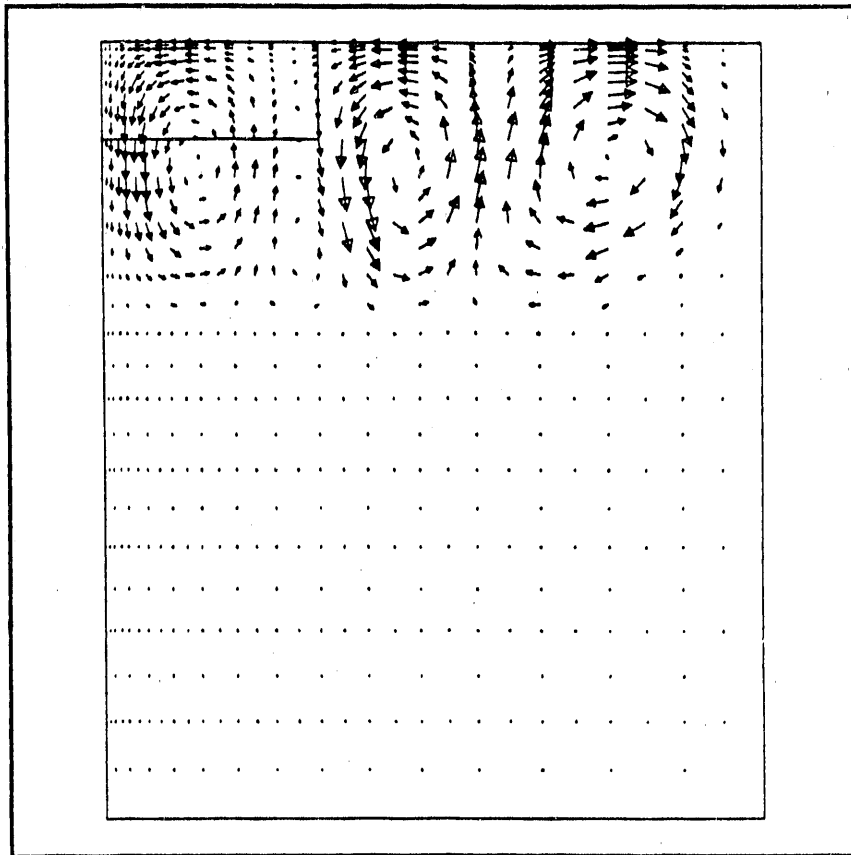60
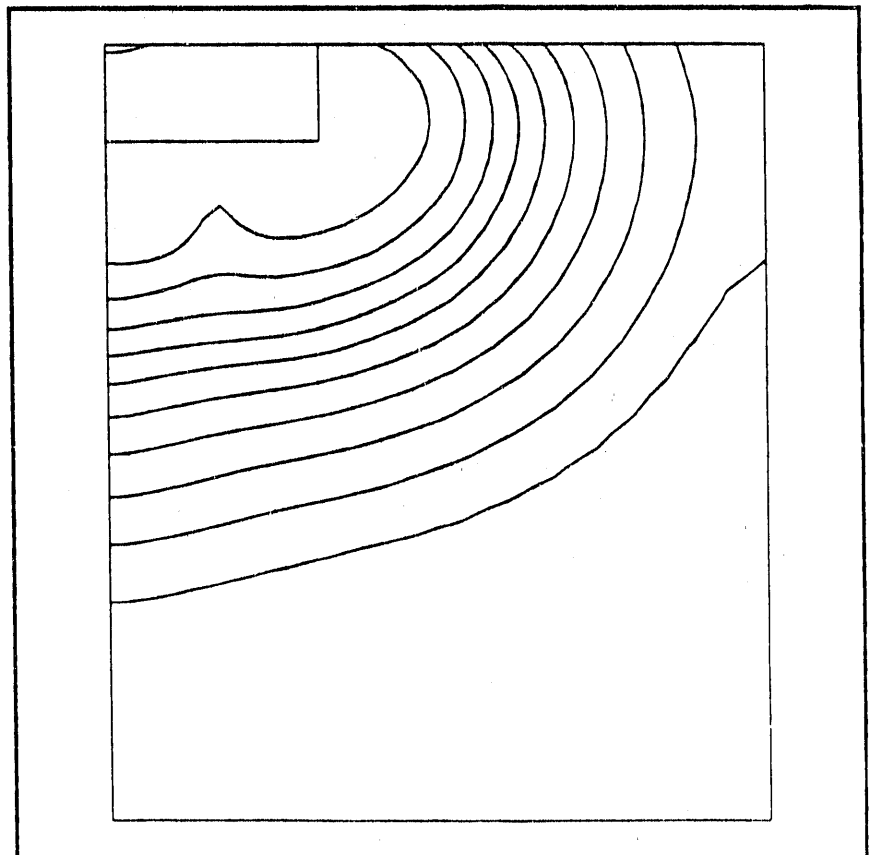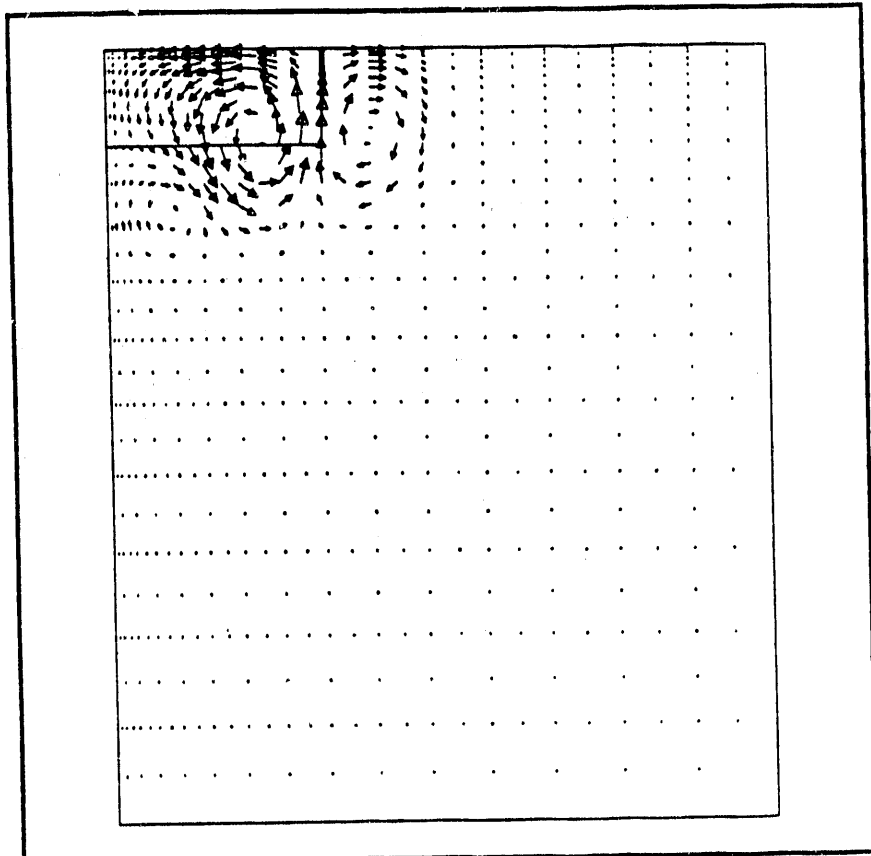
Fig. 9.9

TIME= 0.16800E+06

Fig. 9.10
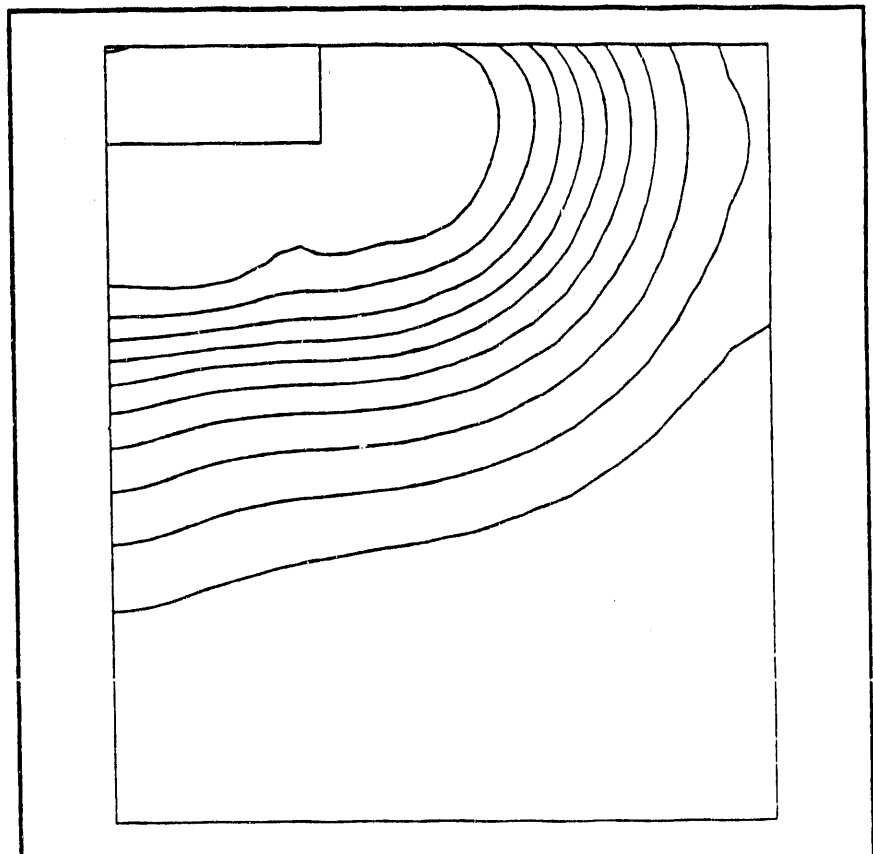
TIME= 0.18300E+06
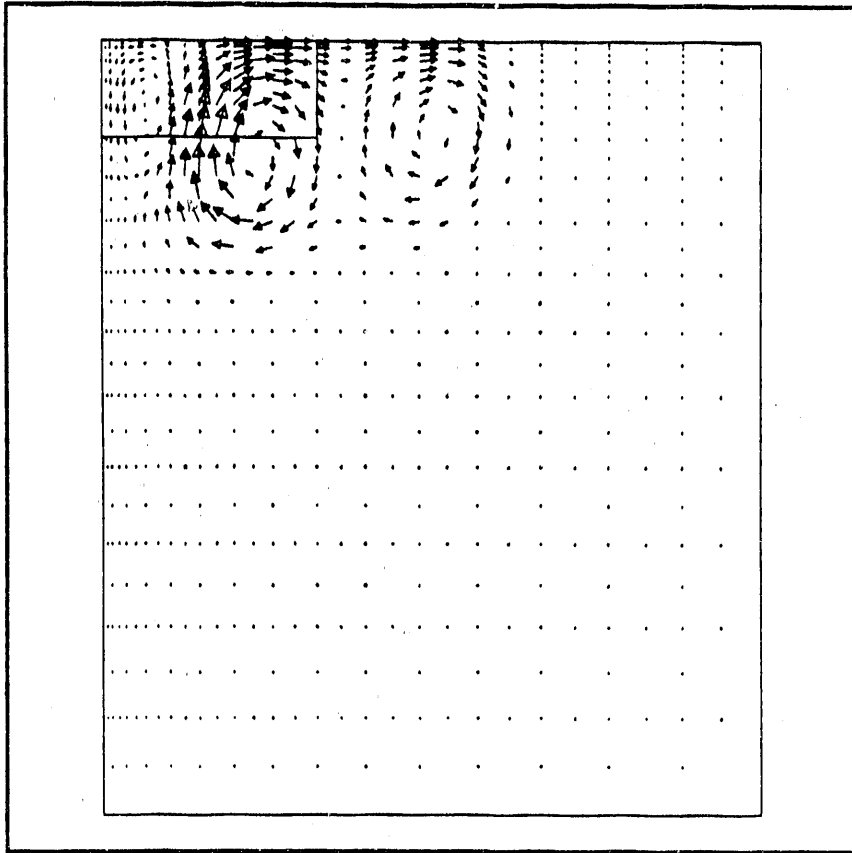
Fig. 9.11

TIME= 0.18300E+06

Fig. 9.12
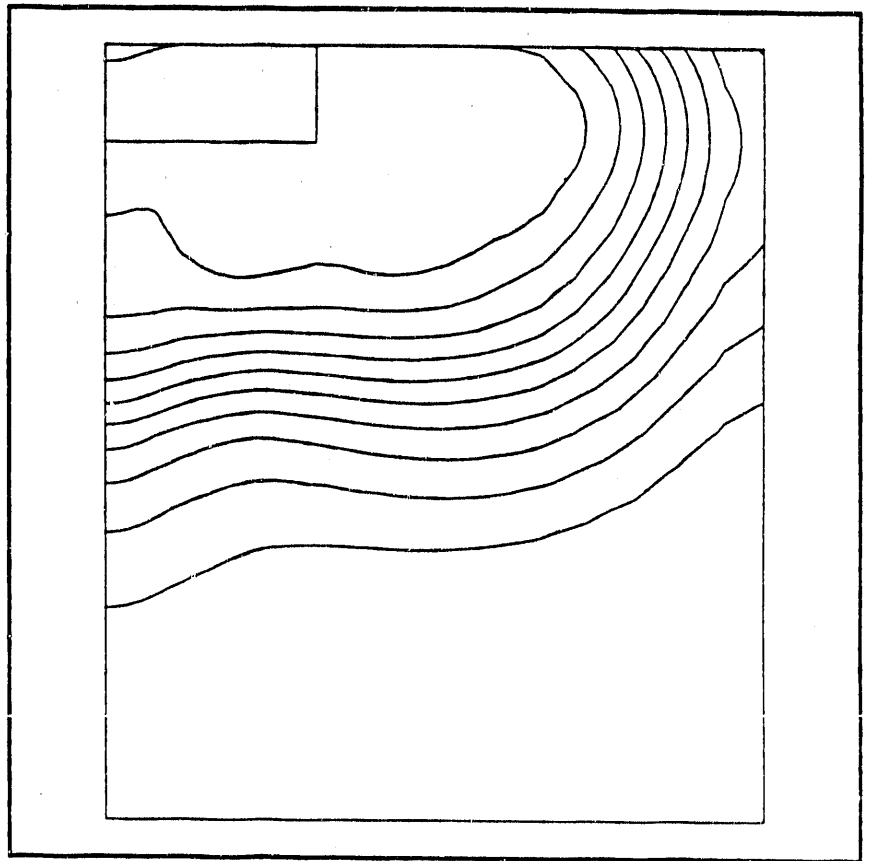
TIME= 0.19800E+06
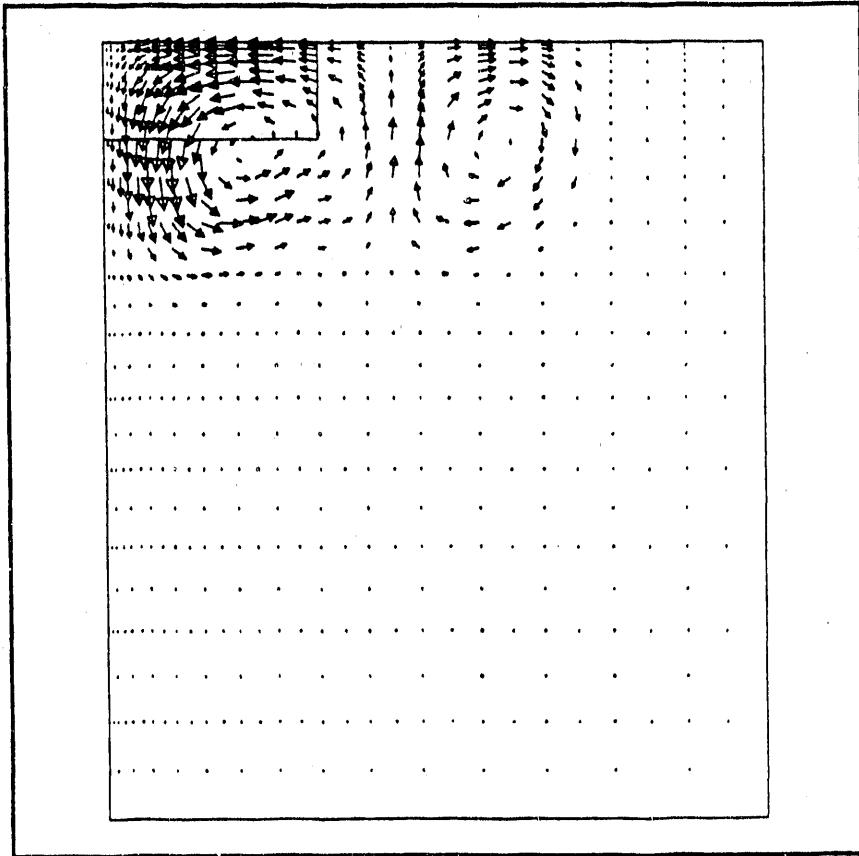
Fig. 9.13

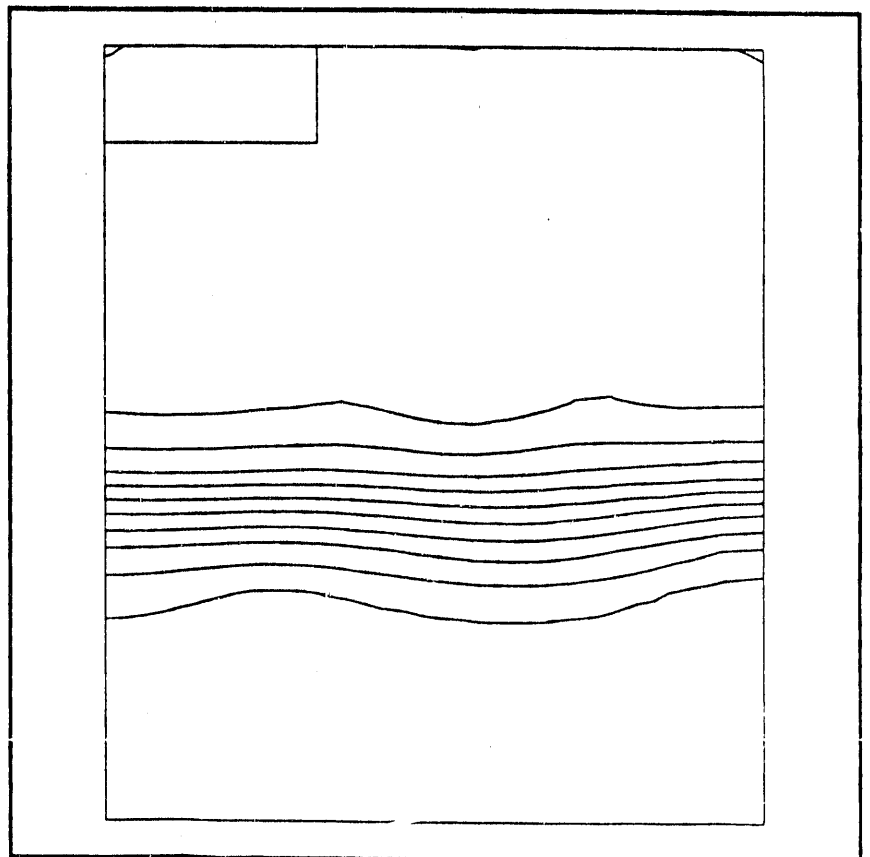TIME= 0.19800E+06
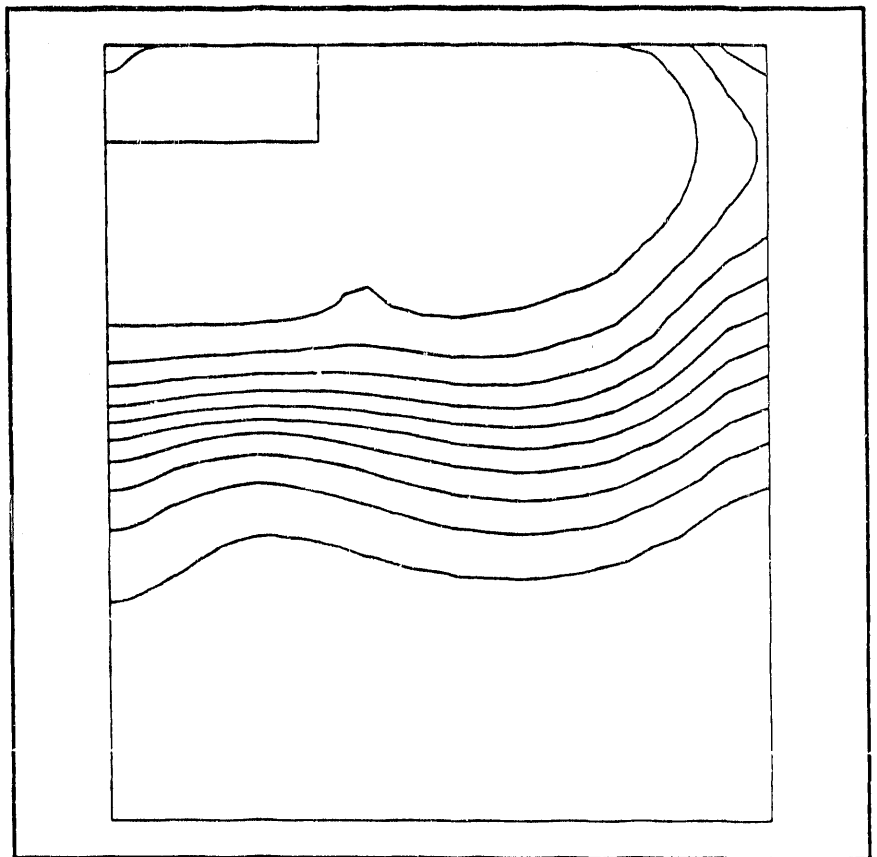
Fig. 9.14

TIME= 0.21300E+06

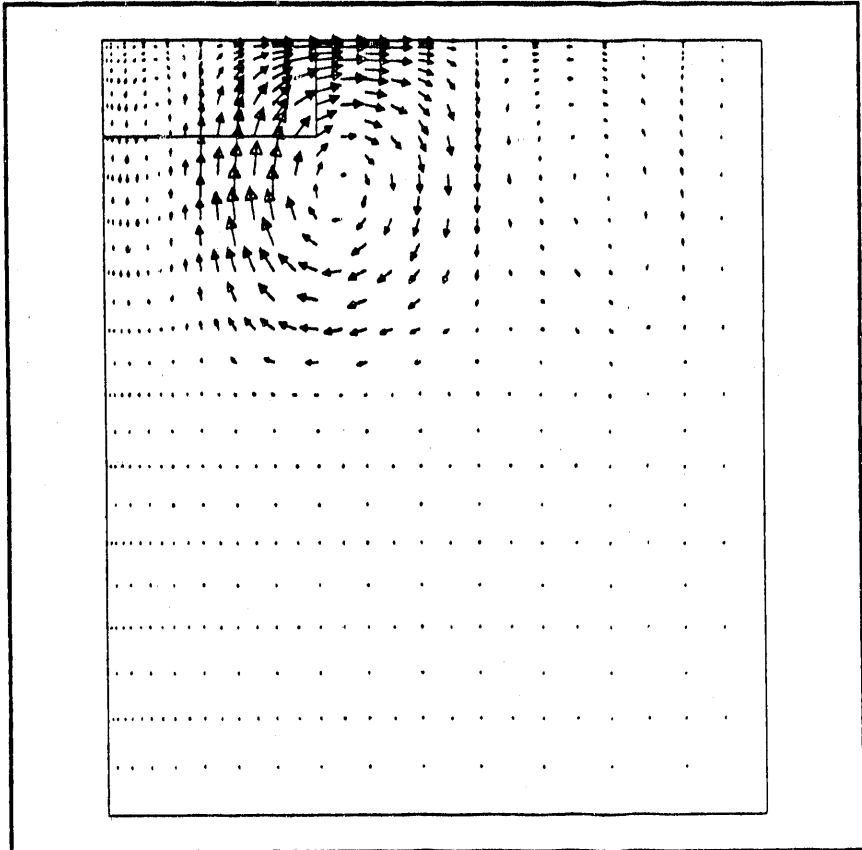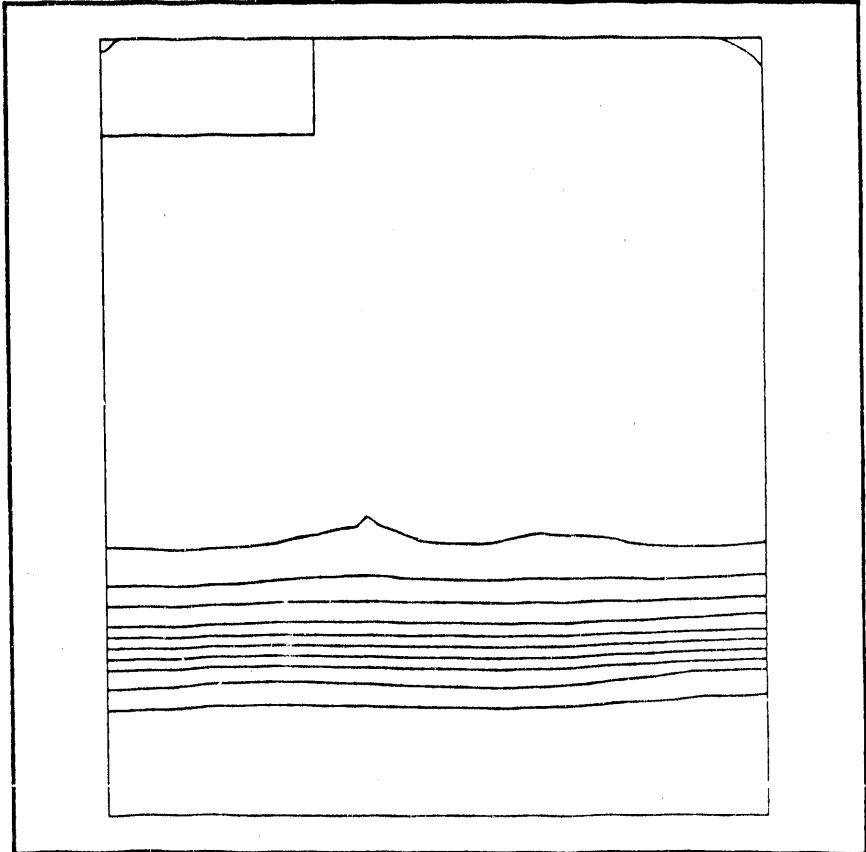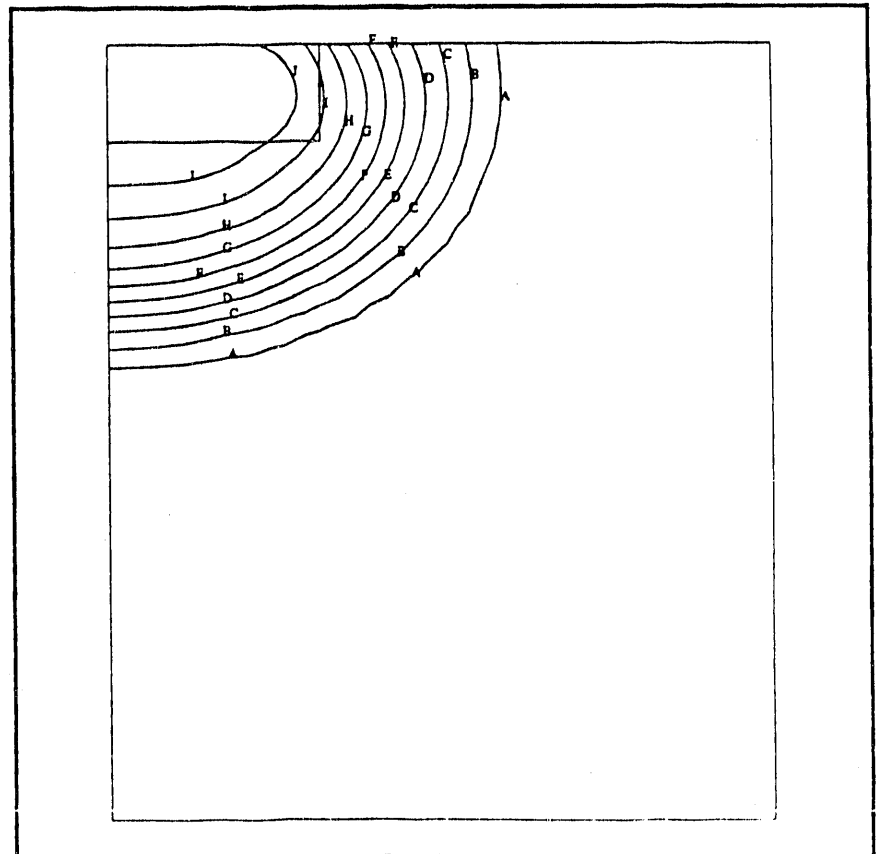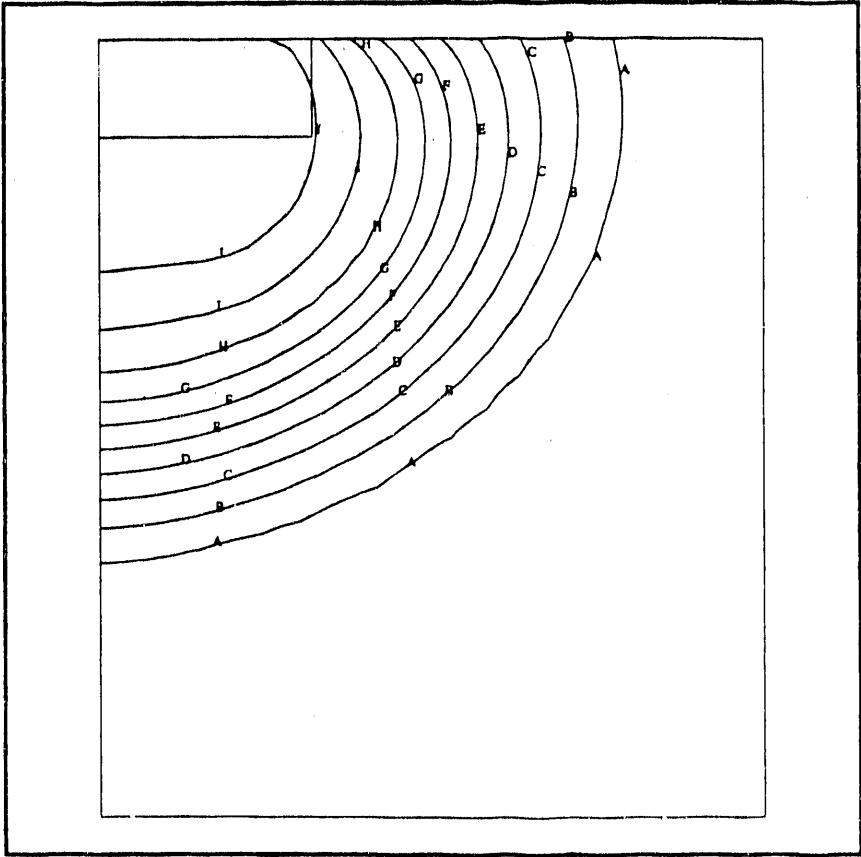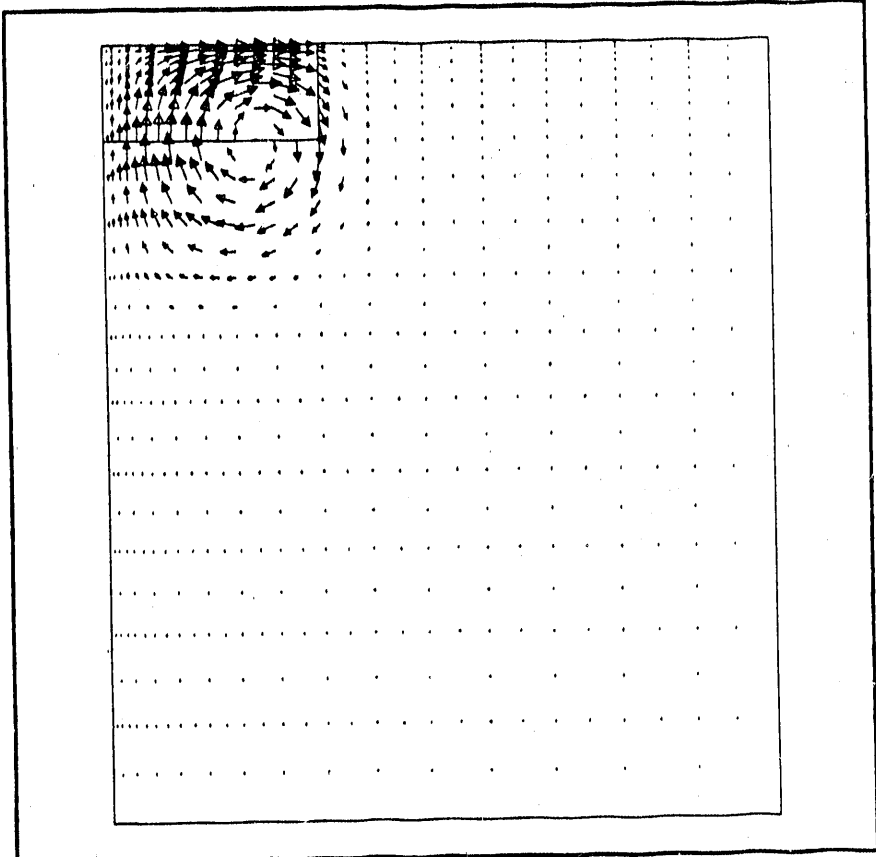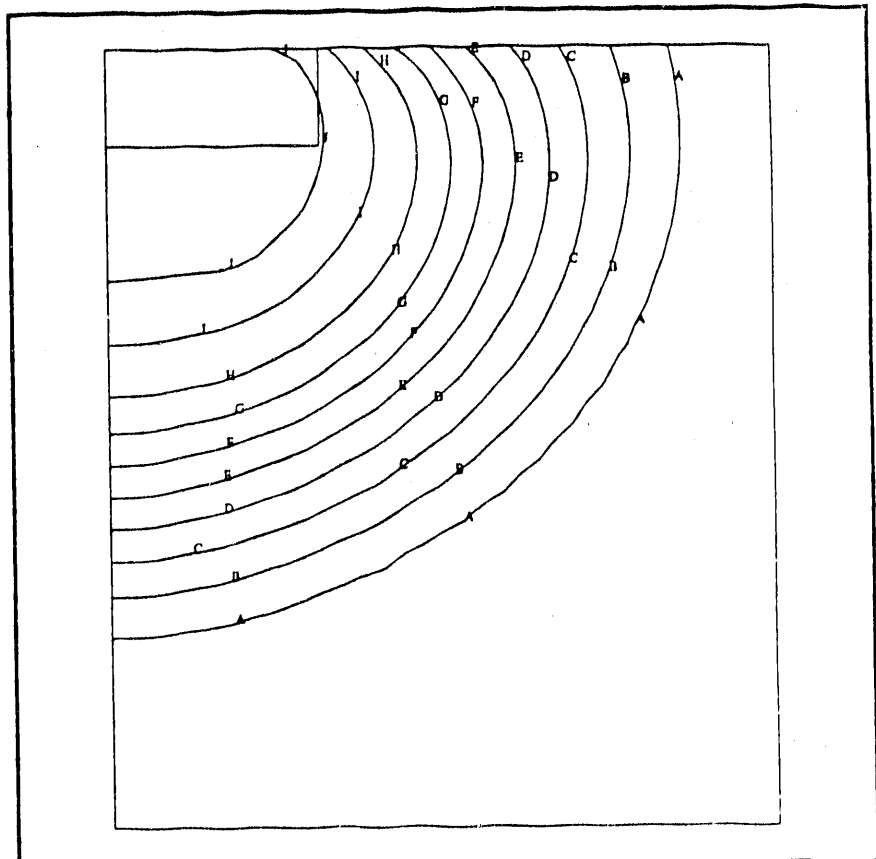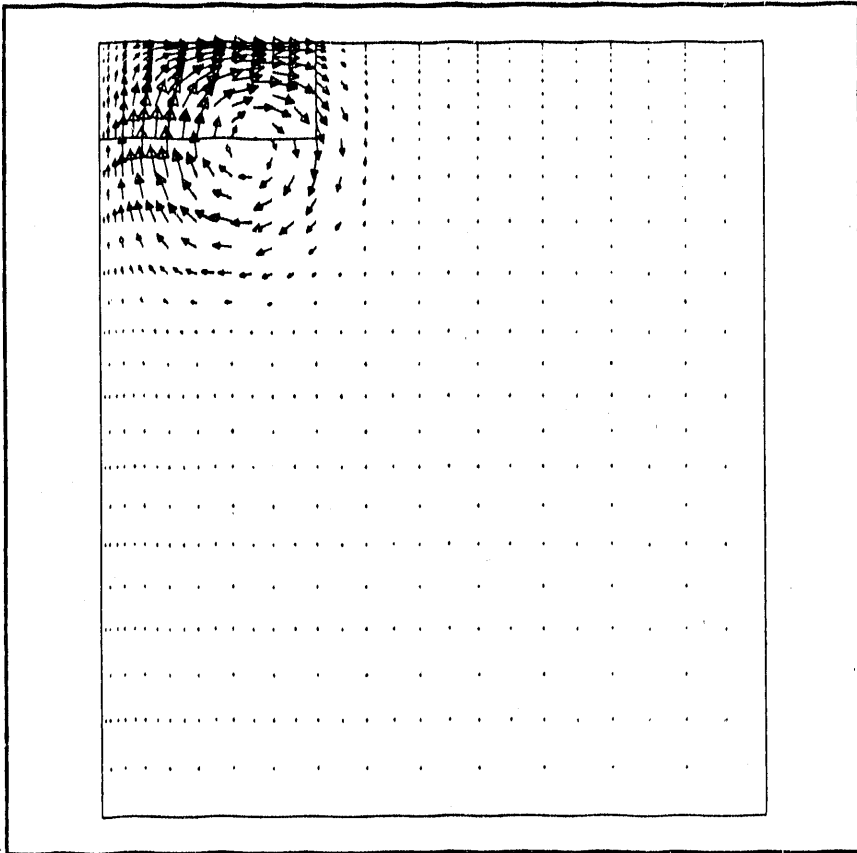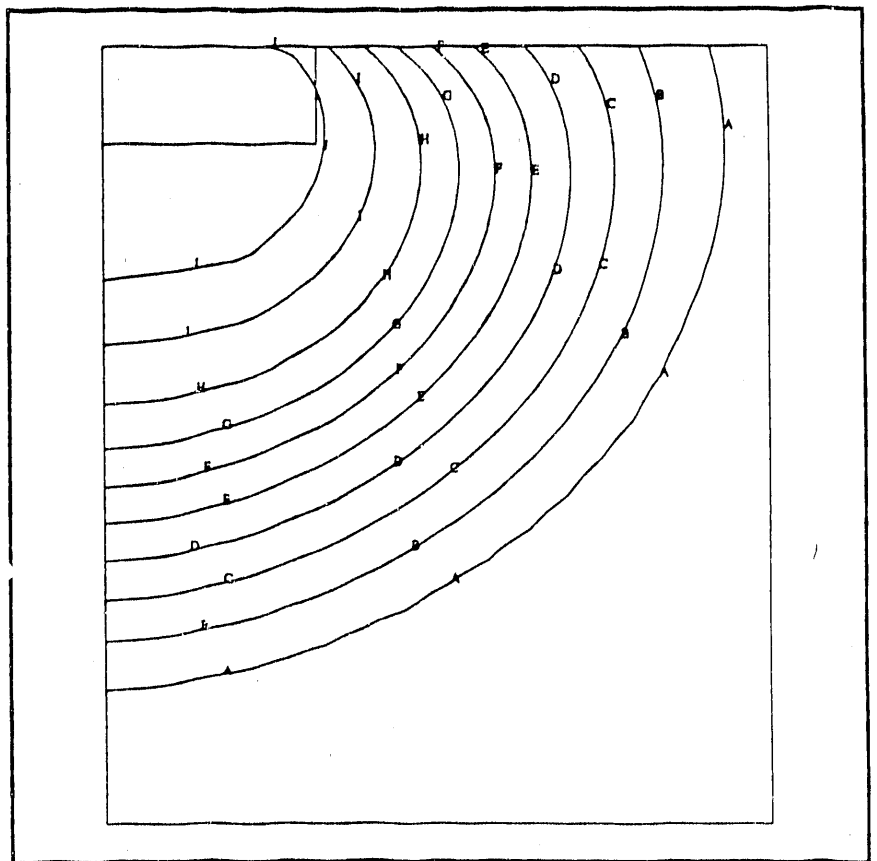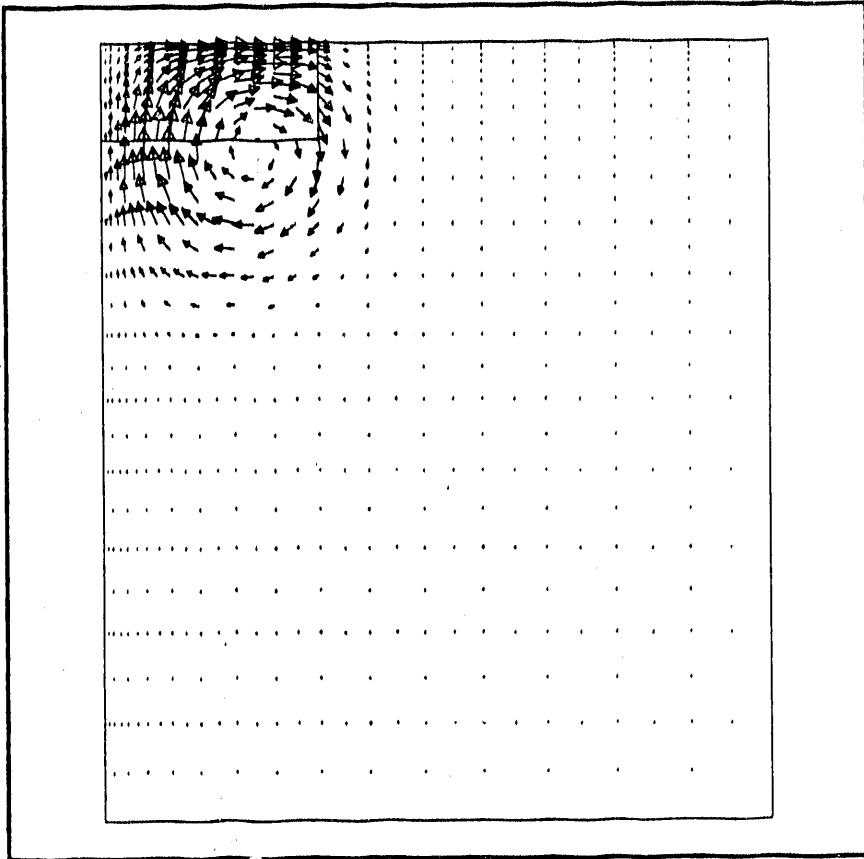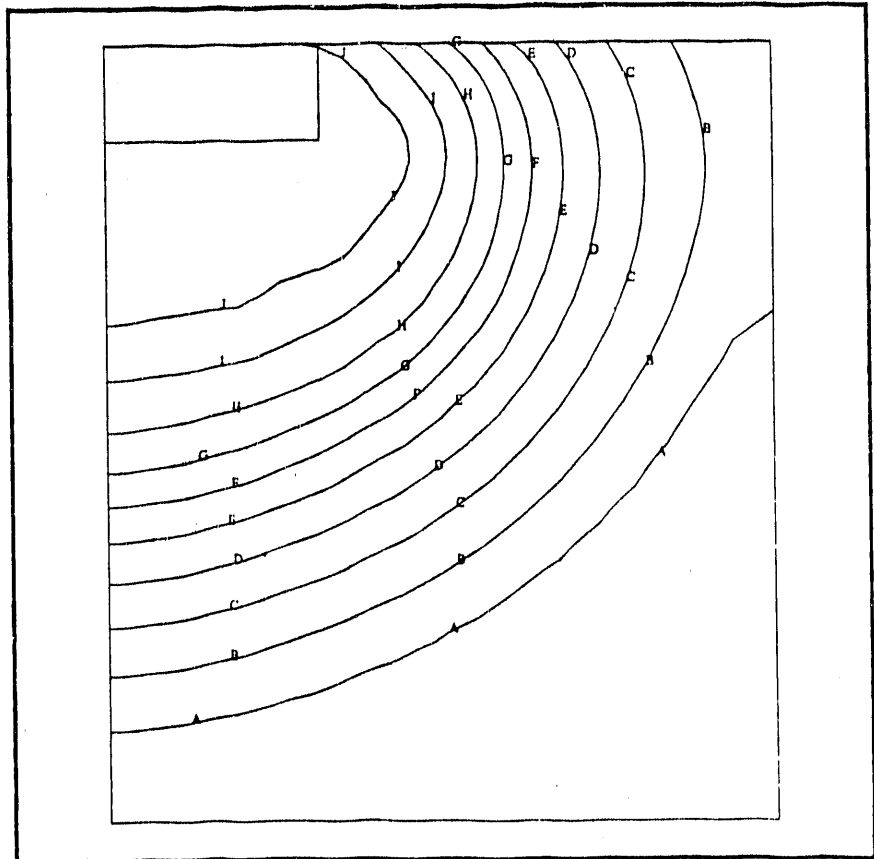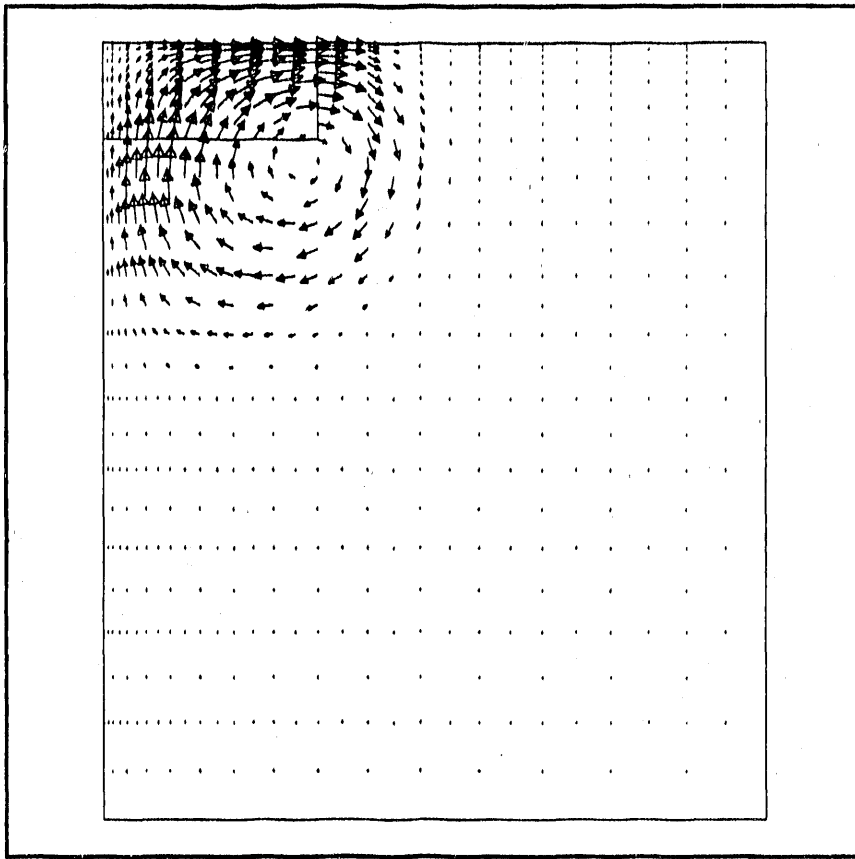Fig. 9.15

TIME= 0.21300E+06

Fig. 9.16

TIME= 0.22800E+06

Fig. 9.17

TIME= 0.22800E+06

Fig. 9.18

TIME= 0.24300E+06
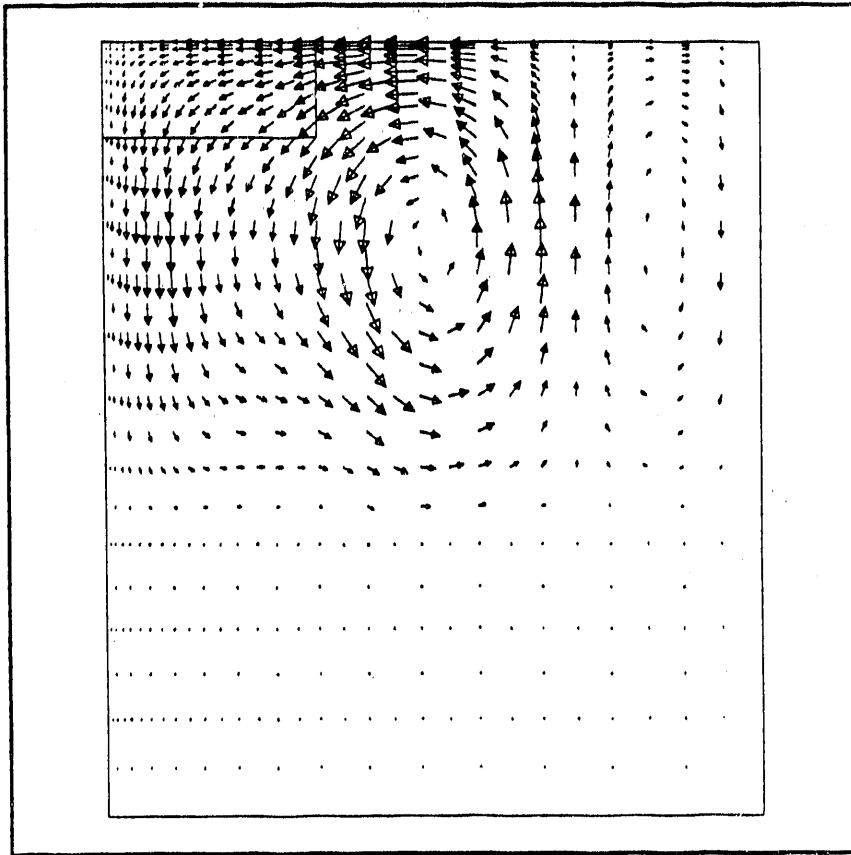
Fig. 9.19

TIME= 0.24300E+06

Fig. 9.20

TIME= 33000.

66
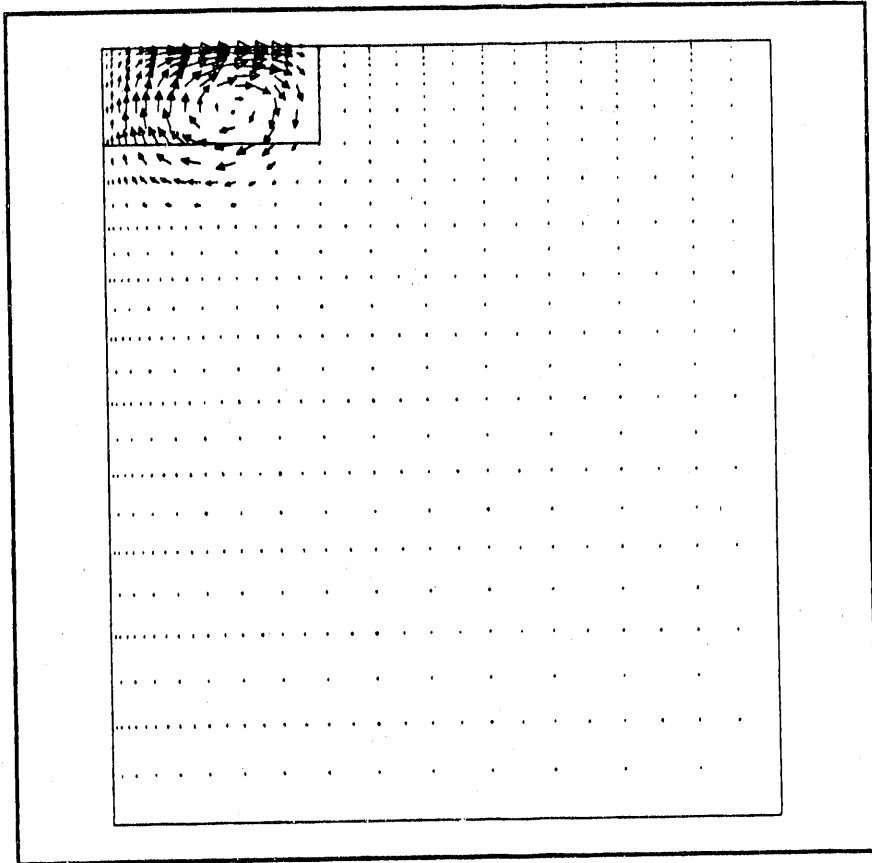
Fig. 9.21

TIME= 33000.
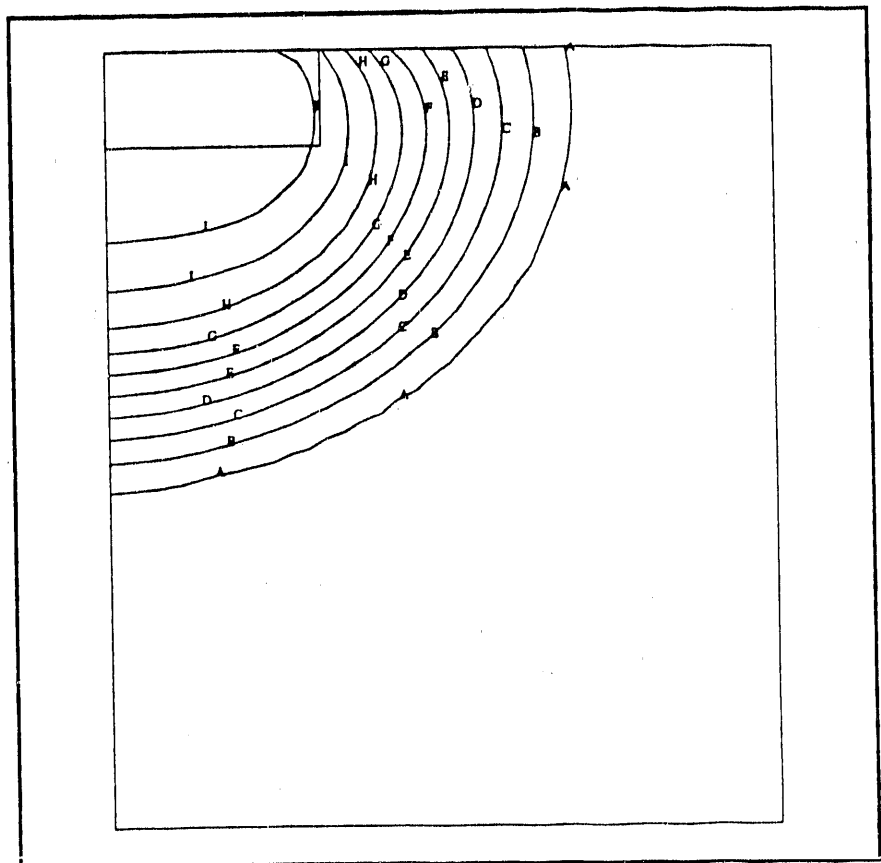
Fig. 9.22

TIME= 63000.
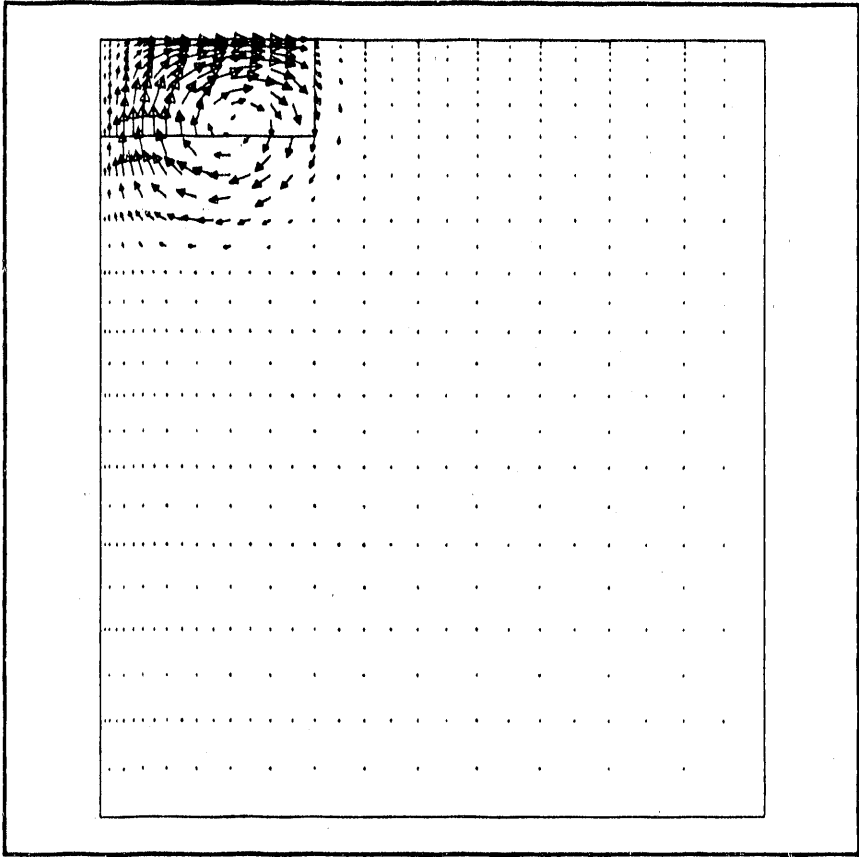
Fi. 9.23

TIME= 63000.

Fig. 9.24

TIME= 93000.

68

Fig. 9.25

TIME= 93000.

Fig. 9.26

TIME= 0.12300E+06

TIME= 0.12300E+06

Fig. 9.27

Fig. 9.28

TIME= 0.15300E+06

70

Fig. 9.29

TIME= 0.15300E+06

Fig. 9.30

TIME= 0.18300E+06

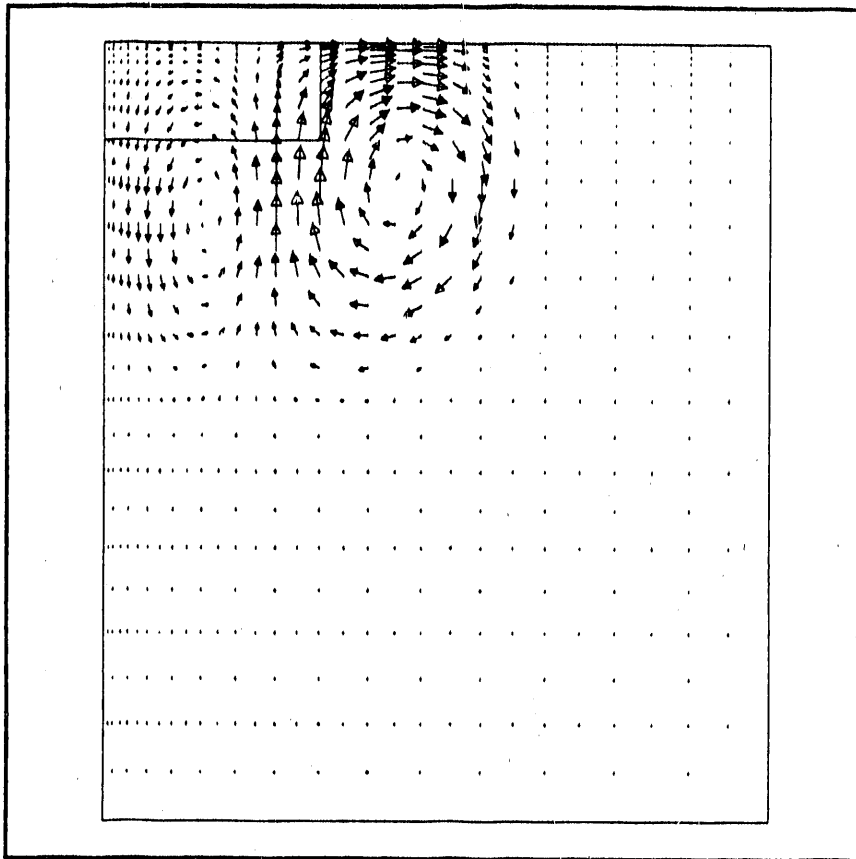Fig. 9.31

TIME= 0.18300E+06
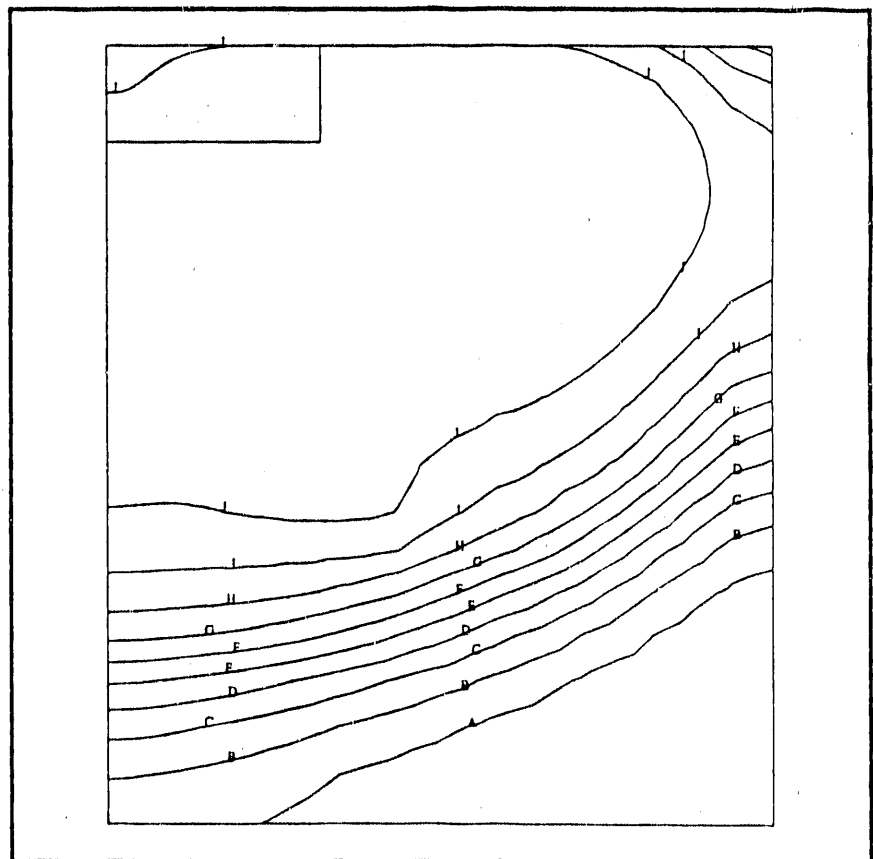
Fig. 9.32

TIME= 0.21300E+06

72
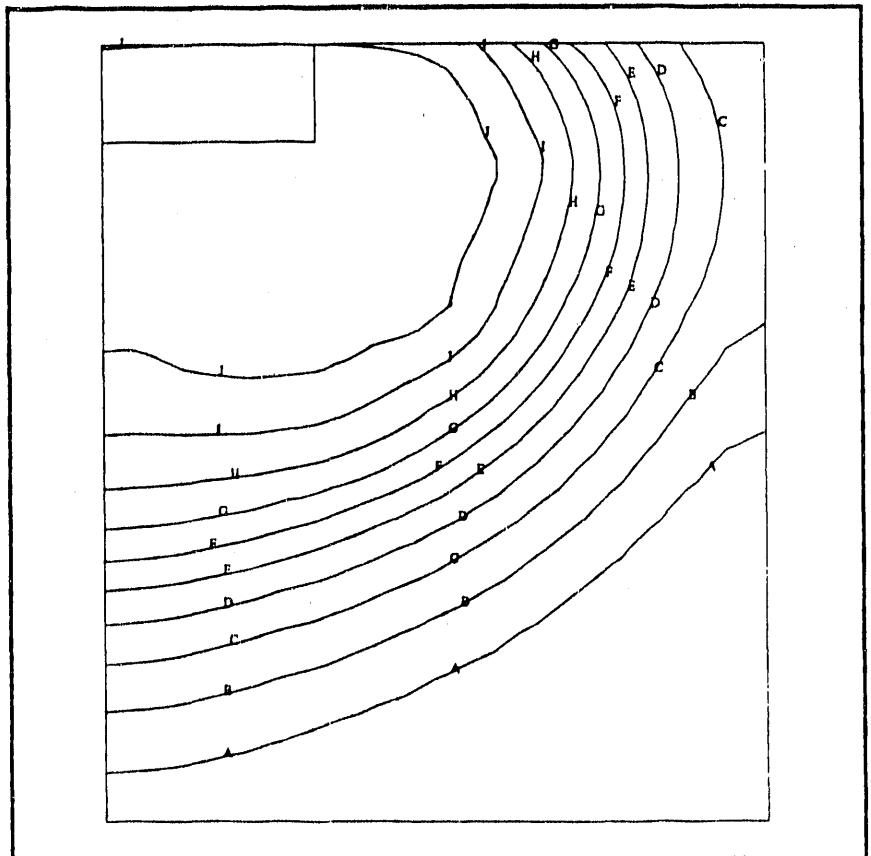
Fig. 9.33
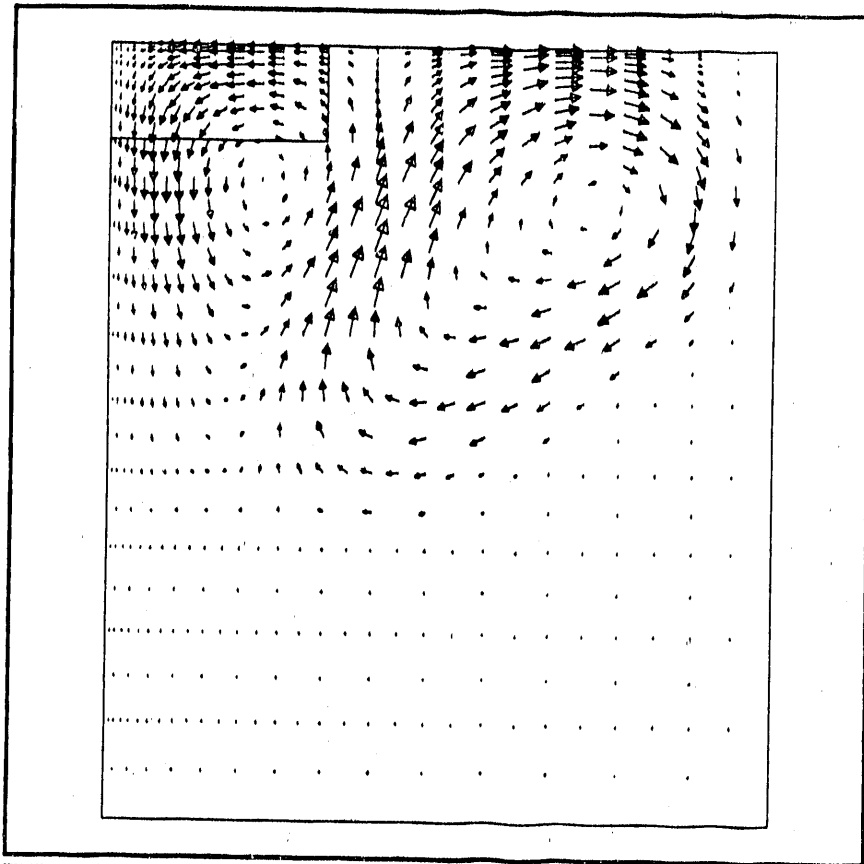
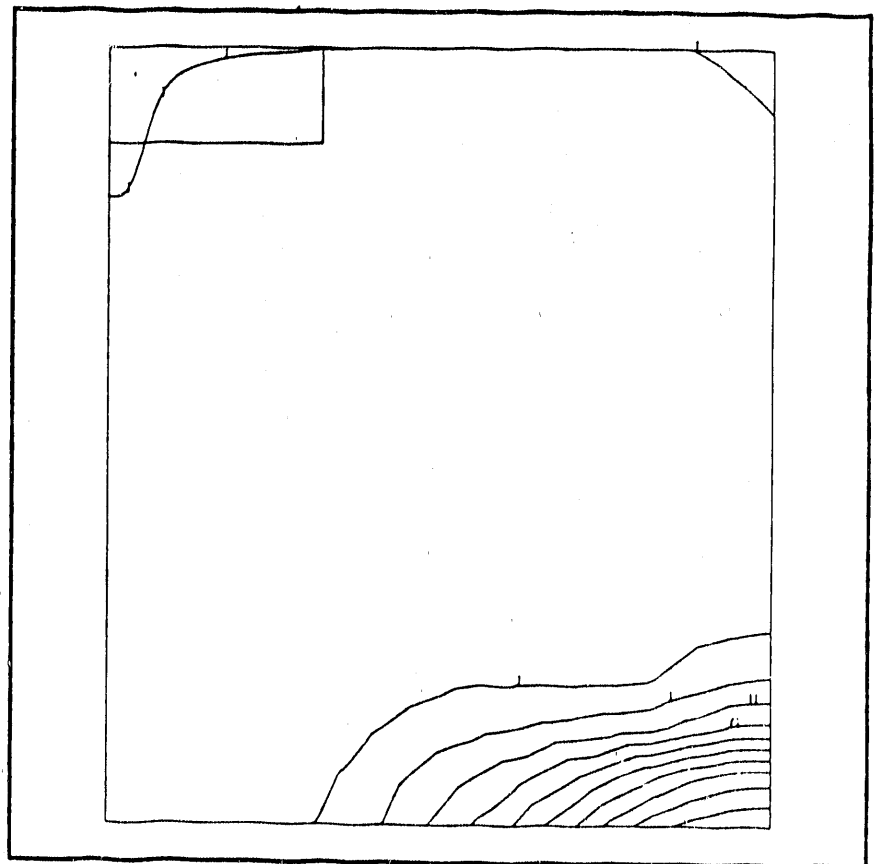TIME= 0.21300E+06

Fig. 9.34

TIME= 0.24300E+06

73

Fig. 9.35

TIME= 0.24300E+06
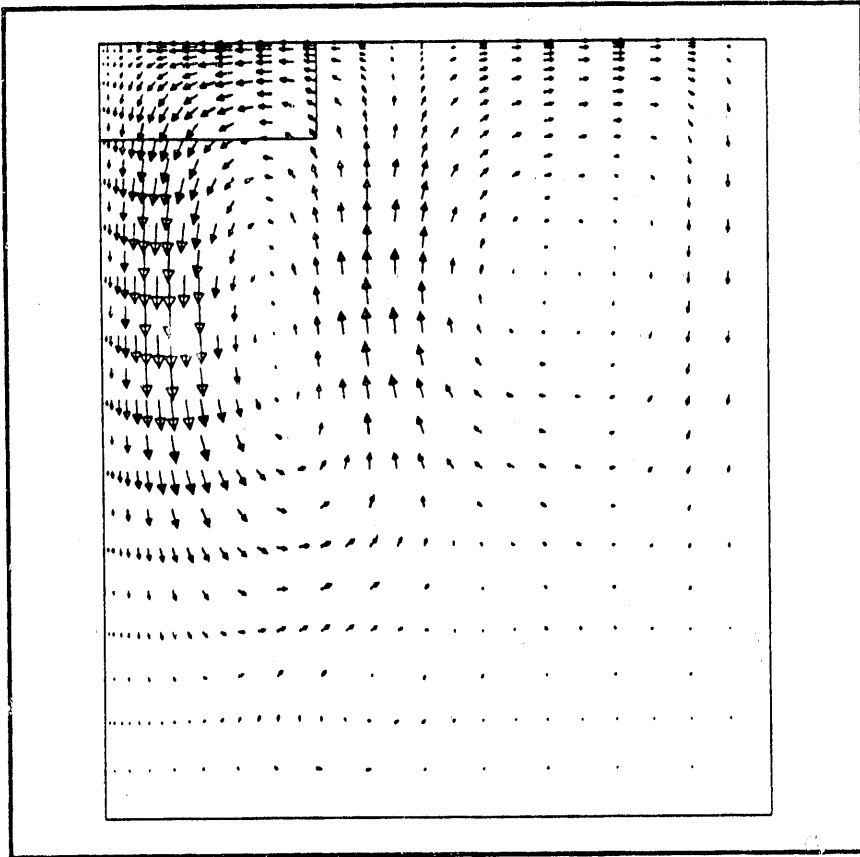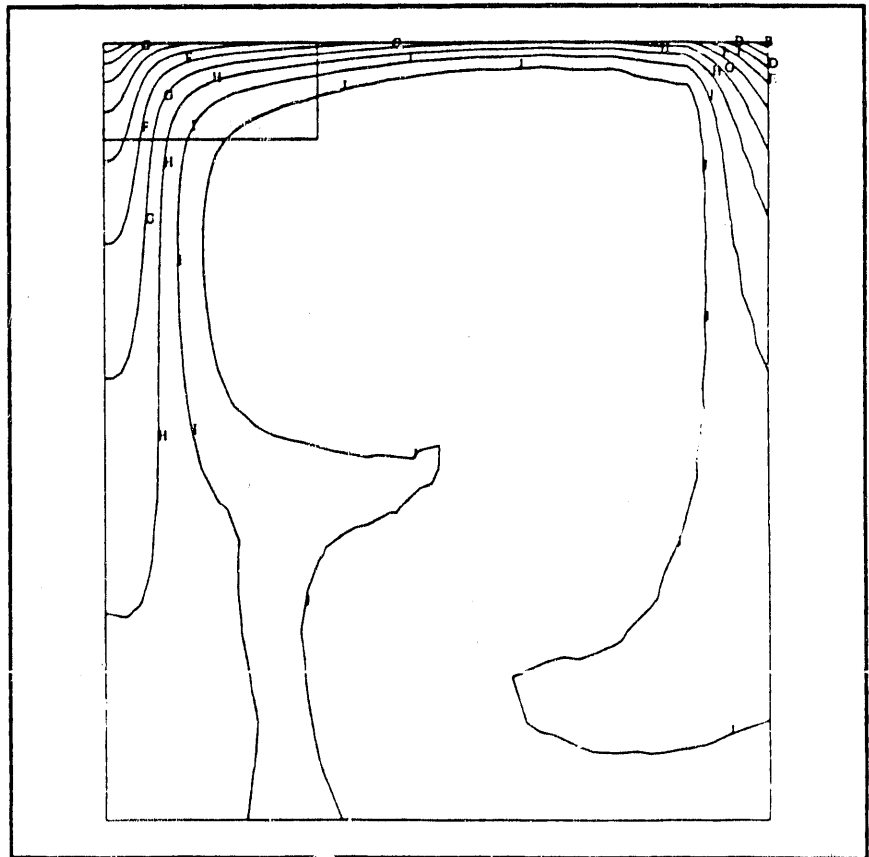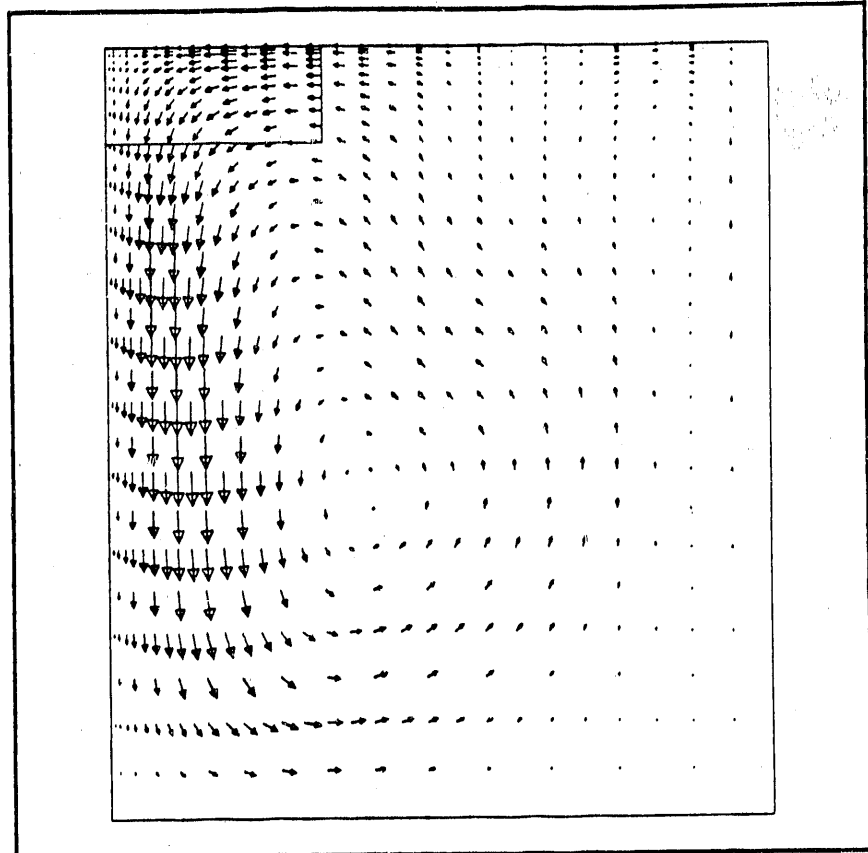
Fig. 9.36

TIME= 0.27300E+06

74

Fig. 9.37

TIME= 0.27300E+06

Fig. 9.38

TIME= 0.30300E+06

TIME= 0.30300E+06

Fig. 9.39

REFERENCES

1. R. J. MacKinnon, D. C. Mecham, et al., <u>Modeling Requirements for In Situ Vitrification</u>, Revision 1.0, EG&G Idaho, Inc., EGG-WM-9035, 1990.

2. R. J. MacKinnon, P. E. Murray, et al., <u>In Situ Model Development and Implementation Plan</u>, Revision 1.0, EG&G Idaho, Inc., EGG-WM-9036, 1990.

3. R. McLay and G. F. Carey, <u>Coupled Heat Transfer and Viscous Flow and Magnetic Effects in Weld Pool Analysis</u>, Int. Jnl. Numer. Meth. Eng., Vol. 9, 713-730, 1989.

4. P. E. Murray, G. L. Hawkes, and R. J. MacKinnon, <u>A Preliminary Numerical Study of Heat Transport During In Situ Vitrification of Soil</u>, EG&G Idaho, Inc., EGG-WM-9038, 1990.

END

DATE FILMED

01/02/91